JOURNAL OF GEOPHYSICAL RESEARCH: SOLID EARTH, VOL. 118, 3142–3159, doi:10.1002/jgrb.50207, 2013

Coseismic and postseismic slip associated with the 2010 Maule Earthquake, Chile: Characterizing the Arauco Peninsula barrier effect

Yu-nung Nina Lin,[1] Anthony Sladen,[2] Francisco Ortega-Culaciati,[1] Mark Simons,[1]
Jean-Philippe Avouac,[1] Eric J. Fielding,[3] Benjamin A. Brooks,[4] Michael Bevis,[5]
Jeff Genrich,[1] Andreas Rietbrock,[6] Christophe Vigny,[7] Robert Smalley,[8] and Anne Socquet[9]

Received 17 October 2012; revised 4 March 2013; accepted 1 May 2013; published 17 June 2013.

[1] Observations of coseismic and postseismic deformation associated with the 2010 $Mw = 8.8$ Maule earthquake in south-central Chile provide constraints on the spatial heterogeneities of frictional properties on a major subduction megathrust and how they have influenced the seismic rupture and postseismic effects. We find that the bulk of coseismic slip occurs within a single elongated patch approximately 460 km long and 100 km wide between the depths of 15 and 40 km. We infer three major patches of afterslip: one extends northward along strike and downdip of the major coseismic patch between 40 and 60 km depth; the other two bound the northern and southern ends of the coseismic patch. The southern patch offshore of the Arauco Peninsula is the only place showing resolvable afterslip shallower than 20 km depth. Estimated slip potency associated with postseismic slip in the 1.3 years following the earthquake amounts to 20–30% of that generated coseismically. Our estimates of the megathrust frictional properties show that the Arauco Peninsula area has positive but relatively low $(a-b)\sigma_{\mathrm{n}}$ values ($0.01 \sim 0.22$ MPa), that would have allowed dynamic rupture propagation into this rate-strengthening area and afterslip. Given the only modestly rate-strengthening megathrust friction in this region, the barrier effect may be attributed to its relatively large size of the rate-strengthening patch. Coseismic and postseismic uplift of the Arauco Peninsula exceeds interseismic subsidence since the time of the last major earthquake in 1835, suggesting that coseismic and postseismic deformation has resulted in some permanent strain in the forearc.

Citation: Lin, Y.-n. N., et al. (2013), Coseismic and postseismic slip associated with the 2010 Maule Earthquake, Chile: Characterizing the Arauco Peninsula barrier effect, *J. Geophys. Res. Solid Earth*, *118*, 3142–3159, doi:10.1002/jgrb.50207.

1. Introduction

[2] Large megathrust earthquakes frequently trigger aseismic frictional afterslip on the megathrust in regions that are complimentary to those that slipped coseismically [e.g., *Miyazaki et al.*, 2004; *Ozawa et al.*, 2004; *Baba et al.*, 2006; *Hsu et al.*, 2006; *Pritchard and Simons*, 2006; *Perfettini et al.*, 2010; *Vigny et al.*, 2011; *Ozawa et al.*, 2012]. The amplitude of afterslip is generally estimated to range from tens of centimeters to several meters (partially dependent on the size of the mainshock, the time span of the observations, and the approach used to infer afterslip), and the location can range from near the trench to as deep as 100 km. Aftershocks tend to cluster along the boundary between the coseismic and postseismic slip zones [e.g., *Hsu et al.*, 2006; *Agurto et al.*, 2012; *Ozawa et al.*, 2012]. The observed spatial and temporal correlation between afterslip and aftershocks, and the small contribution of the latter to the total postseismic energy release, suggest that aftershocks are at least partly triggered by afterslip [*Perfettini and Avouac*, 2004; *Hsu et al.*, 2006; *Pritchard and Simons*, 2006; *Perfettini et al.*, 2010]. All these observations suggest that megathrust frictional properties are heterogeneous, allowing interfingering and interplay of seismic and aseismic slip from the trench all the way down to 100 km. However, it is generally difficult to really assess true differences in fault properties due to heterogeneity in models resolution.

Additional supporting information may be found in the online version of this article.

[1] California Institute of Technology, Pasadena, California, USA.
[2] Géoazur, Université de Nice Sophia-Antipolis, CNRS, Observatoire de la Côté d'Azur, Valbonne, France.
[3] Jet Propulsion Laboratory, La Cañada, California, USA.
[4] University of Hawaii, Honolulu, Hawaii, USA.
[5] Ohio State University, Columbus, Ohio, USA.
[6] University of Liverpool, Liverpool, UK.
[7] École Normale Supérieure, Paris, France.
[8] University of Memphis, Memphis, Tennessee, USA.
[9] Université Joseph Fourier, Grenoble, France.

Corresponding author: Y.-n. N. Lin, California Institute of Techology, C100-23, 1200 E California Blvd., Pasadena, CA 91125, USA. (ninalin@gps.caltech.edu)

2169-9313/13/10.1002/jgrb.50207

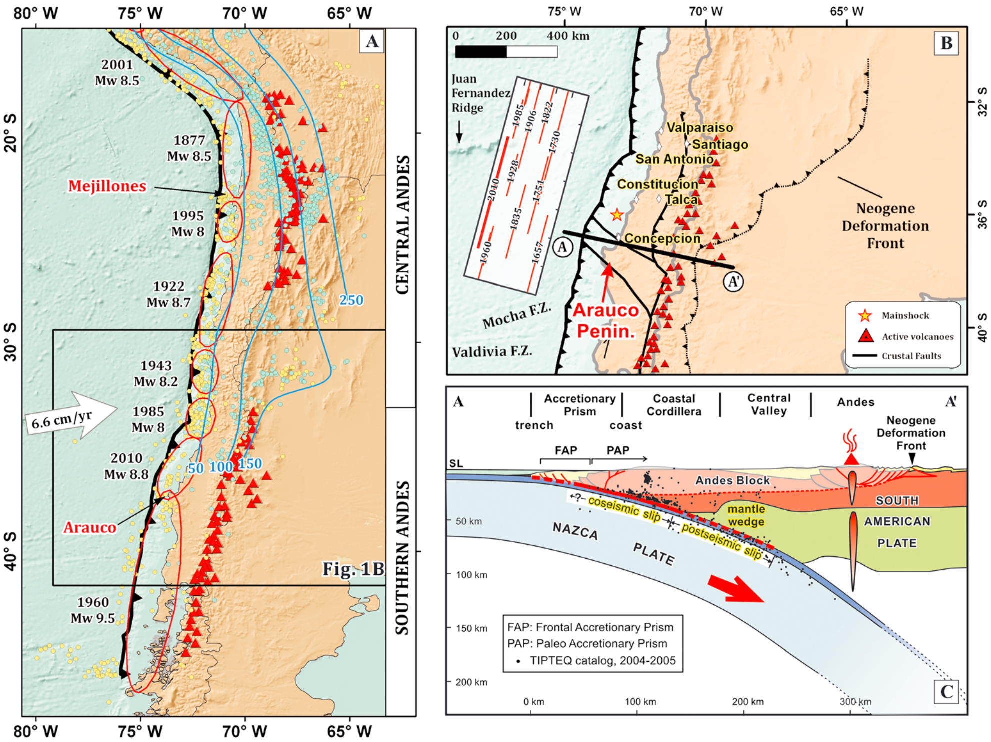

Figure 1. (a) Regional tectonic map showing slab isodepth contours (blue lines) [*Cahill and Isacks*, 1992], $M >= 4$ earthquakes from the National Earthquake Information Center catalog between 1976 and 2011 (yellow circles for depths less than 50 km, and blue circles for depths greater than 50 km), active volcanoes (red triangles), and the approximate extent of large megathrust earthquakes during the past hundred years (red ellipses) modified from *Campos et al.* [2002]. The large white vector represents the direction of Nazca Plate with respect to stable South America [*Kendrick et al*., 2003]. (b) Simplified seismo-tectonic map of the study area. Major Quaternary faults are modified after *Melnick et al*. [2009] (black lines). The Neogene Deformation Front is modified from *Folguera et al*. [2004]. The west-vergent thrust fault that bounds the west of the Andes between 32° and 38°S is modified from *Melnick et al.* [2009]. (c) Schematic cross-section along line *A–A′* (Figure 1b), modified from *Folguera and Ramos* [2009]. The upper bound of the coseismic slip coincides with the boundary between the frontal accretionary prism and the paleo-accretionary prism [*Contreras-Reyes et al*., 2010], whereas the contact between the coseismic and postseismic patch is from this study. The thick solid red line and dashed red line on top of the slab represent the approximate coseismic and postseismic plus interseismic slip section of the subduction interface. The thin red and grey lines within the overriding plate are active and inactive structures in the retroarc, modified from *Folguera and Ramos* [2009]. The red dashed line underneath the Andean Block represents the regional décollement. Background seismicity is from the TIPTEQ catalog, recorded between November 2004 and October 2005 [*Rietbrock et al*., 2005; *Haberland et al*., 2009].

[3] In this study, we estimate the distribution of coseismic and postseismic slip to assess the spatial variability of frictional properties on the south-central Chilean megathrust. As inferred from the strong correlation between coseismic slip patches and large-amplitude gravity anomalies in the region of a majority of (but not all) recent large earthquakes [*Song and Simons*, 2003], the along-strike variations in frictional behavior appear to persist over multiple earthquake cycles [*Song and Simons*, 2003; *Wells et al*., 2003; *Loveless et al*., 2010]. Several long-lived geologic features are also correlated with differences in slip behavior on the megathrust. For example, the most prominent patch of aseismic fault slip after the Pisco earthquake in central Peru coincides with the subducting Nazca ridge, which seems to have repeatedly acted as a barrier to seismic rupture propagation in the past [*Perfettini et al*., 2010]. The region of peak afterslip after the Antofagasta earthquake lies immediately beneath the Mejillones Peninsula, a proposed segment boundary during multiple seismic events, whose Quaternary deformation history is consistent with postseismic uplift [*Pritchard and Simons*, 2006; *Béjar-Pizarro et al*., 2010; *Victor et al*., 2011]. Along the Sumatran megathrust, the segment boundary beneath the Batu Islands also correlates with the subduction of the Investigator Fracture Zone [*Chlieh et al*., 2008].

[4] South-central Chile is an ideal natural laboratory to study the different stages of the seismic cycle and the role of purported seismic barriers because of the information available on past seismic ruptures, strain accumulation in the interseismic period, and the seismological and geodetic constraints on the recent Maule earthquake [*Ruegg et al*., 2002; *Moreno et al*., 2008; *Ruegg et al*., 2009; *Moreno et al*., 2010; *Delouis et al*., 2010; *Lay et al*., 2010; *Vigny et al*., 2011; *Lorito et al*., 2011]. The Arauco Peninsula is of particular interest because it coincides with the boundary

between the $Mw = 8.8$ 2010 Maule and the $Mw = 9.5$ 1960 Valdivia earthquakes (Figure 1a), and in particular may be the location of the 1960 Valdivia earthquake's $Mw = 8.1$ foreshock that was located very close to Concepción [*Cifuentes*, 1989]. Thus, the region of the megathrust below the Arauco Peninsula area has acted as a seismic barrier over at least a few hundred years [*Barrientos and Ward*, 1990; *Moreno et al.*, 2009; *Delouis et al.*, 2010; *Lay et al.*, 2010]. *Melnick et al.* [2009] showed that the peninsula is a zone of rapidly accumulating geological deformation and further proposed that the Arauco acts as a permanent barrier to propagating seismic ruptures on the million-year time scale. They suggest that the Arauco barrier results from the juxtaposition of heterogeneous metamorphic rocks with homogeneous intrusive rocks (Figure 1b), causing a compositional and hence mechanical discontinuity in the crust all the way down to the plate interface. A possible alternative is that the Arauco Peninsula would overlie a section of the megathrust that is dominantly aseismic. Zones of aseismic creep have been proposed to act as permanent barriers based on numerical simulations [*Kaneko et al.*, 2010] and observations [e.g., *Chlieh et al.*, 2008; *Konca et al.*, 2008]. To explore this issue, we infer the distribution of coseismic and postseismic slip associated with the 2010 Maule earthquake and estimate the frictional properties along the megathrust.

[5] To assess the uncertainties and resolution in different slip models, we first derive our own coseismic slip model by using an expanded set of available GPS, InSAR (Interferometric Synthetic Aperture Radar), teleseismic, and tsunami data. We then derive a postseismic slip model relying on GPS and InSAR observations. We integrate these slip models with the distribution of aftershocks to further illuminate the seismic/aseismic behavior of the megathrust. Finally, we discuss the implications of these slip patterns in terms of associated potency or equivalent moment and implications for the frictional behavior of the megathrust.

2. The 2010 Maule Earthquake and Its Seismotectonic Settings

[6] Prior to 2010, the Concepción-Constitución region experienced three large historical megathrust earthquakes in 1730, 1751, and 1835 (Figure 1b) [*Campos et al.*, 2002; *Lomnitz*, 2004]. Among these large historic events, the 1730 $M\,8.5 \sim 9$ Great Valparaiso earthquake generated a sizable tsunami [*Lomnitz*, 2004]. The 1751 $M = 8.5$ Concepción earthquake generated an even larger and more destructive tsunami. The last large earthquake, with an estimated magnitude of 8.5, has been described by Charles Darwin during the voyage of the HMS *Beagle* in 1835 [*Darwin*, 1851]. He and captain FitzRoy reported numerous geological phenomena that accompanied the earthquake, including coseismic coastal uplift/subsidence, postseismic deformation, tsunami waves of intermediate amplitude, and volcanic activity. Later in 1928, a smaller event, the $M = 7.9$ Talca earthquake devastated the towns of Talca and Constitución and produced a local tsunami height of only 1.5 m [*Beck et al.* 1998]. During the 1960 Valdivia earthquake, the $Mw = 8.1$ foreshock ruptured only the southernmost part of this segment [*Cifuentes*, 1989]. Thus, for the majority of the Concepción-Constitución segment, there had been no major subduction earthquakes since 1835 [*Beck et al.*, 1998; *Campos et al.*, 2002]. The potential for a *Mw* 8–8.5 earthquake in this region, based on the seismic gap hypothesis, was recognized before the 2010 event [*Ruegg et al.*, 2009], although *Lorito et al.* [2011] argued that the overall slip distribution of the 2010 event is inconsistent with that expected from the seismic gap hypothesis [*Campos et al.*, 2002; *Ruegg et al.*, 2002; *Moreno et al.*, 2008; *Ruegg et al.*, 2009; *Madariaga et al.*, 2010; *Moreno et al.*, 2010].

[7] The 1960 *M* 9.5 South Chile earthquake occurred to the south of the Concepción-Constitución segment in a region referred to as the Valdivia segment [*Cifuentes*, 1989; *Barrientos and Ward*, 1990] (Figure 1a). This earthquake was preceded historically by earthquakes in 1575, 1737, and 1837 [*Lomnitz*, 2004]. The 1575 and 1837 earthquakes produced only small tsunamis at the Río Maullín estuary in the center of the 1960 rupture and they are now believed to be considerably smaller than the 1960 event [*Lomnitz*, 2004; *Cisternas et al.*, 2005] (Figure 1a). Between this segment and the Concepción-Constitución segment lies the Arauco Peninsula, a major anomaly along the Pacific margin of South America in terms of coastline morphology and trench-to-coast distance (Figure 1a).

[8] The 2010 Maule earthquake nucleated northwest of Concepción [*Delouis et al.*, 2010; *Lay et al.*, 2010], with an epicenter located at 36.41°S and 73.18°W as determined using high-rate GPS records [*Vigny et al.*, 2011]. The rupture appears to have propagated bilaterally through two major asperities and caused severe damage to the city of Constitución, Santiago, Talca, and various others (Figure 1b) [*Astroza et al.*, 2010]. The hinge line between surface uplift and subsidence generally lies along the coastline. The only exception is the Arauco Peninsula, where the hinge line cuts through the east of the peninsula and where coastal uplift of up to 240 ± 20 cm was observed [*Vargas et al.*, 2011]. This observation alone points to the peculiar nature of the Arauco Peninsula. Tsunami waves affected the coastal regions between the cities of Valparaíso and Valdivia, with a peak runup of 29 m on a coastal bluff at Constitución. In most places runup heights are less than 10 meters [*Fritz et al.*, 2011].

[9] Currently there are at least six different published coseismic slip models (see supplementary materials of *Vigny et al.* [2011]; also see *Moreno et al.* [2012]). Major differences between these models include: (1) the updip extent of the primary slip zone (defined by 5 m slip contour), which may extend to the trench (modeling with teleseismic data only, e.g., *Lay et al.* [2010]), stop at 5–10 km (modeling with geodetic data only, e.g., *Tong et al.* [2010]; *Vigny et al.* [2011]; *Moreno et al.* [2012]), or even stop 10–20 km downdip from the trench [e.g., *Delouis et al.*, 2010; *Lorito et al.*, 2011]; (2) the center of the southern slip patch may be to the north of the Arauco Peninsula [*Delouis et al.*, 2010; *Lay et al.*, 2010], right under the peninsula [*Tong et al.*, 2010; *Lorito et al.*, 2011; *Moreno et al.*, 2012], or to the west of the peninsula [*Vigny et al.*, 2011]. These published models of fault slip adopt different forms of regularization and boundary conditions and also consider different data sets, thereby making it difficult to compare models. In this study, we develop our own coseismic slip model. By doing so, we can better understand the resolution limit, the contribution and consistency of different data sets, the impact of regularization terms, and the extent to which we can use these models to extract reliable information on fault zone behavior. More importantly, we ensure that our coseismic

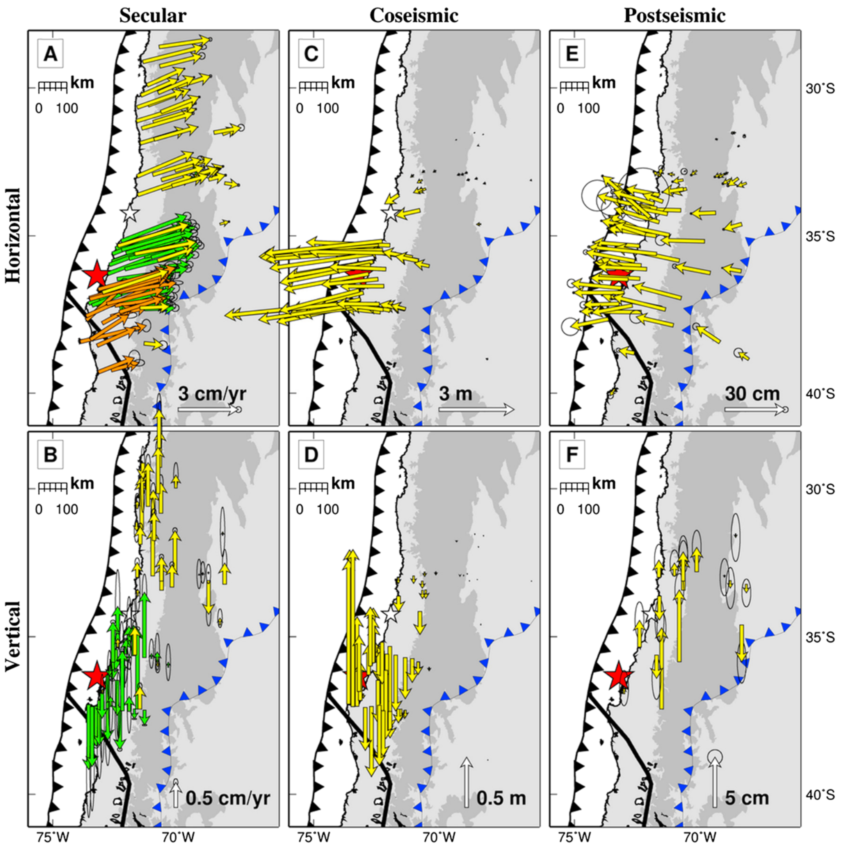

Figure 2. Horizontal and vertical secular interseismic velocities (left), coseismic displacement (middle) and postseismic displacement spanning the period between the 1st and 488th day after the mainshock (right). Note that for the postseismic displacement, when actual data time span for a given record does not cover this whole period, we have extrapolated it to represent the deformation between the 1st and 488th day using principal component analysis-based inversion method,. Yellow vectors are derived from this study; green vectors and orange vectors in Figures 2a and 2b are from are from *Ruegg et al*. [2009] and *Moreno et al*. [2008], respectively. The blue barbed line corresponds to the Neogene Deformation Front. The red and white stars represent the epicenter of the mainshock and the Pichilemu earthquake, respectively. The dark grey region is bounded by the 1000 m contour line, approximately the boundary of the Andes.

and postseismic models are affected by the same potential bias introduced by the inversion procedure and the simplifications made to compute the Green's functions.

3. Data

[10] We combined GPS data from multiple networks (see Table S1 in the supporting information), resulting in a total of 127 three-component continuous records. We use a conventional least-squares approach to separate postseismic deformation from other signals, including secular rates, coseismic jumps (e.g., the Maule main shock, Pichilemu aftershock, and other events), and seasonal variations (Figure 2). For the short time series whose records start after the Maule earthquake, we determined their horizontal secular rates and seasonal variations by using velocities from the long time series and from published literature (Figure 2a) [*Moreno et al*., 2008; *Ruegg et al*., 2009]. We did not carry out the same corrections on the vertical components due to the large uncertainties in their secular rates (Figure 2b) [*Ruegg et al*., 2009], but chose to use only the long time series in our postseismic model. In the end, 79 three-component coseismic displacements are determined with 27 of them, mostly far-field stations, augmenting the data set described in *Vigny et al*. [2011]; 66 cGPS stations are used in the postseismic model, among which 22 vertical records were considered usable.

[11] By inspecting the cumulative postseismic displacements (Figures 2e and 2f) we found the peak horizontal displacement near the coast as expected; however, the peak vertical displacement occurs near the Andes. This pattern is different from any analytical prediction of a thrust fault system in an elastic half-space or layered half-space (Figures 2c and 2d). The peculiarity in the postseismic data therefore indicates such models will have difficulty in fitting all the postseismic data with simple models of slip restricted to the megathrust.

[12] Besides GPS time series, the Japanese L-band Advanced Land Observation Satellite (ALOS) provided continuous monitoring along this region after the earthquake for almost one year (Figure 3). Among the data ALOS acquired, wide-swath descending track 422 forms the most continuous image of the coseismic and early postseismic deformation field (Figures 3 and 4). In addition to this wide-swath track, ascending tracks 111 through 119 provide continuous spatial coverage over different time spans all the way through the end of 2010.

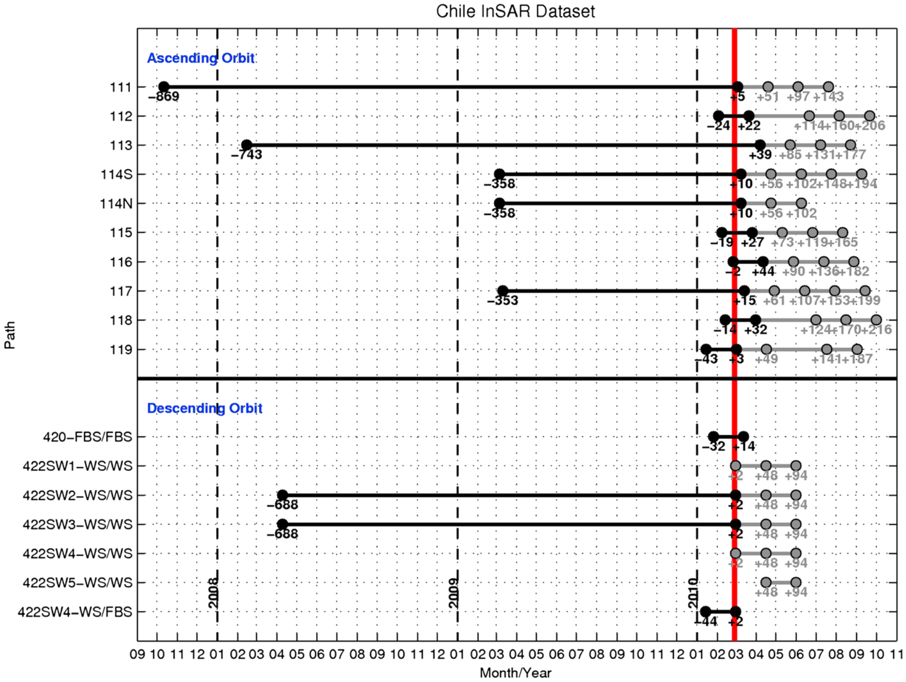

Figure 3. ALOS PALSAR acquisitions used in this study. FBS stands for fine mode single polarization mode while WS stands for wide swath data. Black lines indicate coseismic pairs and gray lines indicate postseismic pairs. Numbers under each acquisition dot represent the number of days before or after the earthquake.

We refer the reader to the supporting information for more details regarding the GPS data processing, corrections applied to coseismic and postseismic InSAR images and the issues associated with data sampling.

4. Coseismic Slip Model

[13] To solve for the distribution of coseismic slip of the Maule earthquake, we perform a joint inversion of all the static data previously described (i.e., InSAR and GPS) and teleseismic body waves (Figure 5; also see supporting information for model details) using the method of *Ji et al.* [2002]. Consistent with previous models, our preferred coseismic slip model indicates that rupture was bilateral and extended over 500 km (Figure 5c). The slip model defines a relatively continuous band of significant slip extending ~100 km down dip that parallels but extends only slightly below the coastline (Figure 6). The distribution of slip is dominated by a region of high slip north of the epicenter (centered around latitude S35°) with a maximum slip of 16 m, close to the 15 m peak slip from *Vigny et al.* [2011]. In the southern part of the rupture, near the Arauco Peninsula, the slip distribution is more irregular with slip amplitudes not exceeding 8 m.

[14] The coseismic model allows us to reproduce the main characteristics of the different data sets (Figures 4–6). There are several residual fringes in some of the InSAR tracks. However, given the orientation of those residual fringes, we suspect unmodeled propagation delays due to ionospheric perturbations or nonoptimal orbital ramp corrections. In the case of the GPS data, all vectors are fit extremely well with the exception of the vertical component of the profile extending eastward from Constitución around latitude S35.3°. In essence, the region of observed coseismic subsidence is narrower (i.e., with a more limited eastward extent) than what our model produces (Figure 6). Extending the downdip limit of our fault geometry allows improvement in the fit to the vertical displacements by allowing localized slip patches beneath the problematic stations near the Andes. Given the correlation of these deep slip patches with the sparse location of the GPS stations, we are not sure if they are reliable or if they reflect, for instance, an oversimplification in the model fault geometry and elastic model. We note that *Moreno et al.* [2012] adopted a finite-element model that takes more subtleties in the fault geometry into account, but their results also show the same residuals in the GPS vertical components near the Andes. We return to this point later in the discussion section.

[15] To limit the potential trade-off between rupture time and rupture duration, which is enhanced by the bilateral rupture [e.g., *Lay et al.*, 2010], and to limit the nonuniqueness of the solution, we impose a narrow prior range of 2.5–3.0 km·s^{-1} for the rupture velocity [*Delouis et al.*, 2010; *Vigny et al.*, 2011] and allow each patch to rupture only once for a maximum of 14 s. Despite these strong prior constraints on the solution, we obtain a slip distribution similar to the geodetic-only inversion (Figure S3) with a reasonable fit of the complex teleseismic *P* wave train (Figure 5).

[16] Coseismic slip in our preferred model stops about 15 km from the trench at the latitude of maximum slip (Figure 5). This behavior is similar to the models of *Delouis et al.* [2010] and *Lorito et al.* [2011], who also included multiple data types in their inversions. This slip extent agrees well with the 90% coupling patch determined by the interseismic GPS measurements during the past decade [*Métois et al.*, 2012], although the resolution of the near-trench portion of the megathrust is significantly

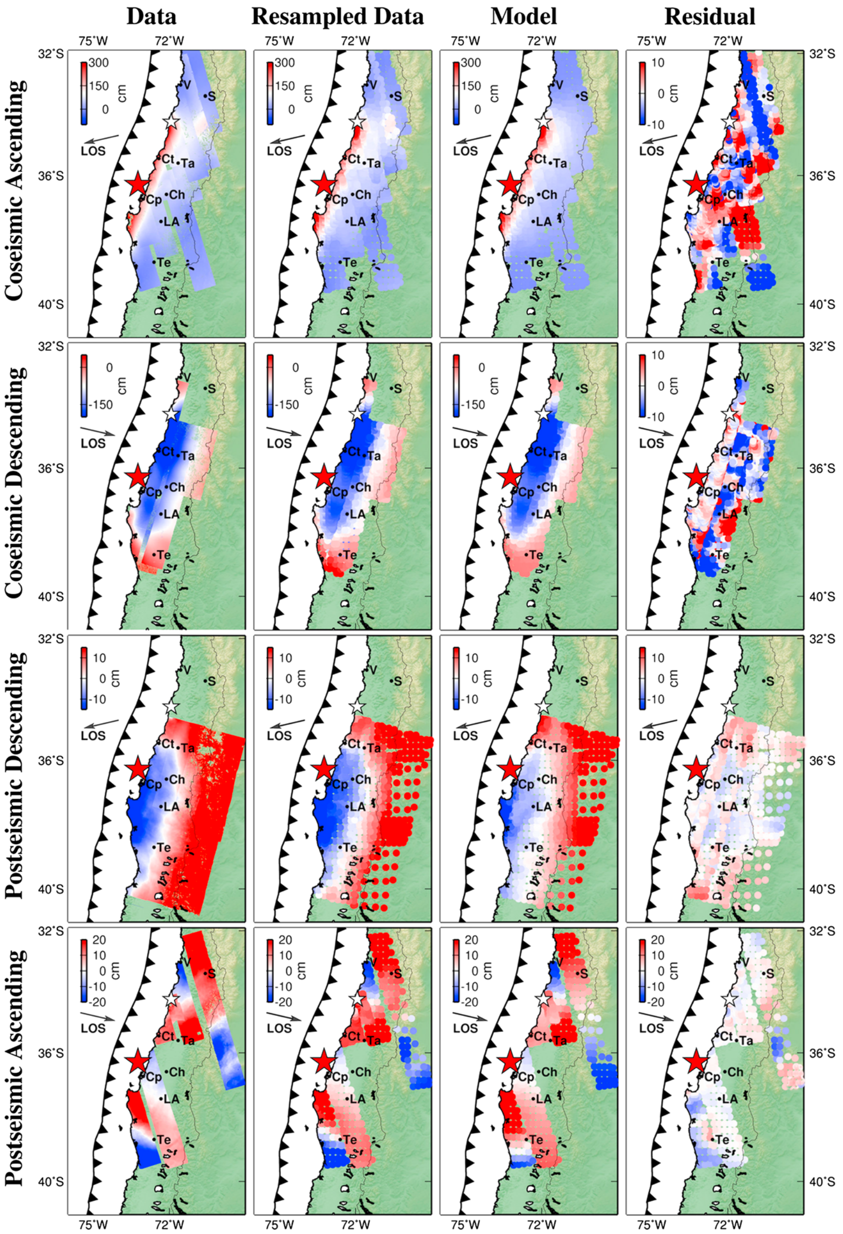

Figure 4. The original, resampled, modeled InSAR data, and the model residuals for both the coseismic and postseismic tracks. Red and white stars are for the Maule and Pichilemu earthquakes, respectively. Notice that for the postseismic ascending images, different tracks cover different time spans (Figure 3) and therefore they cannot form a continuous map as the postseismic descending tracks.

reduced. Coseismic slip on the shallowest part of the megathrust is difficult to constrain from on-land geodetic data alone because of the decreases in resolution with distance from the observations (illustrated by a checkerboard test in Figure S4). In addition to this well-established limitation, resolution is also affected by model errors, that is, the use of approximate Green's functions, not taking into account complex fault geometry (e.g., splay-faults), the effect of topography, and of gradients in material properties [e.g., *Hsu et al.*, 2011]. To illustrate just one of these effects, we estimated a solution adopting a homogeneous elastic half-space instead of a 1-D layered half-space. The result (Figure S8) shows a slip distribution very similar to our preferred model but with slip extending closer to the trench. This simple test illustrates that the extent of shallow slip may be fairly sensitive to the assumed velocity structure. This conclusion is also supported by the checkerboard and sensitivity tests performed on the coseismic and postseismic models (Figures S4, S6, and S7).

[17] On the other hand, tsunami data recorded in the open ocean is sensitive to the outer extent of the megathrust rupture and can be used to constrain the rupture of large subduction earthquakes [e.g., *Satake*, 1993; *Piatanesi and Lorito*, 2007; *Sladen and Hébert*, 2008; *Sladen et al.*, 2010; *Lorito et al.*, 2011; *Simons et al.*, 2011]. The tsunami simulation for our slip model, using the tsunami model described in *Heinrich et al.*, [1998] and *Hébert et al.* [2001], provides good predictions of the tsunami waveforms at nearby tide

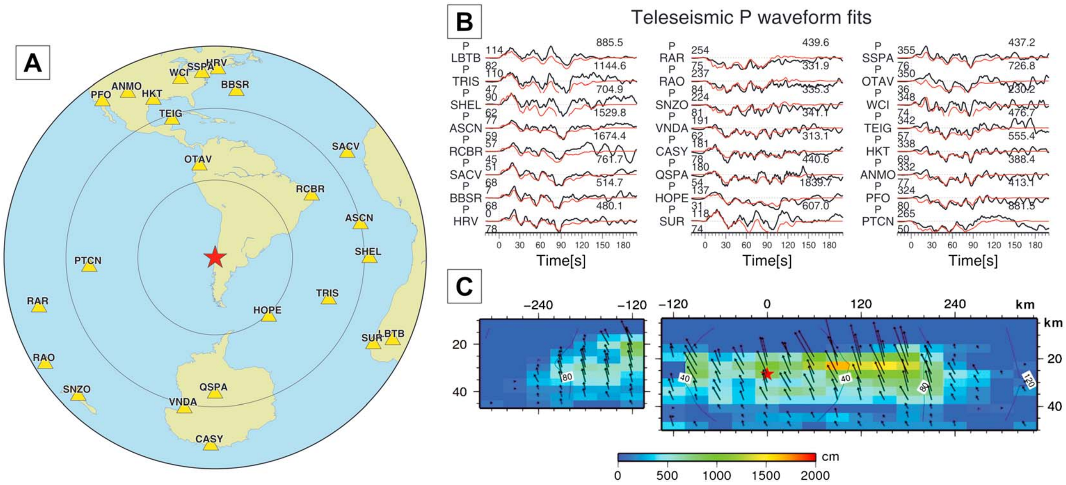

Figure 5. (a) The global distribution of seismic stations used in the coseismic model. Circles are every 30° of azimuthal distance. (b) Comparison of the observed (black) and modeled seismic waveforms (red) of the kinematic finite fault model. (c) The slip magnitude (colors), rake (arrows) and rupture propagation time in seconds (isochrones) for that same kinematic model.

gauges (with the exception of the Ancud and Corral tide gages located deep inside complex bays) and open-ocean buoys, but arrives too early at most stations south of the main tsunami energy beam (Figure 7). Back-projection of the tsunami (Figure S9) indicates that only buoy 51406 is directly sensitive to the slip distribution updip of the main slip patch (see supporting information). Even considering the effects of rupture propagation, the tsunami simulation of our preferred slip model arrives 4 min too early at that 51406 station (Figure 7), suggesting that it is unlikely that the slip extended even closer to the trench. This argument is consistent with the study of *Lorito et al*. [2011] who included the tsunami records in their inversion of the slip distribution. However, this result mainly relies on one distant station and we cannot

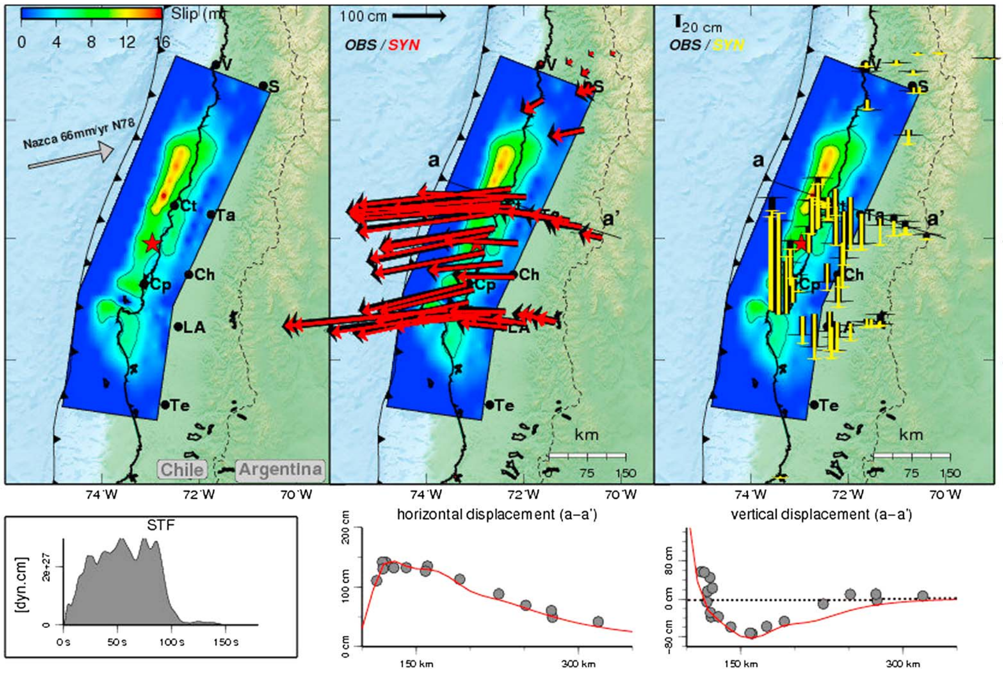

Figure 6. (left) Coseismic slip with 5 m contour intervals from the best-fit model with the source time function of the solution plotted below. (center and right) Black vectors indicate the observed GPS data; red and yellow vectors indicate modeled results in the horizontal and vertical components, respectively. The profile (aa') shows the predicted (red line) and observed (grey solid dots) surface displacements at the latitude of the main asperity, around latitude 36°S. Notice that for the vertical components (right), the slip model predicts a displacement field of longer wavelength than the observed data. See text for a discussion of this discrepancy. STF: Source time function. Ch: Chillán; Ct: Constitución; Cp: Concepción; LA: Los Angeles; Ta: Talca; Te: Temuco; S: Santiago; V: Valparaiso.

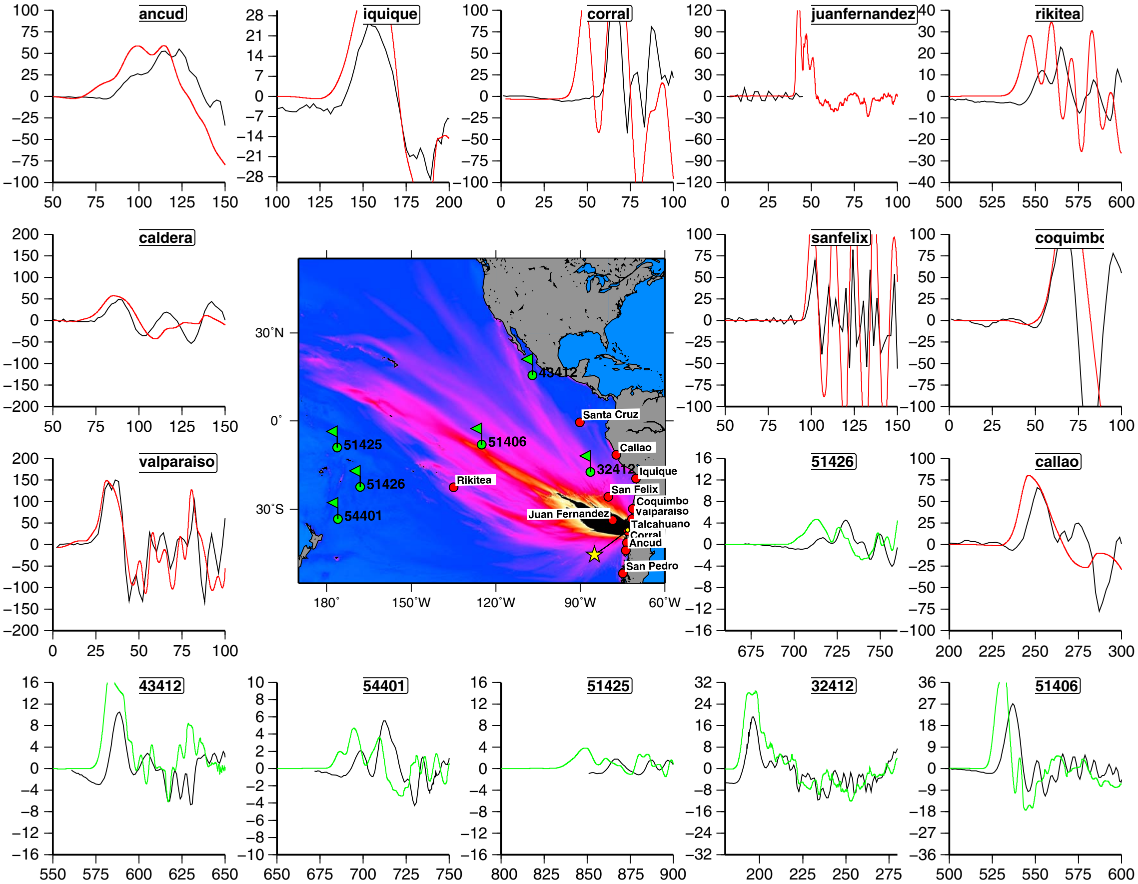

Figure 7. Tsunameter records as predicted by our preferred kinematic source model—these data were not used in the construction of the model. Black lines are observations; red and green lines are the modeled waves for tide gauges and deep-sea bottom pressure gauges, respectively. The map in the middle shows the predicted maximum open ocean wave heights. No time shift has been applied to the records.

exclude the possibility that dispersion effects not taken into account in the shallow-water approximation could have biased the timing of that tsunami record.

[18] The along-strike extent of our preferred slip model, as defined by areas with slip in excess of 5 m, is about 460 km. The northern edge of the slip model (at latitude 34°S) is remarkably sharp, a characteristic also visible in the source time function which abruptly stops after 100 s. This sharp rupture termination may have promoted the static triggering of the Pichilemu aftershock sequence [*Farias et al.*, 2010; *Vigny et al.*, 2011]. The southern slip patch is centered under the Arauco Peninsula, extending slightly northwestward. This pattern agrees with several published results in general [*Tong et al.*, 2010; *Lorito et al.*, 2011; *Moreno et al.*, 2012]. The total seismic moment of our slip model is 2.25e + 21 N·m, equivalent to *Mw* 8.8, a value close to that estimated by GCMT (1.86e + 21 N·m).

5. Postseismic Slip Model

[19] There are a few differences in the construction of the coseismic and postseismic slip models. To derive the time-dependent finite source kinematic models, we use the principal component analysis-based inversion method [*Kositsky and Avouac*, 2010; *Lin et al.*, 2010]. We build a larger fault plane because postseismic slip may take place at greater depth. The fault plane for the postseismic model assumes a curved shape to fit the geometry imaged by various techniques (seismicity, tomography, and so on). In addition, we apply the sensitivity-modulated regularization scheme from the work of Ortega-Culaciati et al. (in preparation, 2013) to take care of the model resolution at different depths. The details of these changes are described in the supporting information.

[20] The RMS residual is 0.9 cm for the horizontal GPS observations and 1.1 cm for vertical components. These values reflect both measurement and prediction error. We find systematic residuals for the GPS observations near the Andes, including SJAV, CURI, MAUL, and ELA2 in the north and UDEC, ANTC, LAJA, LMNS, and ESQA in the south (Figure 8). The E-W components of the time series of these stations display a slower westward increase during the initial postseismic period when compared with other stations, but a faster trend after the first 200 days. The misfit to these stations suggests a modeling inadequacy in our layered elastic half-space afterslip model. We discuss these misfits further in section 6.4

[21] In Figure 9 we compare three postseismic slip models, constrained by GPS horizontal components only, GPS horizontal plus vertical components, and three-component GPS plus InSAR data sets, respectively. Strike-slip motion in

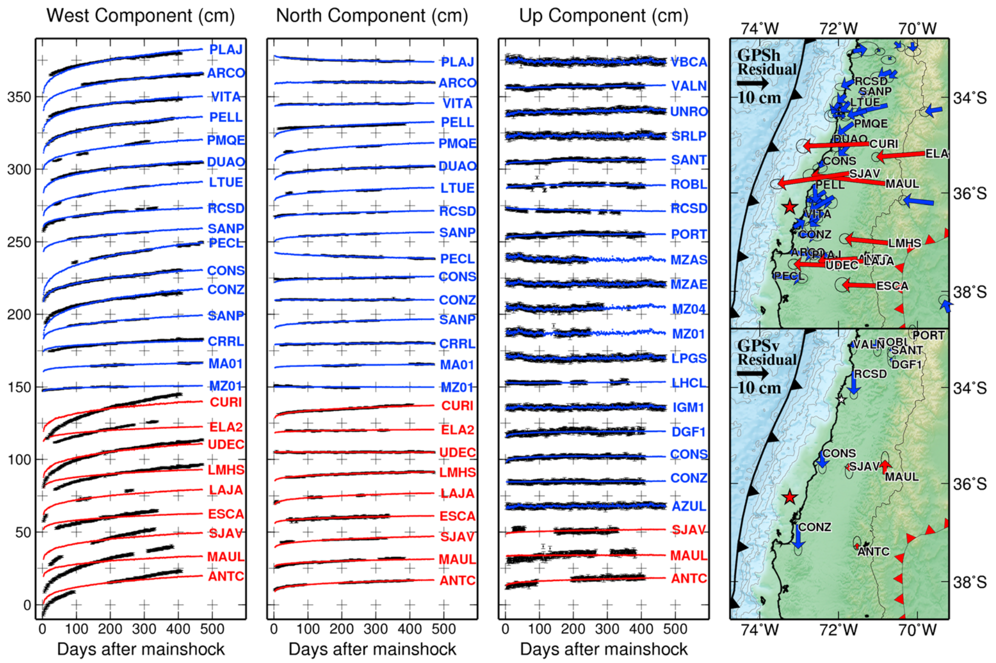

Figure 8. Time series of selected GPS stations. Blue lines and stations represent predicted time series that agree well with the data (black dots), whereas red lines and stations represent model prediction displaying large discrepancies with the data. The map views at the right panel show the residual vectors between the observed and modeled GPS components. The red stations are distributed along the Andes, indicating that the large systematic residuals are likely due to a common source.

these models is minor, so we can treat the slip as primarily dip-slip motion. The comparison of the patterns between the first two models (Figures 9a and 9b) reveals nuances, particularly the connectivity, in the afterslip patch downdip of the coseismic slip region. This elongated zone, designated as **A**, extends from almost 40 to 60 km at depth, with maximum slip of ~1.8 m over the first 488 days after the mainshock. This creeping zone generally agrees with the results from *Vigny et al.* [2011] but is more spatially focused, due to a combination of the augmented GPS and InSAR data and the differing forms of regularization employed. This elongated afterslip zone also coincides with the downdip slip deficit zone proposed by *Moreno et al.* [2012].

[22] Incorporating the InSAR data set (Figure 9c) allows us to resolve a shallow afterslip patch offshore of the Arauco Peninsula and a deep slip patch that is separated from the main slip patch. The offshore region of slip, designated as **B**, is the only region with slip shallower than 20 km. Slip on this patch is constrained primarily by InSAR observations, as we only have one near-coast GPS station between latitudes 38° and 40°S. This lack of GPS data is why this region of afterslip was not captured in the early model of *Vigny et al.* [2011]. A third slip patch that is not as shallow as patch **B** is located to the northern edge of the coseismic slip patch. This patch, designated as **C**, is between 20 and 40 km at depth. Its spatial extent agrees well with the results from *Vigny et al.* [2011]. Patch **B** and **C** together bound the southern and northern edge of the whole coseismic slip patch and agree with the Arauco and San Antonio intersegment area that define the Maule segment in *Métois et al.* [2012].

[23] The deep slip patch, designated as **D**, extends to 120–160 km at depth. This region of slip is spatially distinct from patch **A** and **B** located further updip. The slip on this patch is also primarily constrained by InSAR, because the residuals for the GPS observations in this region are large. It is therefore likely that our model maps some uncorrected noise in InSAR data (atmospheric noises in particular because this patch is close to the Andes) or other geophysical processes in the InSAR data onto the subduction interface. Given these issues, we do not interpret the slip in this patch further.

[24] Except for patch **B**, we do not see significant afterslip updip of the regions that slipped coseismically, i.e., from the trench to 20 km at depth. This result agrees with the nearly zero interseismic slip deficit in the updip portion of the megathrust [*Moreno et al.*, 2012]. Although the resolution of interseismic and postseismic slip is particularly poor there, it is possible that the shallowest portion of the megathrust might creep interseismically. However, *Agurto et al.* [2012] showed that some $M > 4$ earthquakes and associated seismically related afterslip occurred postseismically between March 2010 and March 2012 along the updip edge of the coseismic slip patch south of 35.3°S (also see supporting information). Given the trench-coast distance and the onshore distribution of GPS stations, it is possible that the extent and magnitude of shallow afterslip is beyond the resolution of this study. Our slip potency test (see supporting information) shows that some amount of shallow afterslip cannot be excluded, although the associated slip potency does not exceed ~10% of the total coseismic slip potency.

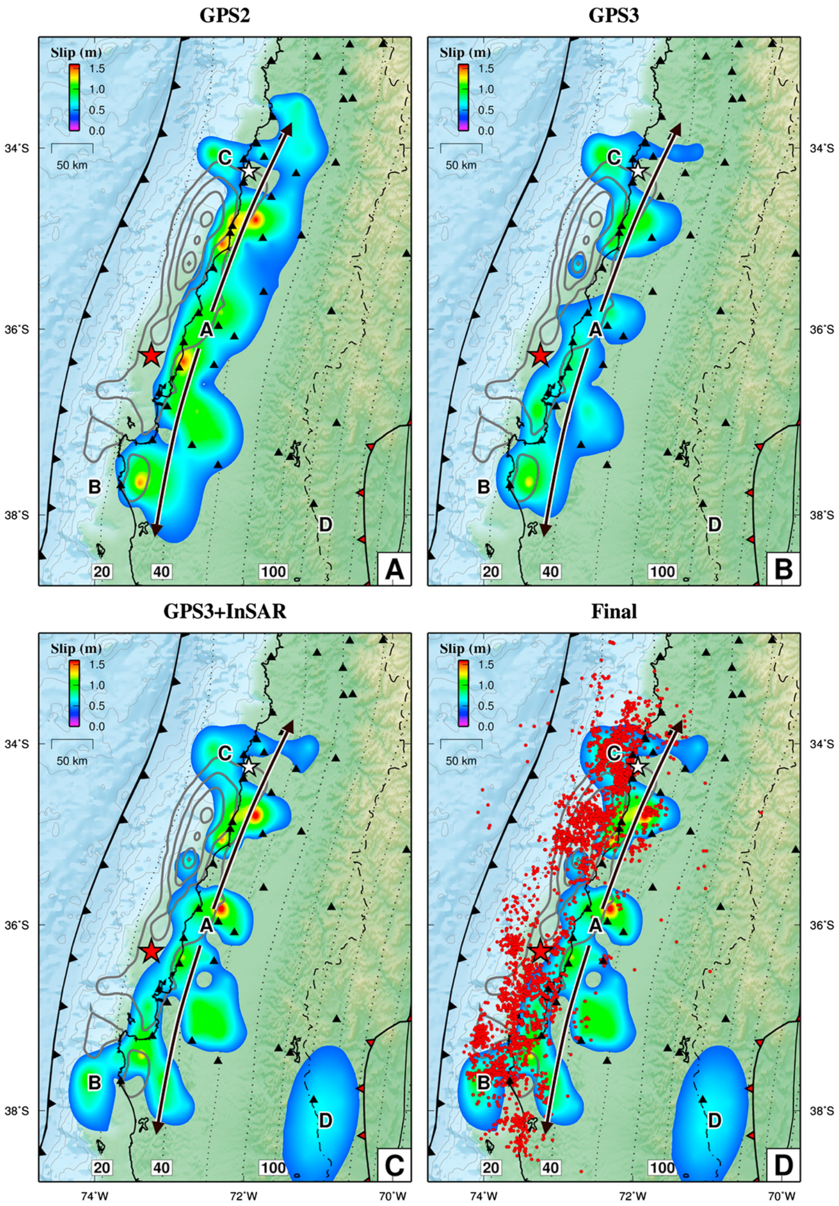

Figure 9. Comparison of the postseismic slip model between the 1st and 488th day constrained by (a) horizontal GPS observations only, (b) all three components of GPS observations, and (c) three component GPS observations plus InSAR data. The coseismic slip model is of 2.5 m contour intervals (gray lines). (d) The same afterslip model as Figure 9c. Red dots are aftershocks [*Rietbrock et al.*, 2012]. Black triangles represent the location of GPS stations. A is the afterslip downdip of the coseismic slip patch, with the black arrows indicating the along-strike extent. B and C correspond to two regions of afterslip that bound the southern and northern end of the coseismic slip patch. D is a deep slip patch that may reflect some tropospheric errors in the Andes.

6. Discussion

6.1. Postseismic Moment Release

[25] Acknowledging that geodetic data primarily constrain the potency associated with fault slip and not seismic moment, we estimate that the moment released by postseismic slip in 1.3 years is $3.6\sim5.1\ 10^{21}$ N·m ($Mw = 8.34\sim8.44$), equivalent to 20 ~ 30% of the coseismic moment. This ratio is similar to that of earthquakes of similar magnitude, such as the 2001 $Mw = 8.4$ Arequipa earthquake in southern Peru (20–40% in 1 year) [*Ruegg et al.*, 2001; *Melbourne et al.*, 2002] and the 2005 $Mw = 8.7$ Nias earthquake (>25% in 9 month) [*Hsu et al.*, 2006]. The relative magnitude of postseismic to coseismic moment seems to scale with the magnitude of the mainshock (Figure 10a). Smaller earthquakes tend to produce relatively less afterslip, such as the 1995 $Mw = 8.1$ Antofagasta earthquake (<20% in 1 year) [*Melbourne et al.*, 2002; *Chlieh et al.*, 2004; *Pritchard and Simons*, 2006] and 2007 $Mw = 8.0$ Pisco earthquake (7–28% in 1.1 years) [*Perfettini et al.*, 2010], whereas larger earthquakes tend to have larger values, such as the 2004 $Mw = 9.1$ Sumatra earthquake (30% in the first month and

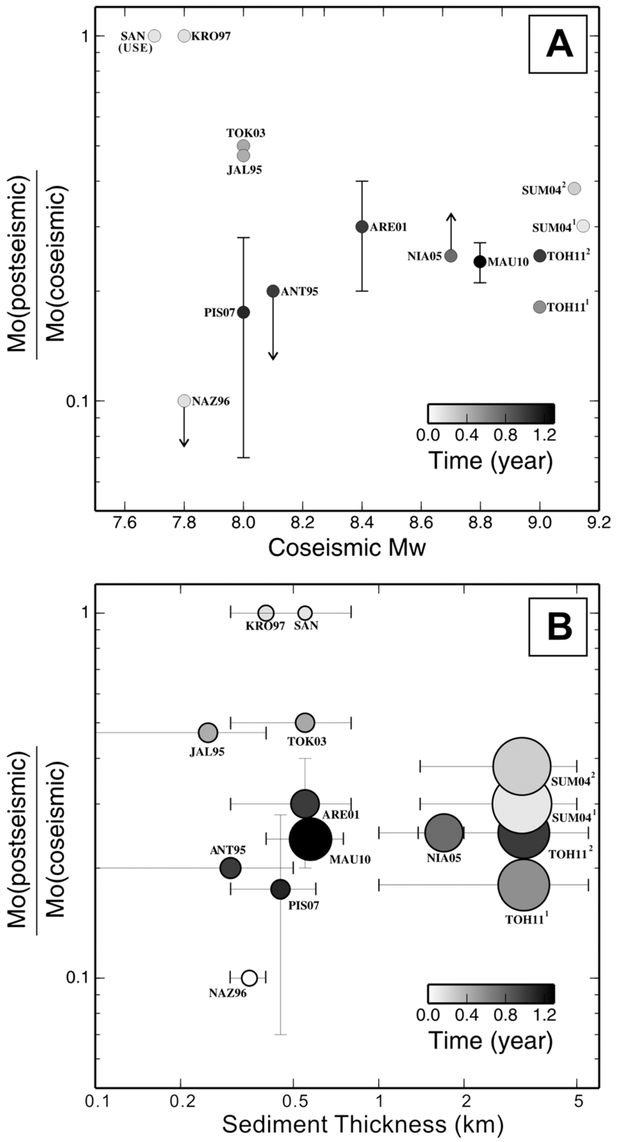

Figure 10. (a) Plot of the estimated postseismic-coseismic ratio as a function of coseismic moment for selected megathrust earthquakes. The ordinate is in log scale to reflect the relationship between *Mo* and *Mw*. The color scale of each dot represents the amount of time after the mainshock considered in each postseismic study. The code next to each circle is the first three letters of the event name and it occurrence year: ANT95, 1995 Antofagasta, Chile [*Melbourne et al*., 2002; *Chlieh et al*., 2004; *Pritchard and Simons*, 2006]; ARE01, 2001 Arequipa, Peru [*Ruegg et al*., 2001; *Melbourne et al*., 2002]; JAL95, 1995 Jalisco, Mexico [*Hutton et al*., 2001; *Melbourne et al*., 2002;]; KRO97, 1997 Kronotsky, Kamchatka [*Burgmann et al*., 2001; *Gordeev et al*., 2001]; MAU10, 2010 Maule, Chile (this study); NAZ96, 1996 Nazca, Peru [*Pritchard et al*., 2007]; NIA05, 2005 Nias, Indonesia [*Hsu et al*., 2006]; PIS07, 2007 Pisco, Peru [*Perfettini et al*., 2010]; TOH11, 2011 Tohoku, Japan [*Ozawa et al*., 2012; *Geospatial Information Authority of Japan*, 2012]; TOK03, 2003 Tokachi-oki, Japan [*Miyazaki et al*., 2004; *Ozawa et al*., 2004; *Baba et al*., 2006]; SAN, 1989–1994 Sanriku-oki, Japan [*Kawasaki et al*., 1995; *Heki et al*., 1997; *Heki and Tamura*, 1997; *Nishimura et al*., 2000; *Kawasaki et al*., 2001; *Melbourne et al*., 2002; *Yagi et al*., 2003]; SUM04, 2004 Sumatra, Indonesia [*Hashimoto et al*., 2006; *Subarya et al*., 2006; *Chlieh et al*., 2007]. Arrows instead of error bars indicate the circles as the upper bound or lower bound of the values. "USE" under the letters SAN (Sanriku-Oki events) represents "ultraslow earthquake." (b) Plot of the estimated postseismic-coseismic ratio as a function trench sediment thickness. The size of the circles scales with the mainshock magnitude. Colors of the circles and name codes follow Figure 10a. The sediment thickness estimates are from multiple sources: *von Huene and Scholl* [1991], *Plank and Langmuir* [1998], and *Divins* [2003].

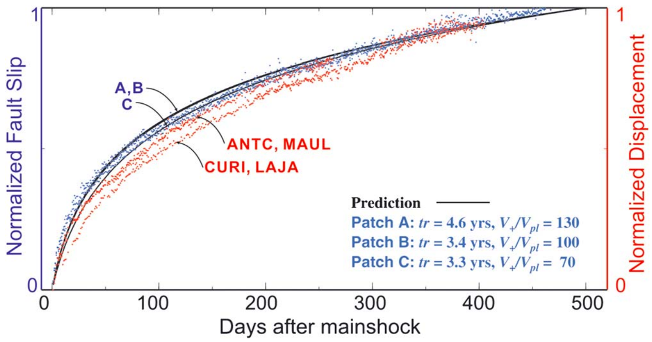

Figure 11. Normalized time-dependent fault slip over different postseismic slip patches from our model result (blue dots; see Figure 9d for locations). The normalized westward displacements over selected GPS stations are also shown for comparison (red dots; see Figure 8 for locations). Solid lines are the model predictions [*Perfettini et al.*, 2010].

38% in 3 months) [e.g., *Chlieh et al.*, 2007] and the 2011 $Mw = 9.0$ Tohoku earthquake (18% in 7 months [*Ozawa et al.*, 2012] and ~25% in 1 year [*Geospatial Information Authority of Japan*, 2012]) .

[26] *Pritchard and Simons* [2006] also pointed out that the amount of sediment subducted may also help modulate the postseismic behavior. As shown in Figure 10b, the relative magnitude of postseismic to coseismic moment increases with sediment thickness, although the correlation is less prominent due to the large variations in trench sediment thickness and the uncertainties in its estimation. We may even attribute the correlation back to the idea that thick trench sediments smooth out the slab topography and encourage large earthquakes [*Ruff*, 1989]. Such relationship seems to hold in many earthquakes, the most well-known of which is the 1.5 km thick trench sediments in southern Chile and the $Mw = 9.5$ 1960 Valdivia earthquake [*Scherwath et al.*, 2009; *Contreras-Reyes et al.*, 2010]. It is therefore difficult to tell which factor, the sediment thickness or the coseismic stress drop, contributes more to the afterslip behavior along the subduction interface.

[27] In both correlation plots, outliers exist. Smaller earthquakes can still be followed by afterslip having a large potency, such as the 1989–1994 Sanriku-oki earthquake sequences in Japan (ranging from $Mw = 6.9$ to $Mw = 7.7$) [*Heki and Tamura*, 1997; *Kawasaki et al.*, 2001]. Because the moment release rate is so large (100% in $5 \sim 50$ days) these postseismic events were further defined as "ultraslow earthquakes" and may likely result from very unique source properties on the subduction interface [*Kawasaki et al.*, 1995]. Other examples include the large afterslip of the 2005–2008 $Mw \sim 7$ earthquakes along the Japan Trench megathrust, whose postseismic moment release exceeded that of the corresponding coseismic events [*Suito et al.*, 2011]. Because the number of earthquakes is small and obvious exceptions exist, more case studies are required to elucidate the possible correlation between the coseismic and postseismic moment release.

6.2. Spatial Friction Variations and the Seismic Barrier

[28] The cumulative moment due to all aftershocks with $Mw > 3$ reported in the National Earthquake Information Center catalogue over the same period of time amounts to only $5.58e+10^{19}$ N·m, indicating that about 99% of the observed postseismic deformation was aseismic, a value even larger than that of the 2005 Nias earthquake (93%) [*Hsu et al.*, 2006]. *Agurto et al.* [2012] found that in the case of Maule aftershocks, the concentration of larger aftershocks ($M = 4 \sim 6$) at the boundary between coseismic and postseismic patches illuminates the region with the highest concentration of stress right after the mainshock, and the boundary of the regions of greatest aseismic afterslip. This region is also the loci of a majority of coseismic high-frequency radiators [*Lay et al.*, 2010]. Their spatial distribution depicts the region of frictional heterogeneities within the brittle-ductile transition zone, i.e., small discrete brittle asperities dotted amidst ductile creeping zone [*Ito et al.*, 2007; *Simons et al.*, 2011; *Meng et al.*, 2011]. However, this creeping zone is further bounded by a second band of aftershocks at the downdip margin [*Rietbrock et al.*, 2012], with lobes of afterslip patches sandwiched in between the upper and lower aftershock clusters (Figure 9d), mimicking the complex mosaic of phenomena revealed by the study of the 1995 Antofagasta earthquake in northern Chile and its corresponding afterslip and aftershocks [*Pritchard and Simons*, 2006]. These deeper aftershocks may result from slip on small stick-slip patches triggered by afterslip. Their locations suggest a nonmonotonic change from a stick-slip regime to a creeping regime with increasing depth.

[29] To explore the frictional properties of the fault patches that produced aseismic afterslip, we compute afterslip with a simple theoretical model. We calculate slip predicted from a one-dimensional rate-strengthening frictional sliding model, assuming that frictional stress increases linearly with the logarithm of the sliding velocity, as observed in laboratory experiments [*Marone*, 1998]. Based on this model and later analytical derivations [*Perfettini and Avouac*, 2004; *Perfettini et al.*, 2010], postseismic slip $U(t)$ evolves as

$$U(t) = V_{\mathrm{pl}} t_{\mathrm{r}} \log\left[1 + \left(V^+/V_{\mathrm{pl}} t_{\mathrm{r}}\right) t\right] \tag{1}$$

where t is time, V_{pl} is the plate convergence velocity, t_{r} is the relaxation time, V^+ can be viewed as the creeping velocity during the postseismic period, and the ratio V^+/V_{pl} represents the postseismic creep rate normalized by the long-term plate convergence velocity.

[30] For the elongated region of slip downdip of the coseismic slip patch (patch **A** in Figure 9), the shallow afterslip offshore of the Arauco Peninsula (patch **B**), and the afterslip that bounds the coseismic slip patch to the north near San Antonio (patch **C**), we find a very stable value of t_{r} of approximately 3.3–4.6 years and V^+/V_{pl} of 70–130 (Figure 11). We further convert V_{pl} and t_{r} to parameters more closely related to material properties, following the formulation described by *Perfettini and Avouac* [2004]. Using a value of coseismic Coulomb stress change of 3 MPa for the elongated downdip region, 0.5–1 MPa around the offshore Arauco Peninsula, and 2.5–3 MPa for the northern afterslip patch [*Lorito et al.*, 2011], we find $(a-b)\sigma_{\mathrm{n}} = 0.08$–$0.62$ MPa for patch **A**, 0.01–0.22 MPa for patch **B**, and 0.04–0.65 MPa for patch **C**, where σ_{n} denotes effective normal stress, and $a-b$ is the frictional parameter (see *Hsu et al.* [2006] for the steps of obtaining these ranges of $(a-b)\sigma_{\mathrm{n}}$ values).

[31] $a-b$ describes how the coefficient of friction varies as a function of the logarithm of sliding velocity, with positive

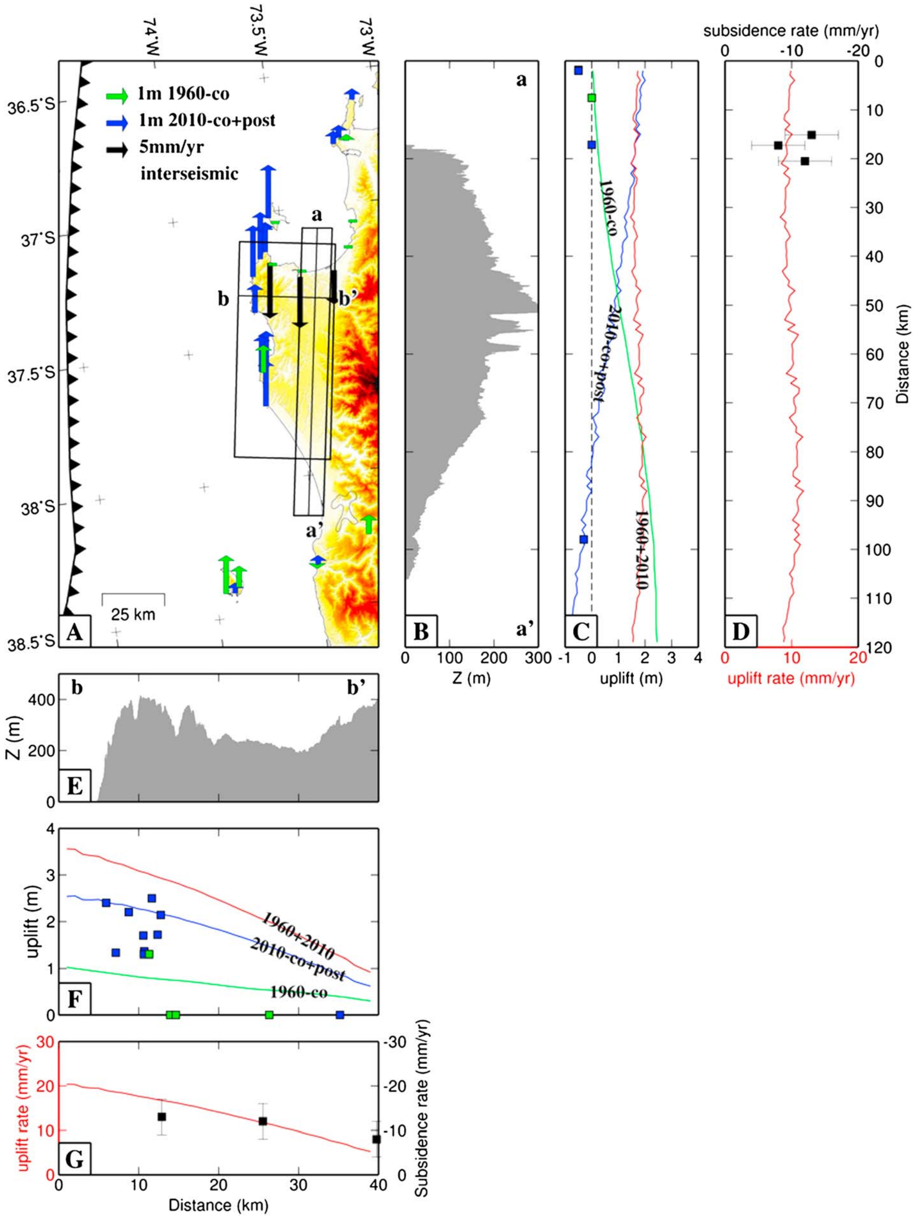

Figure 12. Topography, deformation and uplift/subsidence rate of the Arauco Peninsula along E-W and N-S directions. (a) Map of the Arauco Peninsula. *a*–*a*′ and *b*–*b*′ indicate locations of the profiles, with the bounding boxes showing the area of topography being projected onto the profiles. Green vectors and blue vectors are the in situ measurements of coseismic and early postseismic vertical displacement from the 1960 Valdivia earthquake [*Plafker and Savage*, 1970] and the 2010 Maule earthquake [*Vargas et al*., 2011]. Black vectors are the vertical velocities from campaign-mode GPS between 1996 and 2002 [*Ruegg et al*., 2009]. (b) Projected topography along the swath *a*–*a*′. Vertical exaggeration: 90X. The anticlinal deformation with a WNW-SES trending axis is discussed by *Melnick et al*. [2009]. (c) Coseismic uplift due to the 1960 Valdivia earthquake (green line, *Moreno et al*. [2009]), and the coseismic plus postseismic uplift of the 2010 Maule earthquake (blue line, this study) projected along profile *a*–*a*′, and the total uplift (red line). Squares are the projected in situ measurements with the same color codes as Figure 12a. Dashed black line indicates the location of the neutral line. (d) The equivalent uplift rate (red line), derived by dividing the total uplift in Figure 12c by the period between 2010 and 1835, assuming the year of 1835 is the onset of another seismic cycle. Black squares are the projected GPS vertical velocities. (e) Projected topography along the swath *b*–*b*′, showing clear back-tilting of the peninsula. Vertical exaggeration: 25X. (f) Uplift curves along the *b*–*b*′ profile, with the same color codes as Figure 12c. (g) The equivalent uplift rate and GPS vertical velocities projected along profile *b*–*b*′.

values corresponding to velocity strengthening and negative values to velocity weakening. The smaller estimated $(a-b)\sigma_n$ value for the offshore Arauco Peninsula and the intermediate value for the northern afterslip patch near San Antonio may result from smaller $a-b$ values than surrounding regions, suggesting strong variations in effective megathrust fault properties in the Arauco and San Antonio intersegment areas. Alternatively, locally high pore pressure and therefore small effective normal stress may play an important role in changing the slip behavior in this region. However, Cubas et al. (in preparation, 2013) use the critical taper theory to infer a values of 0.375–0.6 for the Hubbert-Rubey parameter in these two areas (the ratio of pore pressure versus the lithostatic pressure, with 0.4 for hydrostatic; *Hubbert and Rubey* [1959]), suggesting that the pore pressures is not extraordinarily high in this region. Therefore, it is likely that local frictional heterogeneity (smaller positive $a-b$ values) is responsible for the postseismic creep in the intersegment areas. Numerical modeling of rate-and-state frictional sliding on a shear-loaded planar fault also suggests that when $a-b$ is smaller, postseismic sliding propagates far from the coseismic slip region over short time intervals [*Kato*, 2007].

[32] Compared to intermediate $(a-b)\sigma_n$ values in the San Antonio intersegment area, the nearly neutral inferred value near Arauco might help explain some specific aspects of this area. It has been suggested, based on dynamic modeling of slip on a fault with heterogeneous rate-and-state friction patches, that the barrier effect of a rate-strengthening patch scales with the product of $(a-b)\sigma_n$ and the size of the patch [*Kaneko et al.*, 2010]. It might be argued that because of a relatively small value of $(a-b)\sigma_n$ in the Arauco Peninsula area (0.01–0.22 MPa), dynamic ruptures can propagate into the area but do not rupture through it because of its relatively large size. This effect might explain why we observed both some coseismic slip and aseismic afterslip beneath the Arauco Peninsula area. This inference would also be consistent with seismic slip of ~5 m beneath the Arauco Peninsula during the 1960 Valdivia earthquake [*Moreno et al.*, 2009], although the spatial resolution of the models is very low due to the limited availability of relevant observations. The Arauco Peninsula area would owe its character as a barrier to the size of the modestly rate-strengthening zone. The along-trench length of the Arauco Peninsula barrier is ~100 km, much longer than the Batu Islands barrier in Sumatra [*Chlieh et al.*, 2008] and the Mejillones Peninsula barrier in northern Chile [*Pritchard and Simons*, 2006; *Béjar-Pizarro et al.*, 2010; *Victor et al.*, 2011], which may also be examples of rate-strengthening barriers on subduction megathrusts. The findings from the Arauco Peninsula barrier are consistent with the idea that both the $(a-b)\sigma_n$ value and the barrier size determine the barrier effect of a velocity strengthening patch [*Kaneko et al.*, 2010].

6.3. Arauco Peninsula Uplift

[33] We now consider the timing of the deformation of the peninsula in the context of the seismic cycle. If we assume that the whole medium is purely elastic, all elastic strain that accumulates during the interseismic period should be released in earthquakes. In this case, there is no permanent strain and no formation of the peninsula. Clearly, inelastic deformation must have occurred or be occurring to account for the uplift of the Arauco Peninsula. *Melnick et al.* [2009] suggested that there are two styles of long-term deformation on the peninsula: anticlinal bending (Figure 12b), with the anticline axis going through the center of the peninsula in a WNW-ESE orientation, and back tilting, with the marine terraces tilting toward the east (Figure 12e). We now compare these deformation styles to the geodetic data and modeled results we obtained during the past two decades. Because of the lack of in situ measurements within the swath along the profile *a*–*a*′, we use only the modeled uplift to derive the total uplift between 1835 and 2010 (Figure 12c). Using the elapsed time of 175 years, the equivalent interseismic uplift rate is nearly equivalent to the measured subsidence rate (Figure 12d). The nearly neutral balance seems to indicate that all the elastic strain has been released during the two large earthquakes and no permanent strain has accumulated within the last seismic cycle. However, based on the estimates from *Melnick et al.* [2009], the long-term uplift rate ranges from 1.8 mm/yr near the anticline axis to 0.3 mm/yr near the bottom of the anticline flank. The difference is so small (1.5 mm/yr) that it resides within the errors of model predictions and the GPS observations. In this case, we probably would not be able to isolate coseismic or interseismic nonelastic deformation of the anticline on the Arauco Peninsula.

[34] Along profile *b*–*b*′, the uplift pattern from model predictions agrees in general with field observations (Figure 12f), and the cumulative coseismic deformation since 1835 mimics the back-tilting of the peninsula. The equivalent uplift rate during the past 175 years is slightly larger than the interseismic subsidence as we get close to the trench, resulting in backtilt-like deformation (Figure 12g). A straightforward interpretation is that the backtilting of the peninsula may form during the coseismic and early postseismic periods, although it is not clear whether the anticlinal folding should also happen at the same time. This permanent nonelastic deformation could be either associated with the elastic cycle on the megathrust, or resulting from the slip on crustal splay faults in the frontal accretionary prism (Figure 1b) [*Contreras-Reyes et al.*, 2010; *Melnick et al.*, 2012]. As the chance of rupture propagation into this area increases due to low inferred $(a-b)\sigma_n$ values, so does the triggered slip on the crustal slay faults, and the accumulation of nonelastic deformation. This idea of coseismic and postseismic uplift of the Arauco Peninsula is different from the observations around the Mejillones Peninsula in northern Chile [*Ortlieb et al.*, 1996; *Pritchard and Simons*, 2006; *Loveless et al.*, 2010] and the Paracas Peninsula in Peru [*Sladen et al.*, 2010], whose patterns of coseismic vertical movement are different from that of the long-term deformation. The behavior of these peninsulas is considered to be dominated by postseismic and interseismic uplift [*Sladen et al.*, 2010; *Victor et al.*, 2011]. An alternative interpretation is that the backtilting of the Arauco Peninsula results from a deficit of interseismic subsidence, which in turn is the net effect of elastic subsidence and nonelastic uplift in the interseismic period. The coeval strain accumulation of opposite signs is a more complicated interpretation, and therefore field evidence is needed to support this view.

6.4. Limitations

[35] We summarize here all the discrepancies between observations and predictions, together with the anomalies in our model. First, our favored coseismic slip model fails to predict the short-wavelength signals in the GPS vertical

component (Figure 6), which can be fit only when allowing deep slip patches beneath the Andes [*Vigny et al.*, 2011]. Second, there is a systematic misfit in postseismic horizontal displacements for GPS stations around the Andes (Figure 8). These stations demonstrate different deformation behaviors from the three major afterslip patches (Figure 11). These results suggest that the middle- to far-field sampling of the deformation field associated with the Maule earthquake will require more realistic models than elastic or layered elastic half-space.

[36] The above-mentioned discrepancies and model anomalies can be potentially explained by one or more of the following: (1) over-simplification of the elastic model, (2) elastic deformation along other uppercrustal structures, and (3) deformation due to other mechanisms, such as viscoelastic deformation. We address these issues separately below.

[37] As demonstrated earlier, adopting a homogeneous elastic half-space or a 1-D layered elastic half-space can modulate the inferred patterns of fault slip (Figure S8). *Hsu et al.* [2011] have pointed out the important role played by 3-D elastic structure in fault slip inversions. Based on heat flow observations and numerical models, *Volker et al.* [2011] estimated that the geothermal gradient varies greatly over a distance of 400 km, from 10°C/km near the coast, to 5.5°C/km near the Central Valley, and to 22.5°C/km below the Andes. Given the temperature and compositional dependence of elastic moduli, we may expect considerable 3-D variations in elastic structure. Future models of this region using 3-D elastic Green's functions may help us understand the discrepancies—although our relatively poor a priori understanding of 3-D elastic structure may make such an effort pointless.

[38] We are also concerned with the potential role played by upper-crustal structure(s) during and after the earthquake. This explanation for the misfits proximal to the Andes may be as viable as that of variations in 3-D elastic structure, although elastic deformation associated with the earthquake cycle at the plate boundary will not result in the permanent deformation that built the Andes. Slip on a shallow crustal fault, or a downdip extension of such a fault, will create permanent surface deformation of a smaller spatial wavelength similar to the depth of the dislocation tip, a pattern that we see in the coseismic vertical displacement field. Given the locations of the GPS stations with large misfits across the Andes (Figure 8), the Neogene Deformation Front, the west-vergent thrust faults that bounds the west flank of the Andes (between 32° and 38°S, Figures 1b and 1c) and their associated décollement may be potential candidates for such an aseismically slipping upper crustal structure (Figure 1c) [*Armijo et al.*, 2010]. The Quaternary deformation pattern along this fault system has long been a subject of debate. There appears to be little indication of Quaternary contraction except along a small section of Southern Central Andes (36°–38°S) [*Folguera and Ramos*, 2009]. *Folguera et al.* [2007, 2008] even argue that an extensional state of stress in the Andean Cordillera and foothills is producing a regional collapse. On the other hand, *Cobbold and Rossello* [2003], *Galland et al.* [2007], *Guzmán et al.* [2007], and *Messager et al.* [2010] postulate that the stress regime remains mainly compressive. If this shallow crustal fault hypothesis holds, its associated surface deformation will still be intertwined with deformation from the interaction on the plate boundary, making it nontrivial to separate the relative contribution from each structure. A denser and more optimally designed GPS network may be needed to specifically target these upper plate structures. We recognize that considerably more study is needed to characterize the role, if any, of hypothesized upper crustal structures, how they are driven by the plate boundary, and how they contribute to the nonelastic deformation that creates the Andes.

[39] It is also possible that viscoelastic deformation may account for a non-negligible part of the observed postseismic deformation [e.g., *Pollitz et al.*, 1998, 2006]. Nevertheless, because viscoelastic deformation is triggered by coseismic stress change and acts mainly during the postseismic period, this process alone will not reconcile the discrepancies between the observed short-wavelength and modeled long-wavelength coseismic vertical deformation. It is likely that the combination of two or more of the aforementioned processes is necessary to explain all the coseismic and postseismic data for the Maule earthquake.

[40] These discrepancies between our models and the data have significant implications. The Maule earthquake produced measureable deformation in the overriding plate out to a distance of over 1000 km. The standard coseismic and postseismic modeling of such events using layered elastic half-space produces results that explain observations in western Chile well. Our models are less successful in explaining observations in central and eastern Chile and all of Argentina. Such observations, which are not available when the overriding plate consists of a relatively narrow island chain (such as Sumatra and Japan), will potentially provide the data needed to differentiate between competing models for postseismic behavior.

7. Conclusions

[41] To summarize, our joint inversion model shows a coseismic slip pattern similar to the previous ones derived from joint inversion of seismic, geodetic and tsunami data [*Delouis et al.*, 2010; *Lorito et al.*, 2011]. The shallowest 15–20 km of the megathrust shows neither significant coseismic slip nor resolvable postseismic slip, suggesting that the slip on this portion of the megathrust is dominantly due to interseismic creep (between 1835 and 2010). Slip on the megathrust at depth between 15–20 and 50 km is probably mostly seismic. An exception is near the Arauco Peninsula, where aseismic afterslip extends to as shallow as 10 km near trench. We derive a nearly neutral $a-b$ value for this shallow afterslip patch, consistent with the inferred propagation of seismic rupture into this region, whereas the large width of this segment boundary would be the main reason for its barrier effect. This conditionally stable characteristic may also be related to the coseismic uplift of the Arauco Peninsula, as seismic ruptures may propagate more easily into this barrier and trigger the slip on upper-crust structures. Postseismic energy release follows a general trend in which the amount of postseismic slip scales with the coseismic moment release. Our result also shows marked data misfit near the Andes, indicating that other geophysical processes may be involved in the postseismic deformation over the region.

[42] **Acknowledgments.** We thank Matthew Pritchard, the other reviewer and the associate editor of *JGR-Solid Earth*, for valuable comments and suggestions. We thank Shengji Wei at Caltech for providing the

coseismic deformation model for the Pichilemu aftershock. We also thank Nadaya Cubas for her valuable discussions and help in interpreting the frictional properties. ALOS data is copyright Japanese Aerospace Exploration Agency and METI and provided through the U.S. Government Research Consortium Data Pool at the Alaska Satellite Facility and through the Group on Earth Observation Geohazards Supersite. This research is cofunded by NSF grant EAR-1118239, the Gordon and Betty Moore Foundation through Grant GBMF #423.01 to the Caltech Tectonics Observatory, and the NASA Earth Surface and Interior focus area and carried out at the Jet Propulsion Laboratory, California Institute of Technology, under a contract with the National Aeronautics and Space Administration. Part of the cGPS data used for this study have been acquired under the Chilean-French international collaboration "LIA Montessus de ballore," supported by CONICYT and CNRS; and ANR project SUBCHILE (grant #ANR-05-CATT-014). This paper is Caltech Tectonic Observatory contribution 211 and Seismolab contribution 10088.

References

Agurto, H., A. Rietbrock, I. Ryder, and M. Miller (2012), Seismic-afterslip characterization of the 2010 MW 8.8 Maule, Chile, earthquake based on moment tensor inversion, *Geophys. Res. Lett.*, *39*, L20303, doi:10.1029/2012GL053434.

Armijo, R., R. Rauld, R. Thiele, G. Vargas, J. Campos, R. Lacassin, and E. Kausel (2010), The West Andean Thrust, the San Ramon Fault, and the seismic hazard for Santiago, Chile, *Tectonics*, *29*, TC2007, doi:10.1029/2008TC002427.

Astroza, M., F. Cabezas, M. O. Moroni, L. Massone, S. Ruiz, E. Parra, F. Cordero, and A. Mottadelli (2010), Intensidades sismicas en el area de danõs del terremoto del 27 de Febrero de 2010, Departamento de Ingeniería Civil, Facultad de Ciencias Físicas y Matemáticas, Universidad de Chile.

Baba, T., K. Hirata, T. Hori, and H. Sakaguchi (2006), Offshore geodetic data conducive to the estimation of the afterslip distribution following the 2003 Tokachi-oki earthquake, *Earth Planet. Sci. Lett.*, *241*, 281–292, doi:10.1016/j.epsl.2005.10.019.

Barrientos, S. E., and S. N. Ward (1990), The 1960 Chile earthquake: inversion for slip distribution from surface deformation, *Geophys. J. Int.*, *103*(3), 589–598.

Beck, S., S. Barrientos, E. Kausel, and M. Reyes (1998), Source characteristics of historic earthquakes along the central Chile subduction zone, *J. S. Am. Earth Sci.*, *11*(2), 115–129.

Béjar-Pizarro, M., et al. (2010), Asperities and barriers on the seismogenic zone in North Chile: state-of-the-art after the 2007 Mw 7.7 Tocopilla earthquake inferred by GPS and InSAR data, *Geophys. J. Int.*, *183*(1), 390–406, doi:10.1111/j.1365-246X.2010.04748.x.

Burgmann, R., M. G. Kogan, V. E. Levin, C. H. Scholz, R. W. King, and G. M. Steblov (2001), Rapid aseismic moment release following the 5 December, 1997 Kronotsky, Kamchatka, earthquake, *Geophys. Res. Lett.*, *28*(7), 1331–1334, doi:10.1029/2000gl012350.

Cahill, T., and B. L. Isacks (1992), Seismicity and Shape of the Subducted Nazca Plate, *J. Geophys. Res.*, *97*(B12), 17503–17529, doi:10.1029/92jb00493.

Campos, J., D. Hatzfeld, R. Madariaga, G. Lopez, E. Kausel, A. Zollo, G. Iannacone, R. Fromm, S. Barrientos, and H. Lyon-Caen (2002), A seismological study of the 1835 seismic gap in south-central Chile, *Phys. Earth Planet. In.*, *132*(1–3), 177–195, doi:10.1016/S0031-9201(02)00051-1.

Chlieh, M., J. B. De Chabalier, J. C. Ruegg, R. Armijo, R. Dmowska, J. Campos, and K. L. Feigl (2004), Crustal deformation and fault slip during the seismic cycle in the North Chile subduction zone, from GPS and InSAR observations, *Geophys. J. Int.*, *158*(2), 695–711, doi:10.1111/j.1365-246X.2004.02326.x.

Chlieh, M., et al. (2007), Coseismic slip and afterslip of the great M(w) 9.15 Sumatra-Andaman earthquake of 2004, *B. Seismol. Soc. Am.*, *97*(1), S152–S173, doi:10.1785/0120050631.

Chlieh, M., J. P. Avouac, K. Sieh, D. H. Natawidjaja, and J. Galetzka (2008), Heterogeneous coupling of the Sumatran megathrust constrained by geodetic and paleogeodetic measurements, *J. Geophys. Res.*, *113*(B5), B05305, doi:10.1029/2007jb004981.

Cifuentes, I. L. (1989), The 1960 Chilean Earthquakes, *J. Geophys. Res.*, *94*(B1), 665–680.

Cisternas, M., et al. (2005), Predecessors of the giant 1960 Chile earthquake, *Nature*, *437*(7057), 404–407, doi:10.1038/nature03943.

Cobbold, P. R., and E. A. Rossello (2003), Aptian to recent compressional deformation, foothills of the Neuquen Basin, Argentina, *Mar. Pet. Geol.*, *20*(5), 429–443, doi:10.1016/S0264-8172(03)00077-1.

Contreras-Reyes, E., E. R. Flueh, and I. Grevemeyer (2010), Tectonic control on sediment accretion and subduction off south central Chile: Implications for coseismic rupture processes of the 1960 and 2010 megathrust earthquakes, *Tectonics*, *29*, TC6018, doi:10.1029/2010TC002734.

Darwin, C. (1851), *Geological Observations on Coral Reefs, Volcanic Islands, and on South America -- Being the Geology of the Voyage of the Beagle, Under the Command of Captain Fitzroy, R.N., During the Years 1832 to 1836*, p. 768, Smith, Elder, and Co., London, U.K.

Delouis, B., J.-M. Nocquet, and M. Vallee (2010), Slip distribution of the February 27, 2010 Mw = 8.8 Maule Earthquake, central Chile, from static and high-rate GPS, InSAR, and broadband teleseismic data, *Geophys. Res. Lett.*, *37*, L17305, doi:10.1029/2010GL043899.

Divins, D. L. (2003), *Total Sediment Thickness of the Rorld's Oceans and Marginal Seas*, edited by N. N. G. D. Center, Boulder, Colo.

Farias, M., G. Vargas, A. Tassara, S. Carretier, S. Baize, D. Melnick, and K. Bataille (2010), Land-level changes produced by the Mw 8.8 2010 Chilean earthquake, *Science*, *329*(5994), 916, doi:10.1126/science.1192094.

Folguera, A., and V. A. Ramos (2009), Collision of the Mocha fracture zone and a < 4 Ma old wave of orogenic uplift in the Andes (36°-38°S), *Lithosphere*, *1*(6), 364–369, doi:10.1130/L66.1.

Folguera, A., V. A. Ramos, R. L. Hermanns, and J. Naranjo (2004), Neotectonics in the foothills of the southernmost central Andes (37°-38°S): Evidence of strike-slip displacement along the Antinir-Copahue fault zone, *Tectonics*, *23*(5), TC5008, doi:10.1029/2003TC001533.

Folguera, A., A. Introcaso, M. Giménez, F. Ruiz, P. Martinez, C. Tunstall, E. García Morabito, and V. A. Ramos (2007), Crustal attenuation in the Southern Andean retroarc (38°-39°30′S) determined from tectonic and gravimetric studies: The Lonco-Luán asthenospheric anomaly, *Tectonophysics*, *439*, 129–147, doi:10.1016/j.tecto.2007.04.001.

Folguera, A., G. Bottesi, T. Zapata, and V. A. Ramos (2008), Crustal collapse in the Andean backarc since 2 Ma: Tromen volcanic plateau, Southern Central Andes (36°40′-37°30′), *Tectonophysics*, *459*, 140–160, doi:10.1016/j.tecto.2007.12.013.

Fritz, H., et al. (2011), Field survey of the 27 February 2010 Chile tsunami, *Pure Appl. Geophys.*, *168*(11), 1989–2010, doi:10.1007/s00024-011-0283-5.

Galland, O., E. Hallot, P. R. Cobbold, G. Ruffet, and J. de Bremond d'Ars (2007), Volcanism in a compressional Andean setting: A structural and geochronological study of Tromen volcano (Neuquén province, Argentina), *Tectonics*, *26*, TC4010, doi: 10.1029/2006TC002011.

Geospatial Information Authority of Japan (2012), Postseismic slip distribution model inferred from GEONET data, edited, Japan

Gordeev, E. I., A. A. Gusev, V. E. Levin, V. F. Bakhtiarov, V. M. Pavlov, V. N. Chebrov, and M. Kasahara (2001), Preliminary analysis of deformation at the Eurasia-Pacific-North America plate junction from GPS data, *Geophys. J. Int.*, *147*(1), 189–198, doi:10.1046/j.0956-540x.2001.01515.x.

Guzmán, C., E. Cristallini, and G. Bottesi (2007), Contemporary stress orientations in the Andean retroarc between 34°S and 39°S from borehole breakout analysis, *Tectonics*, *26*, TC3016, doi:10.1029/2006TC001958.

Haberland, C., A. Rietbrock, D. Lange, K. Bataille, and T. Dahm (2009), Structure of the seismogenic zone of the southcentral Chilean margin revealed by local earthquake traveltime tomography, *J. Geophys. Res.*, *114*, B01317, doi:10.1029/2008JB005802.

Hashimoto, M., N. Choosakul, M. Hashizume, S. Takemoto, H. Takiguchi, Y. Fukuda, and K. Frjimori (2006), Crustal deformations associated with the great Sumatra-Andaman earthquake deduced from continuous GPS observation, *Earth Planets Space*, *58*(2), 127–139.

Hébert, H., P. Heinrich, S. François, and A. Piatanesi (2001), Far-field simulation of tsunami propagation in the Pacific Ocean: impact on the Marquesas Islands (French Polynesia), *J. Geophys. Res.*, *106*(C5), 9161–9177, doi:10.1029/2000JC000552.

Heinrich, P., F. Schindele, S. Guibourg, and F. P. Ihmlé (1998), Modeling of the February 1996 Peruvian tsunami, *Geophys. Res. Lett.*, *25*(14), 2687–2690.

Heki, K., and Y. Tamura (1997), Short term afterslip in the 1994 Sanriku-Haruka-Oki earthquake, *Geophys. Res. Lett.*, *24*(24), 3285–3288, doi:10.1029/97gl03316.

Heki, K., S. Miyazaki, and H. Tsuji (1997), Silent fault slip following an interplate thrust earthquake at the Japan Trench, *Nature*, *386*(6625), 595–598, doi:10.1038/386595a0.

Hsu, Y.-J., M. Simons, J.-P. Avouac, J. Galetzka, K. Sieh, M. Chlieh, D. Natawidjaja, L. Prawirodirdjo, and Y. Bock (2006), Frictional afterslip following the 2005 Nias-Simeulue earthquake, Sumatra, *Science*, *312*(5782), 1921–1926, doi:10.1126/science.1126960.

Hsu, Y.-J., M. Simons, C. Williams, and E. Casarotti (2011), Three-dimensional FEM derived elastic Green's functions for the coseismic deformation of the 2005 Mw 8.7 Nias-Simeulue, Sumatra earthquake, *Geochem. Geophys. Geosyst.*, *12*, Q07013, doi:10.1029/2011GC003553.

Hubbert, M. K., and W. W. Rubey (1959), Role of fluid pressure in mechanics of overthrust faulting. I. Mechanics of fluid-filled porous solids and its application to overthrust faulting, *Geol. Soc. Am. Bull.*, *70*(2), 115–166.

von Huene, R., and D. W. Scholl (1991), Observations at convergent margins concerning sediment subduction, subduction erosion, and the growth of continental crust, *Rev. Geophys.*, *29*(3), 279–316.

Hutton, W., C. DeMets, O. Sanchez, G. Suarez, and J. Stock (2001), Slip kinematics and dynamics during and after the 1995 October 9 M-w = 8.0 Colima-Jalisco earthquake, Mexico, from GPS geodetic constraints, *Geophys. J. Int.*, *146*(3), 637–658, doi:10.1046/j.1365-246X.2001.00472.x.

Ito, Y., K. Obara, K. Shiomi, S. Sekine, and H. Hirose (2007), Slow earthquakes coincident with episodic tremors and slow slip events, *Science*, *315*(5811), 503–506, doi:10.1126/science.1134454.

Ji, C., D. J. Wald, and D. V. Helmberger (2002), Source description of the 1999 Hector Mine, California, earthquake, part I: Wavelet domain inversion theory and resolution analysis, *B. Seismol. Soc. Am.*, *92*(4), 1192–1207, doi:10.1785/0120000916.

Kaneko, Y., J.-P. Avouac, and N. Lapusta (2010), Towards inferring earthquake patterns from geodetic observations of interseismic coupling, *Nat. Geosci.*, *3*(5), 363–369, doi:10.1038/NGEO843.

Kato, N. (2007), Expansion of aftershock areas caused by propagating post-seismic sliding, *Geophys. J. Int.*, *168*(2), 797–808, doi:10.1111/j.1365-246X.2006.03255.x.

Kawasaki, I., Y. Asai, Y. Tamura, T. Sagiya, N. Mikami, Y. Okada, M. Sakata, and M. Kasahara (1995), The 1992 Sanriku-oki, Japan, ultra-slow earthquake, *J. Phys. Earth*, *43*(2), 105–116.

Kawasaki, I., Y. Asai, and Y. Tamura (2001), Space-time distribution of interplate moment release including slow earthquakes and the seismo-geodetic coupling in the Sanriku-oki region along the Japan trench, *Tectonophysics*, *330*(3-4), 267–283, doi:10.1016/S0040-1951(00)00245-6.

Kendrick, E., M. Bevis, R. Smalley, B. Brooks, R. B. Vargas, E. Lauriia, and L. P. S. Fortes (2003), The Nazca South America Euler vector and its rate of change, *J. S. Am. Earth Sci.*, *16*(2), 125–131, doi:10.1016/S0895-9811(03)00028-2.

Konca, A. O., et al. (2008), Partial rupture of a locked patch of the Sumatra megathrust during the 2007 earthquake sequence, *Nature*, *456*(7222), 631–635, doi:10.1038/nature07572.

Kositsky, A., and J. P. Avouac (2010), Inverting geodetic time-series with a principal component analysis-based inversion method (PCAIM), *J. Geophys. Res.*, *115*, B03401, doi:10.1029/2009JB006535.

Lay, T., C. J. Ammon, H. Kanamori, K. D. Koper, O. Sufri, and A. R. Hutko (2010), Teleseismic inversion for rupture process of the 27 February 2010 Chile (M-w 8.8) earthquake, *Geophys. Res. Lett.*, *37*, L13301, doi:10.1029/2010GL043379.

Lin, Y.-n. N., A. P. Kositsky, and J.-P. Avouac (2010), PCAIM joint inversion of InSAR and ground-based geodetic time series: Application to monitoring magmatic inflation beneath the Long Valley Caldera, *Geophys. Res. Lett.*, *37*, L23301, doi:10.1029/2010GL045769.

Lomnitz, C. (2004), Major earthquakes of Chile: A historical survey, 1535-1960, *Seismol. Res. Lett.*, *75*(3), 368–378.

Lorito, S., F. Romano, S. Atzori, X. Tong, A. Avallone, J. McCloskey, M. Cocco, E. Boschi, and A. Piatanesi (2011), Limited overlap between the seismic gap and coseismic slip of the great 2010 Chile earthquake, *Nat. Geosci.*, *4*(3), 173–177, doi:10.1038/NGEO1073.

Loveless, J. P., M. E. Pritchard, and N. Kukowski (2010), Testing mechanisms of subduction zone segmentation and seismogenesis with slip distributions from recent Andean earthquakes, *Tectonophysics*, *495*(1–2), 15–33, doi:10.1016/j.tecto.2009.05.008.

Madariaga, R., M. Metois, C. Vigny, and J. Campos (2010), Central Chile finally breaks, *Science*, *328*(5975), 181–182, doi:10.1126/science.1189197.

Marone, C. (1998), Laboratory-derived frictional laws and their application to seismic faulting, *Annu. Rev. Earth Planet. Sci.*, *26*(1), 643–696, doi:10.1146/annurev.earth.26.1.643.

Melbourne, T. I., F. H. Webb, J. M. Stock, and C. Reigber (2002), Rapid postseismic transients in subduction zones from continuous GPS, *J. Geophys. Res.*, *107*(B10), 2241, doi:10.1029/2001JB000555.

Melnick, D., B. Bookhagen, M. R. Strecker, and H. P. Echtler (2009), Segmentation of megathrust rupture zones from fore-arc deformation patterns over hundreds to millions of years, Arauco peninsula, Chile, *J. Geophys. Res.*, *114*, B01407, doi:10.1029/2008JB005788.

Melnick, D., M. Moreno, M. Motagh, M. Cisternas, and R. L. Wesson (2012), Splay fault slip during the Mw 8.8 2010 Maule Chile earthquake, *Geology*, doi:10.1130/G32712.1.

Meng, L., A. Inbal, and J.-P. Ampuero (2011), A window into the complexity of the dynamic rupture of the 2011 Mw 9 Tohoku-Oki earthquake, *Geophys. Res. Lett.*, *38*, L00G07, doi:10.1029/2011GL048118.

Messager, G., B. Nivìire, J. Martinod, P. Lacan, and J. P. Xavier (2010), Geomorphic evidence for Plio-Quaternary compression in the Andean foothills of the southern Neuquén Basin, Argentina, *Tectonics*, *29*, TC4003, doi:10.1029/2009TC002609.

Métois, M., A. Socquet, and C. Vigny (2012), Interseismic coupling, segmentation and mechanical behavior of the central Chile subduction zone, *J. Geophys. Res.*, *117*, B03406, doi:10.1029/2011jb008736.

Miyazaki, S., P. Segall, J. Fukuda, and T. Kato (2004), Space time distribution of afterslip following the 2003 Tokachi-oki earthquake: Implications for variations in fault zone frictional properties, *Geophys. Res. Lett.*, *31*, L06623, doi:10.1029/2003GL019410.

Moreno, M. S., J. Klotz, D. Melnick, H. Echtler, and K. Bataille (2008), Active faulting and heterogeneous deformation across a megathrust segment boundary from GPS data, south central Chile (36-39°S), *Geochem. Geophys. Geosyst.*, *9*, Q12024, doi:10.1029/2008GC002198.

Moreno, M. S., J. Bolte, J. Klotz, and D. Melnick (2009), Impact of megathrust geometry on inversion of coseismic slip from geodetic data: Application to the 1960 Chile earthquake, *Geophys. Res. Lett.*, *36*, L16310, doi:10.1029/2009GL039276.

Moreno, M., M. Rosenau, and O. Oncken (2010), 2010 Maule earthquake slip correlates with pre-seismic locking of Andean subduction zone, *Nature*, *467*(7312), 198–202, doi:10.1038/nature09349.

Moreno, M., et al. (2012), Toward understanding tectonic control on the Mw 8.8 2010 Maule Chile earthquake, *Earth Planet. Sci. Lett.*, *321–322*, 152–165, doi:10.1016/j.epsl.2012.01.006.

Nishimura, T., et al. (2000), Distribution of seismic coupling on the subducting plate boundary in northeastern Japan inferred from GPS observations, *Tectonophysics*, *323*(3–4), 217–238, doi:10.1016/s0040-1951(00)00108-6.

Ortlieb, L., S. Barrientos, and N. Guzman (1996), Coseismic coastal uplift and coralline algae record in Northern Chile: The 1995 Antofagasta earthquake case, *Quat. Sci. Rev.*, *15*(8–9), 949–960, doi:10.1016/S0277-3791(96)00056-X.

Ozawa, S., M. Kaidzu, M. Murakami, T. Imakiire, and Y. Hatanaka (2004), Coseismic and postseismic crustal deformation after the Mw 8 Tokachi-oki earthquake in Japan, *Earth Planets Space*, *56*(7), 675–680.

Ozawa, S., T. Nishimura, H. Munekane, H. Suito, T. Kobayashi, M. Tobita, and T. Imakiire (2012), Preceding, coseismic, and postseismic slips of the 2011 Tohoku earthquake, Japan, *J. Geophys. Res.*, *117*, B07404, doi:10.1029/2011JB009120.

Perfettini, H., and J. P. Avouac (2004), Postseismic relaxation driven by brittle creep: A possible mechanism to reconcile geodetic measurements and the decay rate of aftershocks, application to the Chi-Chi earthquake, Taiwan, *J. Geophys. Res.*, *109*, B02304, doi:10.1029/2003JB002488.

Perfettini, H., et al. (2010), Seismic and aseismic slip on the Central Peru megathrust, *Nature*, *465*(7294), 78–81, doi:10.1038/nature09062.

Piatanesi, A., and S. Lorito (2007), Rupture process of the 2004 Sumatra-Andaman earthquake from tsunami waveform inversion, *B. Seismol. Soc. Am.*, *97*(1), S223–S231, doi:10.1785/0120050627.

Plafker, G., and J. C. Savage (1970), Mechanism of the Chilean Earthquakes of May 21 and 22, 1960, *Geol. Soc. Am. Bull.*, *81*(4), 1001–1030.

Plank, T., and C. H. Langmuir (1998), The chemical composition of subducting sediment and its consequences for the crust and mantle, *Chem. Geol.*, *145*(3–4), 325–394.

Pollitz, F. F., R. Burgmann, and P. Segall (1998), Joint estimation of afterslip rate and postseismic relaxation following the 1989 Loma Prieta earthquake, *J. Geophys. Res.*, *103*(B11), 26975–26992, doi:10.1029/98jb01554.

Pollitz, F. F., R. Bürgmann, and P. Banerjee (2006), Post-seismic relaxation following the great 2004 Sumatra-Andaman earthquake on a compressible self-gravitating Earth, *Geophys. J. Int.*, *167*(1), 397–420, doi:10.1111/j.1365-246X.2006.03018.x.

Pritchard, M. E., and M. Simons (2006), An aseismic slip pulse in northern Chile and along-strike variations in seismogenic behavior, *J. Geophys. Res.*, *111*(B8), B08405, doi:10.1029/2006JB004258.

Pritchard, M. E., E. O. Norabuena, C. Ji, R. Boroschek, D. Comte, M. Simons, T. H. Dixon, and P. A. Rosen (2007), Geodetic, teleseismic, and strong motion constraints on slip from recent southern Peru subduction zone earthquakes, *Journal of Geophysical Research: Solid Earth*, *112*, B03307, doi:10.1029/2006jb004294.

Rietbrock, A., C. Haberland, K. Bataille, T. Dahm, and O. Oncken (2005), Studying the seismogenic coupling zone with a passive seismic array, *Eos. Trans. AGU*, *86*, 293–300, doi:10.1029/2005EO320001.

Rietbrock, A., I. Ryder, G. Hayes, C. Haberland, D. Comte, S. Roecker, and H. Lyon-Caen (2012), Aftershock seismicity of the 2010 Maule Mw = 8.8, Chile, earthquake: Correlation between co-seismic slip models and aftershock distribution?, *Geophys. Res. Lett.*, *39*, L08310, doi:10.1029/2012GL051308.

Ruegg, J. C., M. Olcay, and D. Lazo (2001), Co-, post- and pre(?)-seismic displacements associated with the Mw 8.4 Southern Peru Earthquake of 23 June 2001 from continuous GPS measurements, *Seismol. Res. Lett.*, *72*(6), 673–678, doi:10.1785/gssrl.72.6.673.

Ruegg, J. C., J. Campos, R. Madariaga, E. Kausel, J. B. de Chabalier, R. Armijo, D. Dimitrov, I. Georgiev, and S. Barrientos (2002), Interseismic strain accumulation in south central Chile from GPS measurements, 1996-1999, *Geophys. Res. Lett.*, *29*(11), 1517, doi:10.1029/2001GL013438.

Ruegg, J. C., A. Rudloff, C. Vigny, R. Madariaga, J. B. de Chabalier, J. Campos, E. Kausel, S. Barrientos, and D. Dimitrov (2009), Interseismic strain accumulation measured by GPS in the seismic gap between Constitución and Concepción in Chile, *Phys. Earth Planet. Inter.*, *175*(1–2), 78–85, doi:10.1016/j.pepi.2008.02.015.

Ruff, L. J. (1989), Do trench sediments affect great earthquake occurrence in subduction zones?, *Pure Appl. Geophys.*, *129*(1–2), 263–282, doi:10.1007/bf00874629.

Satake, K. (1993), Depth distribution of coseismic slip along the Nankai Trough, Japan, from joint inversion of geodetic and tsunami data, *Journal of Geophysical Research: Solid Earth*, *98*(B3), 4553–4565, doi:10.1029/92jb01553.

Scherwath, M., E. Contreras-Reyes, E. R. Flueh, I. Grevemeyer, A. Krabbenhoeft, C. Papenberg, C. J. Petersen, and R. W. Weinrebe (2009), Deep lithospheric structures along the southern central Chile margin from wide-angle P-wave modelling, *Geophys. J. Int.*, *179*(1), 579–600, doi:10.1111/j.1365-246X.2009.04298.x.

Simons, M., et al. (2011), The 2011 magnitude 9.0 Tohoku-Oki earthquake: Mosaicking the megathrust from seconds to centuries, *Science*, *332*(6036), 1421–1425, doi:10.1126/science.1206731.

Sladen, A., and H. Hébert (2008), On the use of satellite altimetry to infer the earthquake rupture characteristics: application to the 2004 Sumatra event, *Geophys. J. Int.*, *172*(2), 707–714, doi:10.1111/j.1365-246X.2007.03669.x.

Sladen, A., H. Tavera, M. Simons, J. P. Avouac, A. O. Konca, H. Perfettini, L. Audin, E. J. Fielding, F. Ortega, and R. Cavagnoud (2010), Source model of the 2007 M-w 8.0 Pisco, Peru earthquake: Implications for seismogenic behavior of subduction megathrusts, *J. Geophys. Res.*, *115*, B02405, doi:10.1029/2009JB006429.

Song, T. R. A., and M. Simons (2003), Large trench-parallel gravity variations predict seismogenic behavior in subduction zones, *Science*, *301*(5633), 630–633, doi:10.1126/science.1085557.

Subarya, C., M. Chlieh, L. Prawirodirdjo, J. P. Avouac, Y. Bock, K. Sieh, A. J. Meltzner, D. H. Natawidjaja, and R. McCaffrey (2006), Plate-boundary deformation associated with the great Sumatra-Andaman earthquake, *Nature*, *440*(7080), 46–51, doi:10.1038/nature04522.

Suito, H., T. Nishimura, M. Tobita, T. Imakiire, and S. Ozawa (2011), Interplate fault slip along the Japan Trench before the occurrence of the 2011 off the Pacific coast of Tohoku Earthquake as inferred from GPS data, *Earth Planets Space*, *63*(7), 615–619, doi:10.5047/eps.2011.06.053.

Tong, X., et al. (2010), The 2010 Maule, Chile earthquake: Downdip rupture limit revealed by space geodesy, *Geophys. Res. Lett.*, *37*, L24311, doi:10.1029/2010GL045805.

Vargas, G., M. Farias, S. Carretier, A. Tassara, S. Baize, and D. Melnick (2011), Coastal uplift and tsunami effects associated to the 2010 M(w) 8.8 Maule earthquake in Central Chile, *Andean Geology*, *38*(1), 219–238.

Victor, P., M. Sobiesiak, J. Glodny, S. N. Nielsen, and O. Oncken (2011), Long-term persistence of subduction earthquake segment boundaries: Evidence from Mejillones Peninsula, northern Chile, *J. Geophys. Res.*, *116*, B02402, doi:10.1029/2010JB007771.

Vigny, C., et al. (2011), The 2010 Mw 8.8 Maule megathrust earthquake of central Chile, monitored by GPS, *Science*, *332*(6036), 1417–1421, doi:10.1126/science.1204132.

Volker, D., I. Grevemeyer, M. Stipp, K. Wang, and J. He (2011), Thermal control of the seismogenic zone of southern central Chile, *J. Geophys. Res.*, *116*, B10305, doi:10.1029/2011JB008247.

Wells, R. E., R. J. Blakely, Y. Sugiyama, D. W. Scholl, and P. A. Dinterman (2003), Basin-centered asperities in great subduction zone earthquakes: A link between slip, subsidence, and subduction erosion?, *J. Geophys. Res.*, *108*(B10), 2507, doi:10.1029/2002JB002072.

Yagi, Y., M. Kikuchi, and T. Nishimura (2003), Co-seismic slip, post-seismic slip, and largest aftershock associated with the 1994 Sanriku-haruka-oki, Japan, earthquake, *Geophys. Res. Lett.*, *30*(22), 2177, doi:10.1029/2003gl018189.

Coseismic and Postseismic Slip Associated with the 2010 Maule Earthquake, Chile: Characterizing the Arauco Peninsula Barrier Effect

Supplementary Online Materials

Yu-nung Nina Lin, Anthony Sladen, Francisco Ortega-Culaciati, Mark Simons,
Jean-Philippe Avouac, Eric J. Fielding, Benjamin A. Brooks, Michael Bevis, Jeff Genrich,
Andreas Rietbrock, Christophe Vigny, Robert Smalley and Anne Socquet

1. Data Selection and Processing

1.1 GPS Observations

Our general field, processing, and velocity analysis methods in South America have been described previously [Bevis et al., 1997; Brooks et al., 2003; Brooks et al., 2011; Kendrick et al., 2003]. We estimate velocities by stacking daily network solutions obtained using GAMIT [King and Bock, 2000] and GLOBK [Herring, 2000] software. All publicly available cGPS data in South America from 1 Jan 2007 through 10 June 2011 were processed using GAMIT with additional IGS sites included to provide reference frame stability. All data were processed using MIT precise orbits. Orbits were held tightly constrained and standard EOP and earth and ocean tides were applied. Due to the number of stations, two separate subnets were formed with common fiducial sites. The subnets were merged and combined with MIT's global solution using GLOBK. We express our solutions in a reference frame nominally attached to the stable South American craton that has horizontal RMS velocity of 0.92 mm/yr and vertical RMS velocity of 1.6mm/yr. We estimate positions and velocities in inner coordinates, treating the reference frame as a computational convenience and allowing it to rotate and translate freely (at constant rates) while focusing on the rate of change of the polyhedron’s shape and size. One six parameter Helmert transformation is applied to each daily polyhedron solution so as to align the daily polyhedra as closely as possible to a suite of constant velocity trajectories. No position or velocity constraints are imposed during this iterative stacking process: the only constraint is that the individual (daily) polyhedra are not allowed to change their size or shape.

We combined GPS data from multiple networks (**Table S1**), resulting in a total of 127 3-component continuous records. To determine coseismic offsets, we use all stations that cover the time span around the mainshock, resulting in a total of 79 stations each with 3 components. This data set includes an augmentation of 27 stations (**Table S2**) to the existing dataset of 61 cGPS and 33 campaign-mode GPS stations from Vigny et al. [2011]. Compared to the GPS network used in Moreno et al. [2012], our dataset contains 21 more stations to the north near Valparaíso and Santiago, but has relatively sparse spatial coverage to the south near the Arauco region, and therefore our model results in this area depend heavily on InSAR observations.

For the postseismic GPS time series, we selected stations between 32°S and 40°S with at least 180 epochs recorded between the mainshock on February 27 2010 and June 30 2011. We omitted GPS sites south of 39.5°S which may still contain signatures of prolonged regional postseismic relaxation following the 1960 Valdivia earthquake [Hu et al., 2004; Moreno et al., 2008]. These criteria resulted in 66 stations, with 30 of them installed after the 2010 earthquake.

For each time series we use a conventional least squares approach to separate postseismic deformation from other signals, including secular rates, coseismic jumps (e.g., the Maule main shock, Pichilemu aftershock as well as other events) and seasonal variations (**Fig. 2**). The RMS of the residuals is 3-5 mm in the horizontal and 10-15 mm in the vertical. Of the 127 GPS stations, 81 stations have at least one and half year of observations before the Maule earthquake. We use the secular rates from these 81 stations plus those from two published studies (**Fig. 2A**)[Moreno et al., 2008; Ruegg et al., 2009] to interpolate and correct for the 66 stations we use in our model (**Table S1**). This correction is done for horizontal components only, because the uncertainties for the vertical components are larger than the secular rates in many stations (**Fig. 2B**) [Ruegg et al., 2009]. To avoid introducing errors into our model through improper corrections, we choose to use only the vertical component of the time series that have at least 1.5 years of pre-quake records with more than 365 epochs to allow estimates of their vertical secular rates (**Fig. S1**). We did not interpolate the seasonal variations for the short time series, as these values tend to vary more rapidly in space due to the specific geological and hydrological setting of each station. We estimate seasonal variations based on the longest available records for each time series, and therefore the error for shorter time series is larger and the correction is less reliable. As a sanity check, we ensure that each of the corrected time series shows signals of similar order of magnitudes with other surrounding stations. In the end, 66 cGPS stations are used in the postseismic model and among them 22 vertical records were considered reliable.

The March 11 Mw=6.9 Pichilemu earthquake in 2010 and the January 2 Mw=7.1 Araucania earthquake in 2011 produced notable displacements in a few of the time series. These coseismic jumps and corresponding postseismic deformation, if significant, are also removed from the postseismic time series.

1.2 InSAR

The coseismic signal has sufficiently large amplitude (up to 3-4 m in the line of sight direction, **Fig. 4**) that we did not attempt to correct for any atmospheric delays. However, given the small amplitude and long wavelength of the postseismic deformation, it is challenging to image the tectonic signal with InSAR. We correct for the topographically-correlated phase delay by using a multi-scale approach [Lin et al., 2010a]. Given that the postseismic ascending SAR images were acquired much later than the descending track 422 (**Fig. 3**), resulting in a smaller signal-to-noise ratio (as postseismic deformation rates generally decay approximately exponentially with time), and that each track covers a different temporal period and cannot form a continuous snapshot image, we choose to arbitrarily down weight these tracks 10 to 100 times more than the descending tracks. We adjust the weighting of the wide-swath descending track based on the relative number of resampled InSAR observations and total GPS acquisition epochs so that both datasets contribute equally to the model, i.e. each dataset contributes equally to the reduced

Chi-square of the residuals.

We also correct for the deformation associated with the March 11, 2010 Pichilemu earthquake. This composite earthquake is presumably triggered by the stress transfer due to the slip on the subduction interface and is therefore considered as the aftershock of the Maule earthquake [Ryder et al., 2012]. We run a simple 1-plane finite fault model by using the source parameters from GCMT (strike = 144°, dip = 55°, rake = -90°, depth = 12.9 km, Mw = 6.9). Only InSAR data track 114 and teleseismic data are used in this model, since the main purpose is to remove the deformation associated with the Pichilemu events from the interferogram. The corrected track 114 is then used in our postseismic slip model.

In order to reduce the computational cost associated with inverting all the InSAR data, we adopt the spatially variable data resampling/averaging approach based on the estimate of the inherent data resolution for a given source model [Lohman and Simons, 2005]. This approach efficiently reduces the total number of data to ~3000 points for the combination of all 32 tracks to be used in the inversion, while preserving the information contained in the original interferograms at all relevant scales.

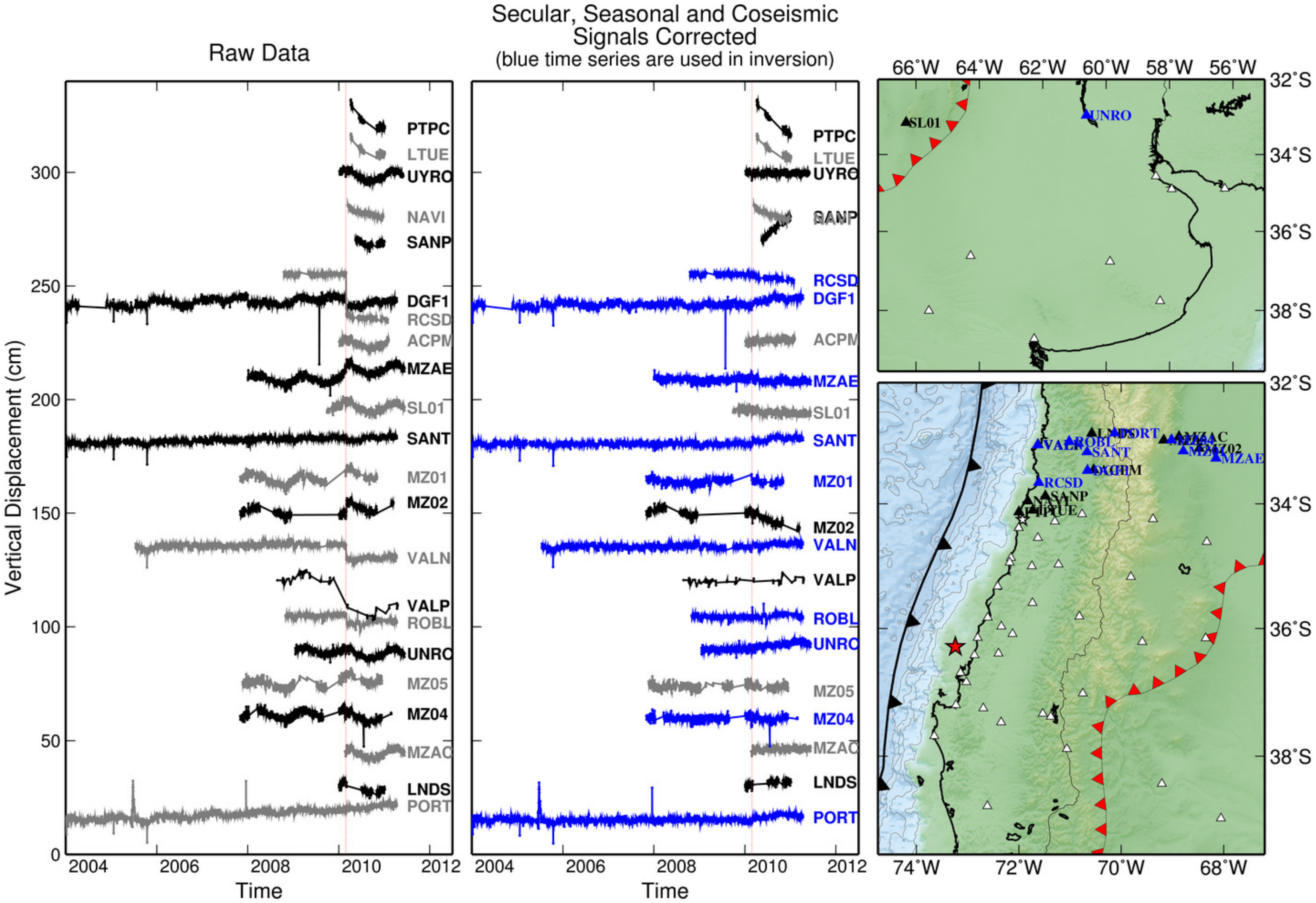

Figure S1-1

The vertical components of the cGPS time series. [Left] Raw time series. [Middle] The secular rates are estimated only with the long time series (with more than 1.5 years of records before the Maule earthquake). The seasonal variations are estimated with every time series. The coseismic jump is estimated whenever the time series span through the earthquake. [Right] The location of the stations. Blue stations are the ones picked for the postseismic slip inversion.

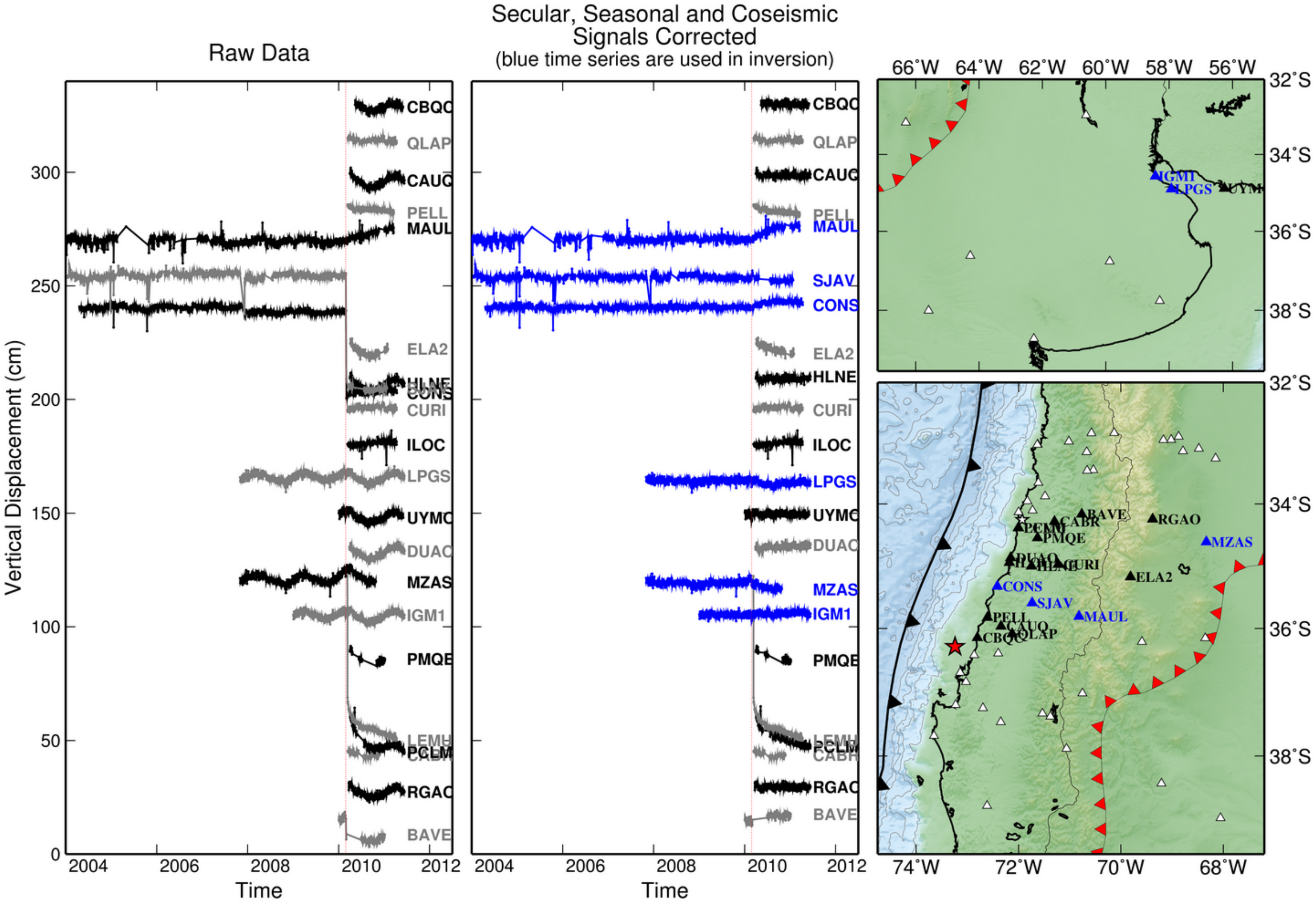

Figure S1-2

The vertical components of the cGPS time series. [Left] Raw time series. [Middle] The secular rates are estimated only with the long time series (with more than 1.5 years of records before the Maule earthquake). The seasonal variations are estimated with every time series. The coseismic jump is estimated whenever the time series span through the earthquake. [Right] The location of the stations. Blue stations are the ones picked for the postseismic slip inversion.

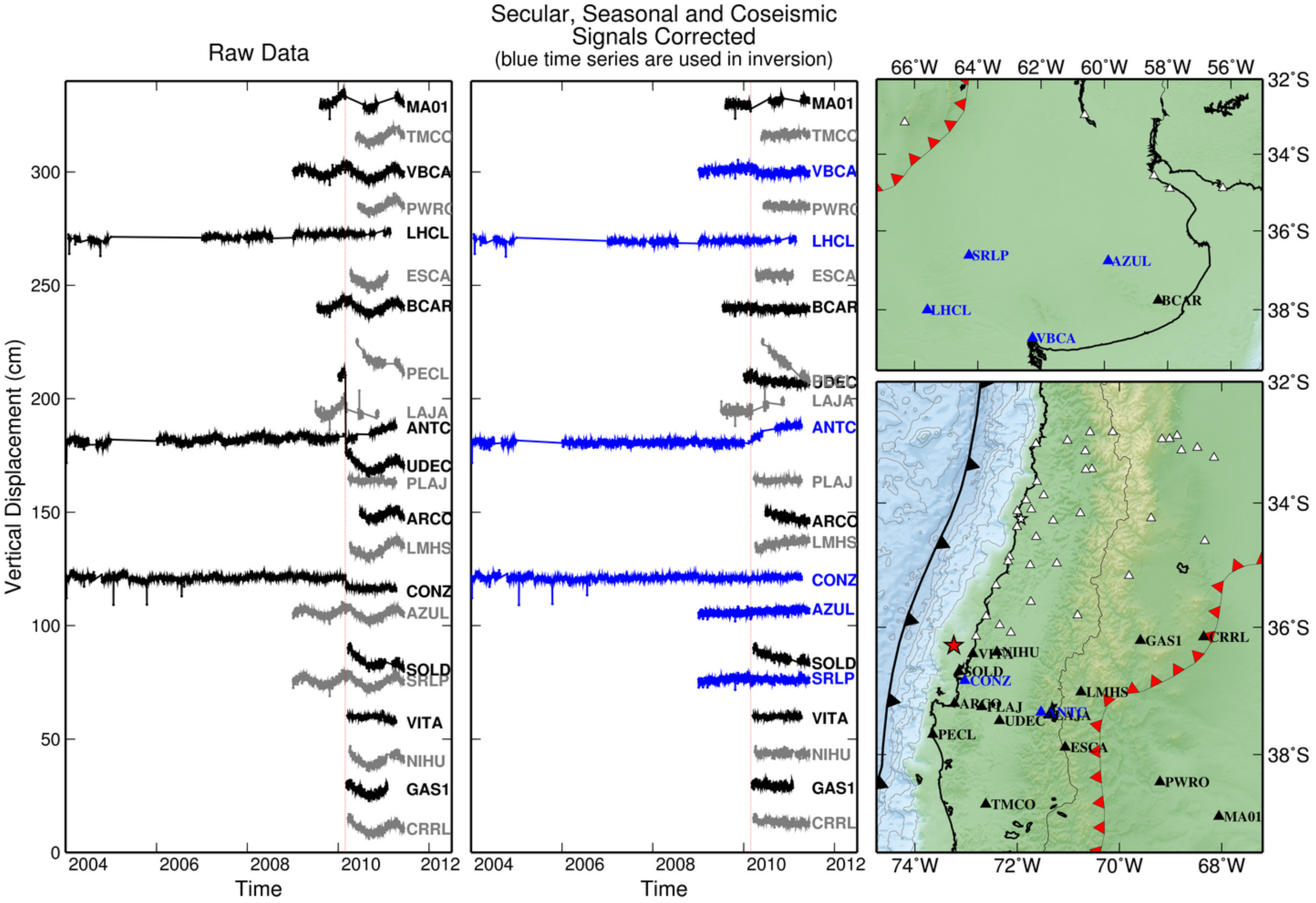

Figure S1-3

The vertical components of the cGPS time series. [Left] Raw time series. [Middle] The secular rates are estimated only with the long time series (with more than 1.5 years of records before the Maule earthquake). The seasonal variations are estimated with every time series. The coseismic jump is estimated whenever the time series span through the earthquake. [Right] The location of the stations. Blue stations are the ones picked for the postseismic slip inversion.

2. Inversion Models

2.1 Coseismic Model

To solve for the distribution of coseismic slip of the Maule earthquake, we perform a joint inversion of all the static data previously described (i.e. InSAR and GPS) as well as teleseismic body waves. We use a simulated-annealing algorithm [Ji et al., 2002] to solve this non-linear optimization problem. We use a fault geometry consisting of two fault segments aligned along strike to accommodate the curvature of the trench. Those segments also have variable dip angles to better approximate the shallower dip angle of the slab south of the Arauco peninsula. This geometry shows a very good agreement (**Fig. S2**) with the USGS 3D slab model [Hayes et al., 2009]. The fault geometry is discretized into 292 elements of 30 km x 15 km. For each fault element, we solve for 4 parameters: the slip amplitude and rake, as well as rupture initiation time and duration. The time evolution of each fault element is constructed using half-cosine functions with a minimum rise-time of 1 s. To limit the size of the parameter space as well as to account for uncertainties in the data and model (292x4 unknowns), we include Laplacian regularization term in the cost function that is minimized during the inversion procedure. We use the epicenter location estimate of Vigny et al. [2011]: 36.41°S and 73.18°W. Any given segment of the fault is only allowed to rupture once and its velocity is bounded in the 2.5 to 3 km/s range [Delouis et al., 2010; Vigny et al., 2011].

We selected 24 P waveforms from the GSN global broadband network. To avoid triplication in the crust and upper mantle, or diffraction at the core-mantle boundary, we selected stations in the 30-90° distance range (teleseismic range; **Fig. 5A**). In that distance range, stations are selected to provide a good azimuthal coverage thereby maximizing the resolution on the slip history. We use a 2.5 second to 200 second bandpass (0.005-0.4 Hz) on the seismograms (**Fig. 5B**) and both the teleseismic and geodetic Green's functions are computed in a 1D layered elastic half-space. The velocity and density model is derived from the global 3D CRUST2.0 model [Bassin et al., 2000] for a point on the coast at the latitude of the epicenter.

In the inversion, InSAR and GPS datasets are given equal weight. Because of the strong trade-offs in the rupture-process estimation [e.g. Lay et al., 2010] and the lower resolution [e.g. Delouis et al., 2010] while using only the teleseismic data, we double the weight of the geodetic data in the cost function relative to the teleseismic data. The contribution of the moment and smoothing regularization in the cost function follows Ji et al. [2002].

2.2 Postseismic Model

To derive the time-dependent finite source kinematic models, we use the Principle Component Analysis-based Inversion Method (PCAIM) developed by Kositsky and Avouac [2010]. This approach allows the joint inversion of multiple geodetic datasets with various spatiotemporal resolutions [Lin et al., 2010b]. The two datasets we use in our model, GPS and InSAR data, provide complementary constraints on the temporal and spatial evolution of slip and therefore a joint inversion is crucial for understanding the detailed evolution of the postseismic creep. In our modified version of PCAIM, we only use the GPS data for the PCA. During the inversion stage, we apply InSAR data as extra constraints that bridge through different components. This adaptation from the method described in Lin et al. [2010b] is due to the temporal sparsity of the InSAR data in this study (only 1-4 epochs for most of the ALOS tracks), making the joint decomposition not necessarily beneficial. With this adaptation, sparse InSAR data still provides a significant constraint.

Since afterslip may occur on significantly deeper portions of the fault, the model fault extends deeper and further along strike than that used in the coseismic model (**Fig. S2**). For the post-seismic model, we reduce our spatial resolution to limit the computational cost of the inversion, and take into account the curved geometry of the fault plane. Our fault geometry is constrained by: (1) reflection seismic profiles [Contreras-Reyes et al., 2008a; Contreras-Reyes et al., 2008b], (2) background seismicity before the mainshock [Campos et al., 2002; Rietbrock et al., 2005; Haberland et al., 2009], and (3) the distribution of aftershocks [Rietbrock et al., 2012]. The shallow part of the geometry (0~25 km) is primarily constrained by reflection seismic profiles, whereas the deeper part between 25 and 150 km are primarily constrained by seismicity. The resulting fault plane is slightly deeper than SLAB 1.0 [Hayes et al., 2009] for depths greater than 40 km, but agrees well with the relocated earthquakes from the NEIC and ISC catalog for the time period between February to September 2010 (**Fig. S5**) [Pesicek et al., 2012]. We tessellate the fault plane into a 30 km x 30 km "magic carpet" of square patches that respect the original curvature of the megathrust geometry. The elastic Green's functions are computed by using the same 1D layered structure as used for the coseismic slip model.

We use an F-test to determine the number of principle components used in the inversion, a procedure described in Kositsky and Avouac [2010]. Then we define our objective function $\Phi(\lambda) = \|\mathbf{C}(\mathbf{Gm} - \mathbf{d})\|_2 + \lambda\|\mathbf{WDm}\|_2$, where $\mathbf{C}$ is the Cholesky decomposition of the data covariance matrix , $\mathbf{m}$ is the slip on each fault patch, $\mathbf{D}$ is the Laplacian operator, $\mathbf{W}$ is a shape function that controls the differential Laplacian applied on each part of the fault model, and λ is the weighting over the regularization term [Lohman, 2004]. $\mathbf{W}$ is defined as the reciprocal of the fault slip sensitivity $\mathbf{S} = [1/\mathrm{diag}(\mathbf{G}^T\mathbf{G})]^{1/2}$ [Ortega-Culaciati et al., 2013]. Each element in the vector $\mathbf{S}$ represents the summation of the displacements over all GPS stations and/or InSAR pixels due to unit slip on each individual patch, and corresponds to a measure of the resolution power of the observational constraints [Loveless and Meade, 2011] or equivalently a relative measure of the capacity of the fault slip for each path to be constrained by the available observations [Ortega-Culaciati et al., 2013]. **Figure S6** shows that the highest sensitivity occurs for regions of the fault model between 10 and 80 km at depth in the north, and can extend close to the trench near the Arauco Peninsula. **W**, defined in terms of the reciprocal of this sensitivity vector, will assign more smoothing to regions with smaller sensitivity and less smoothing to those with higher sensitivity. Using **W** as defined here limits the introduction of smearing of resolved slip variability into regions that are less constrained, improves the stability of the slip distribution and enables us to infer overall rougher slip models while imposing a stronger smoothing in regions that are less constrained by the observables [Ortega-Culaciati et al., 2013]. In regions of low sensitivity, such as the shallowest and the deepest parts of the megathrust, while the resolved slip is close to an average low resolution value of the region with limited observational constraints – slip is not pushed to a zero value (**Fig. S7**).

In addition to the aforementioned regularization terms, we enforce positivity in the up-dip slip direction. Under the assumption that the strike-slip components tend to vary more gradually in space than the dip-slip components, we choose by trial and error the relative damping of the strike-slip components to be a 1000 times larger than for the dip-slip components. We use a conventional L-curve method to determine the best λ.

To partially account for the fact that the Green's functions used will always be approximate, we incorporate an additional "prediction error" term in the error model. Minson et al. [2013] address this issue by assigning prediction errors that scale with the magnitude of data, under the assumption that the larger the observational response, the larger the prediction error in the response. Here, we assume that the Green's functions are good to about 5%. The final error model, E, is thus $E = E_{obs} + E_{pred}*0.05$. This is a crude approach to accounting for the prediction error, one that ignores covariances that are also induced by errors in our assumed Green's functions. Our data fits are shown in **Fig. 4** & **8**.

For the postseismic InSAR data, we adopted a more sophisticated approach to deal with the systematic error associated with inaccurate orbit information. All the sub-swaths of descending track 422 share the same orbit, and therefore a single large ramp should be estimated jointly, whereas the ramp for each ascending track is estimated separately. The approach better avoids mixing the postseismic deformation signals with the bilinear ramp. The mean RMS residual is 2.5 cm for the InSAR data (**Fig. 4**), a value consistent with the range of atmospheric delays observed elsewhere [Mockler 1995; Li et al., 2003].

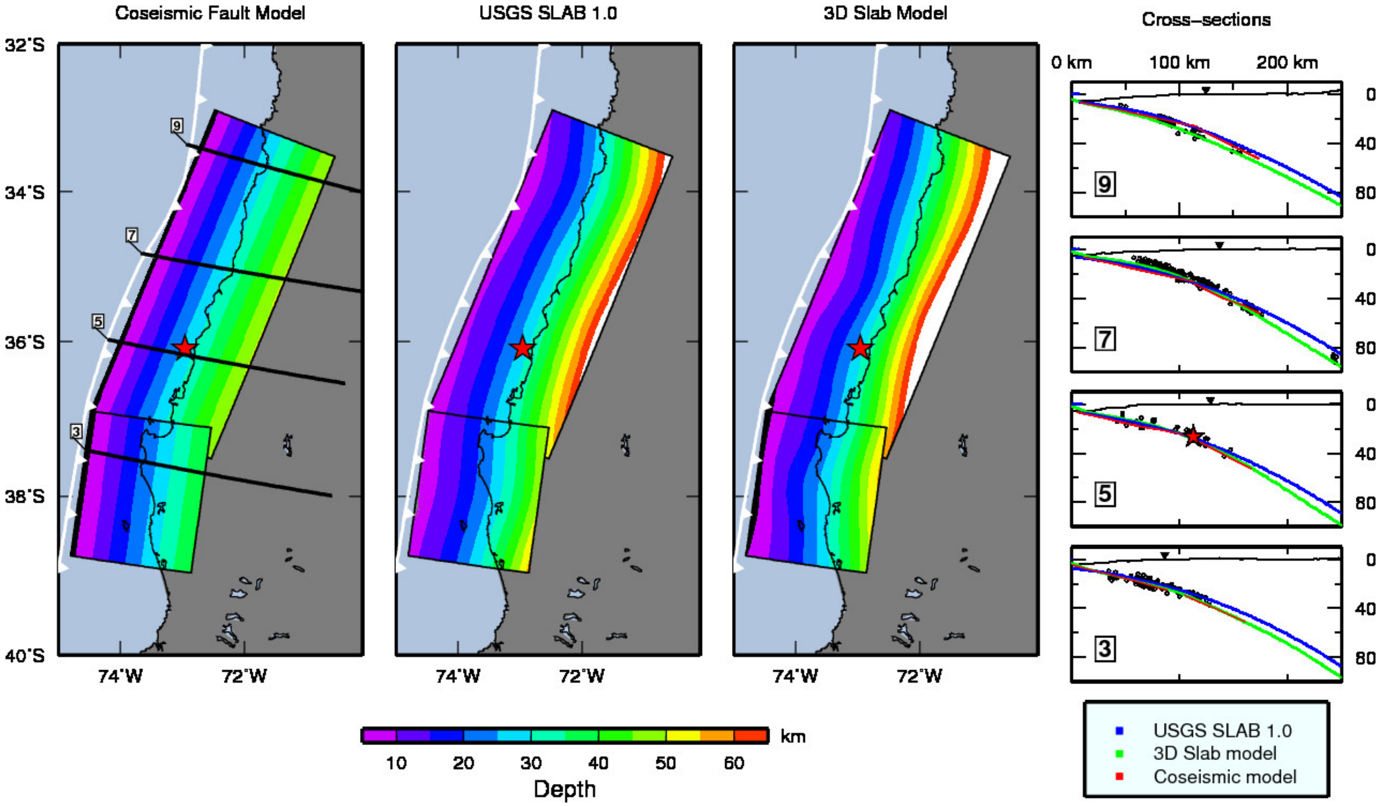

Figure S2

Comparisons between the coseismic fault geometry, USGS SLAB 1.0 [Hayes et al., 2009] and the 3D slab model used in the postseismic slip model. The coseismic model is composed of two fault planes to describe the changes of dip angles from north to south. The postseismic model is meshed by using constraints from seismicity [Campos et al., 2002; Rietbrock e tal., 2005; Haberland et al., 2009; Rietbrock et al., 2012] and reflection seismic profiles [Contreras-Reyes et al., 2008a; Contreras-Reyes et al., 2008b].

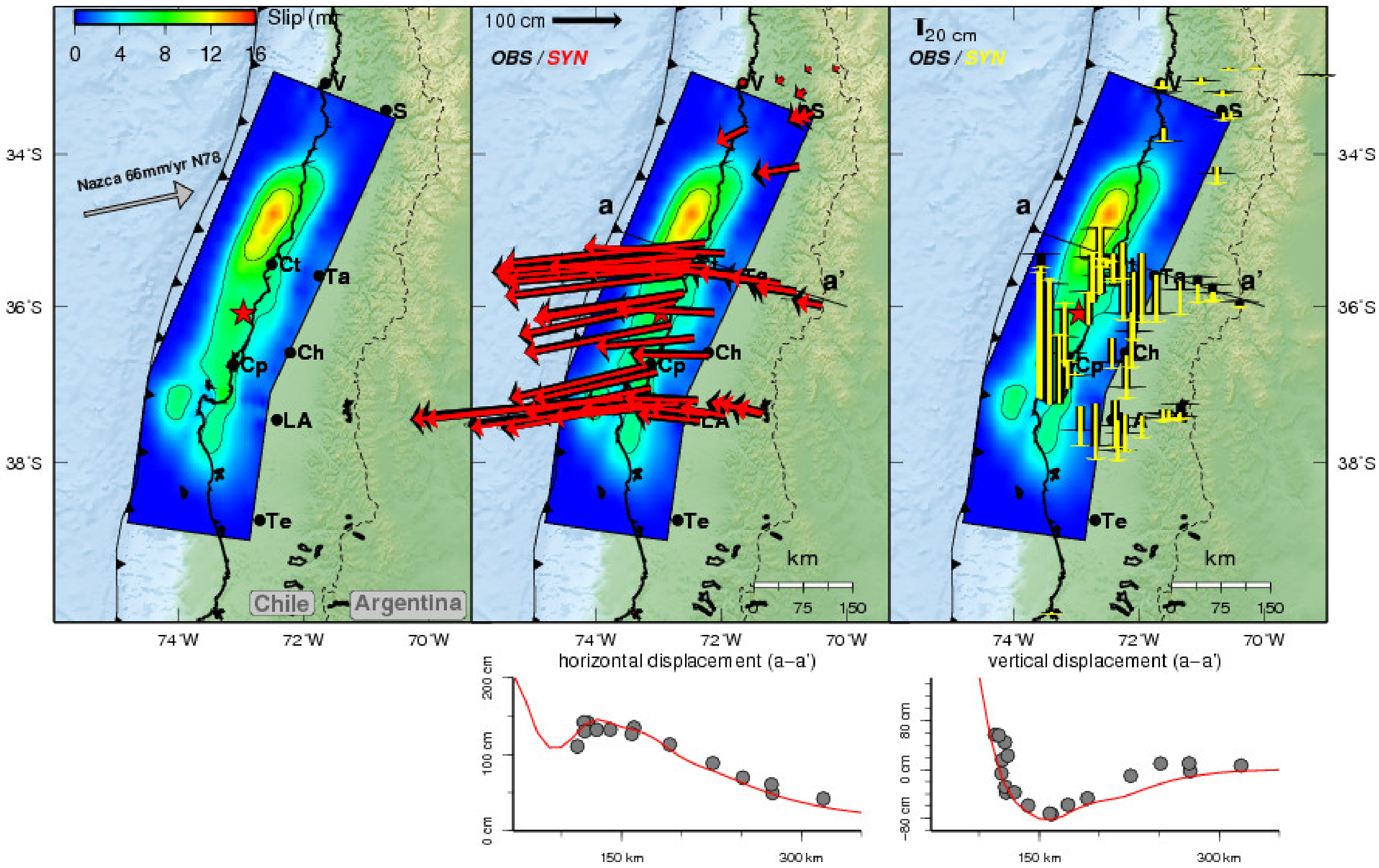

Figure S3

Results from geodetic-only inversion. (Left) Coseismic slip with 5-m contour intervals. (Center and Right) Black vectors indicate the observed GPS data; red and yellow vectors indicate modeled results in the horizontal and vertical components, respectively. The profile (aa') shows the predicted (red line) and observed (grey solid dots) surface displacements at the latitude of the main asperity, around latitude 36°S. Notice that for the vertical components (right), the slip model predicts a displacement field of longer wavelength than the observed data, a result similar to the kinematic source model shown in **Fig. 6**. STF: Source time function. Ch: Chillán; Ct: Constitución; Cp: Concepción; LA: Los Angeles; Ta: Talca; Te: Temuco; S: Santiago; V: Valparaiso.

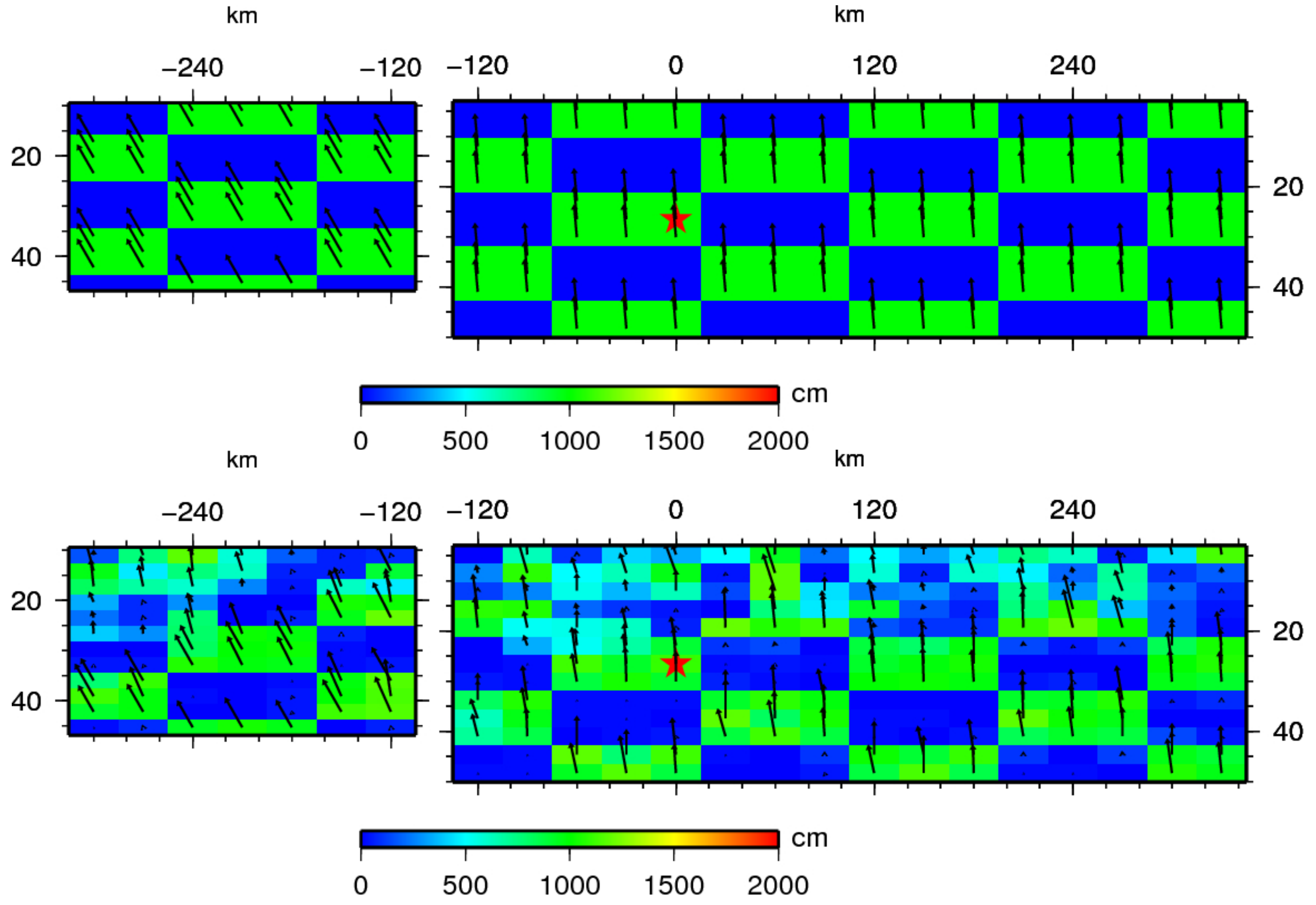

Figure S4

Checkerboard test for the geodetic-only inversion (InSAR+GPS). (Top) Pattern of the checkerboard slip distribution. (Bottom) Pattern recovered from the inversion of the synthetic data allowing the rake to vary on each cell. The model obtained from inversion clearly shows the decrease in resolution for the patches less than 15 km depth.

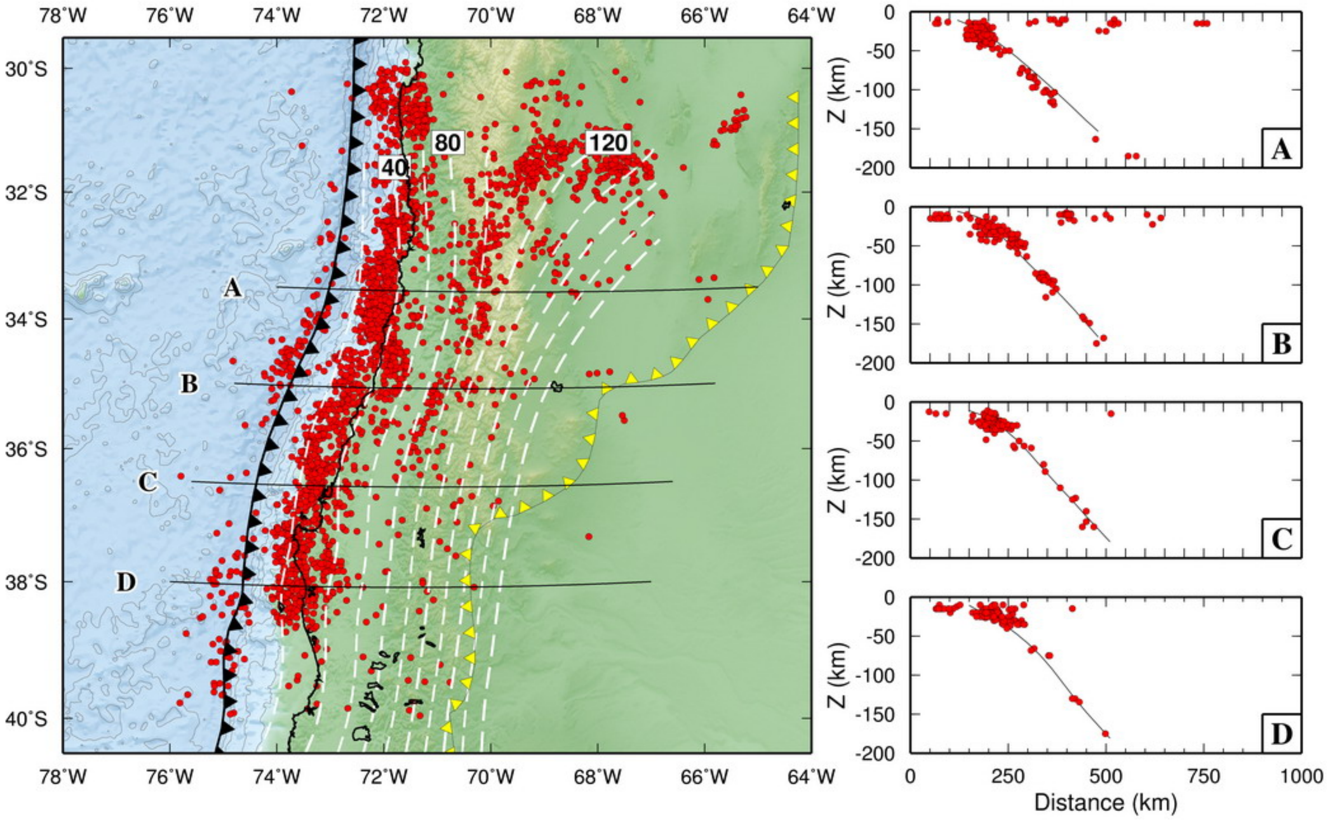

Figure S5

We compare the fault geometry for our postseismic model (white dashed lines for the contours) with the relocated earthquakes from the NEIC and ISC catalog for the time period between February to September 2010 (Pesicek et al. [2012], red circles). These earthquakes were not used in estimating the slab geometry. (A)-(D) The geometry agrees well with the location of earthquakes on the subduction zone interface to depths of at least 200 km, thereby validating the reconstruction of the fault plane.

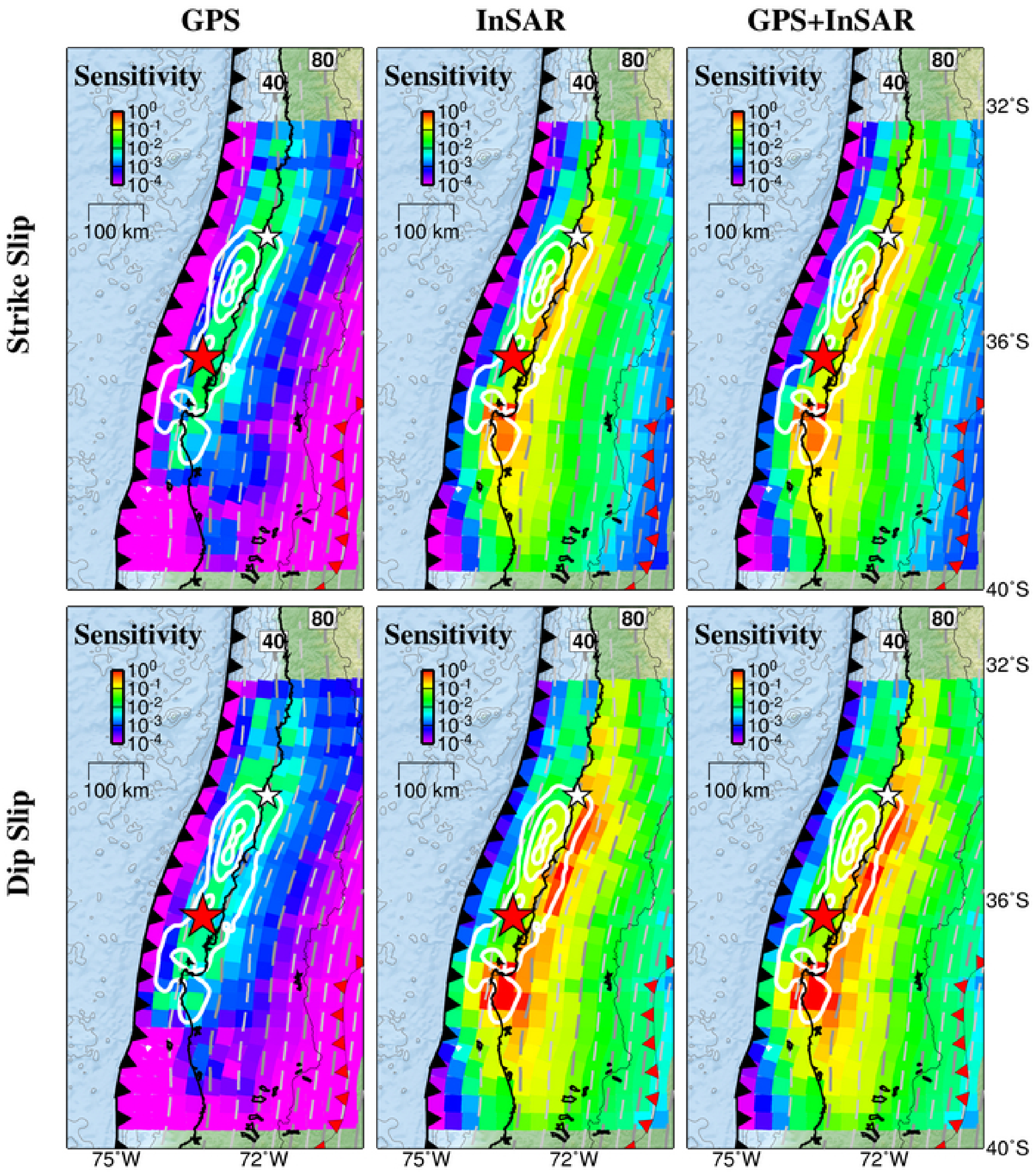

Figure S6

Postseismic model sensitivity for the strike-slip and dip-slip component when using GPS only (left), InSAR only (middle) and the GPS+InSAR joint dataset (right). Use of the joint dataset constrained maximizes the fraction of the model that is well constrained.

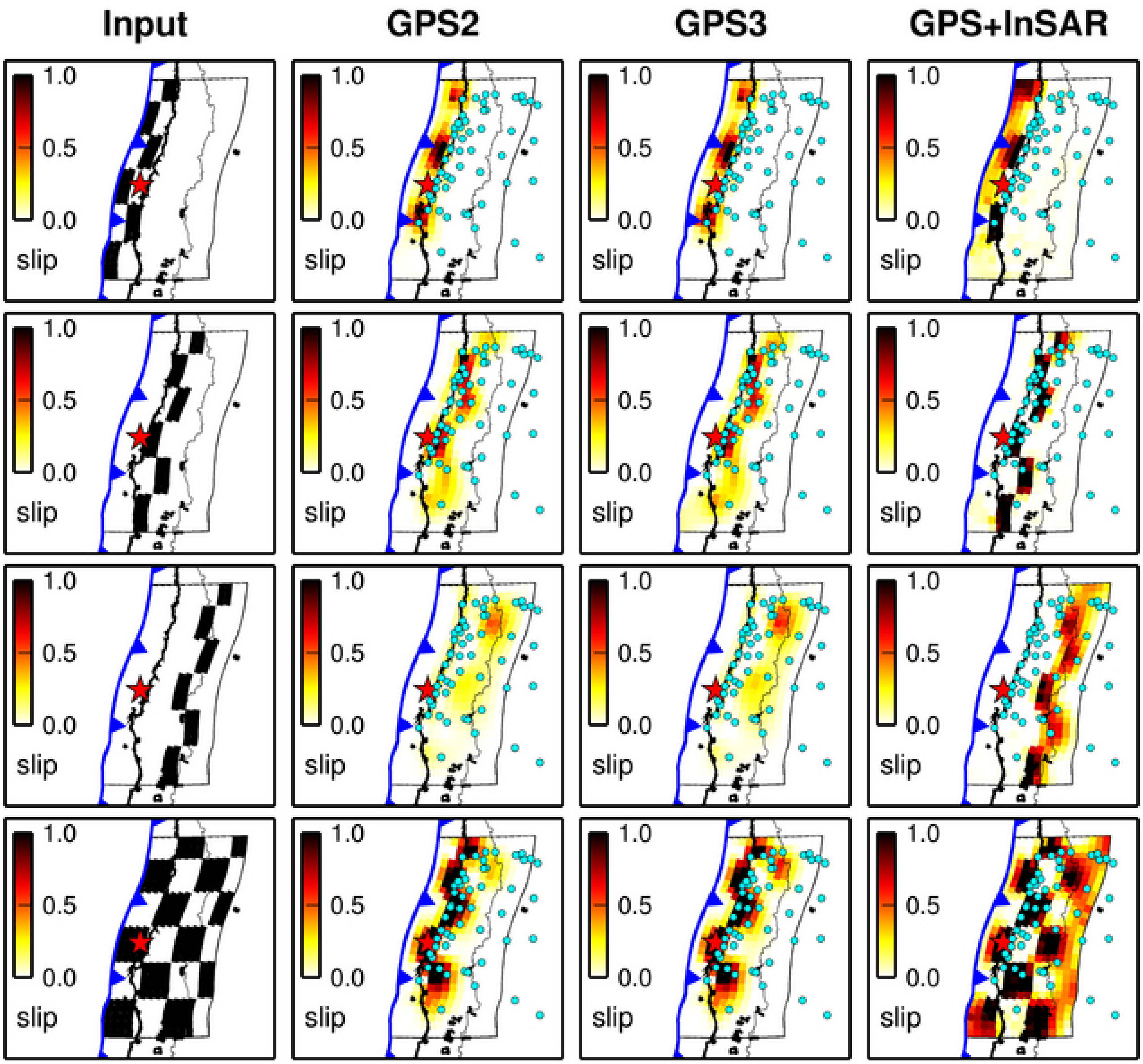

Figure S7

Checkerboard tests used for the postseismic inversion modeling. These tests assume observation errors of 5 mm in the GPS horizontal components and 15 mm in the GPS vertical components. Systematic bilinear ramps in the InSAR data and observation errors are derived following Lohman and Simons [2005]. This test shows that the lack of model sensitivity at shallowest and deepest depths (**Fig. S5**) leads to more smeared and averaged slip patterns (last column).

3. Effects of Approximate Green's Function

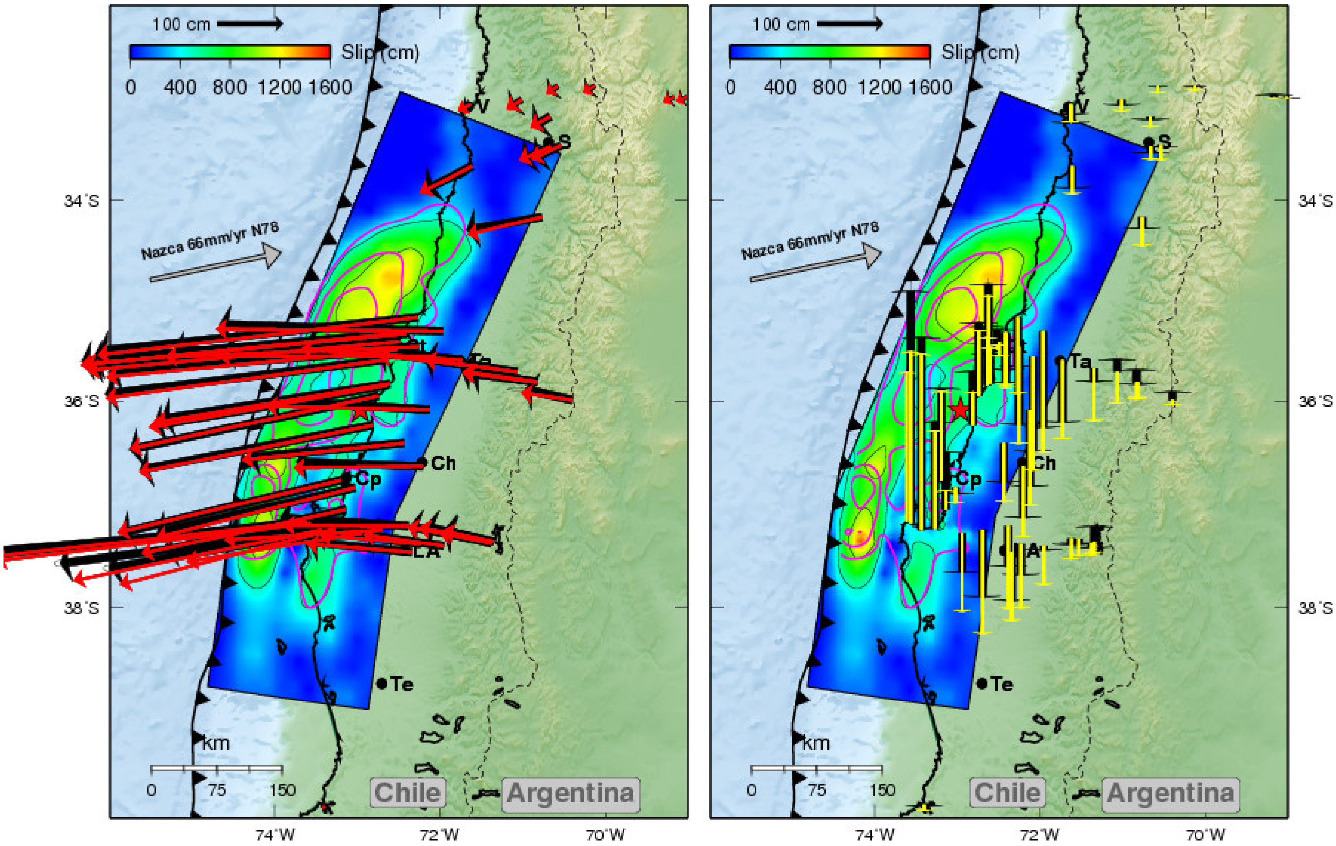

Figure S8

Coseismic slip distribution, with 5-m contour intervals, obtained using the semi-inifite elastic half-space approximation instead of the layered elastic half-space approximation used for our preferred slip model (**Fig. 6**). This model is overlain with the contours of Vigny et al. [2011] slip model (pink) which also uses the semi-infinite elastic half-space approximation. Black vectors are for observed GPS data; red and yellow vectors are for modeled results in the horizontal and vertical components. Both models shown here have a similar spatial extent and suggest a slip distribution shifted much closer to the trench than our prefered slip model using a layered elastic half-space (**Fig. 6**). This comparison illustrates the influence of the physical model approximations on the solution.

4. Resolution of Updip Slip Extent from Tsunami Data

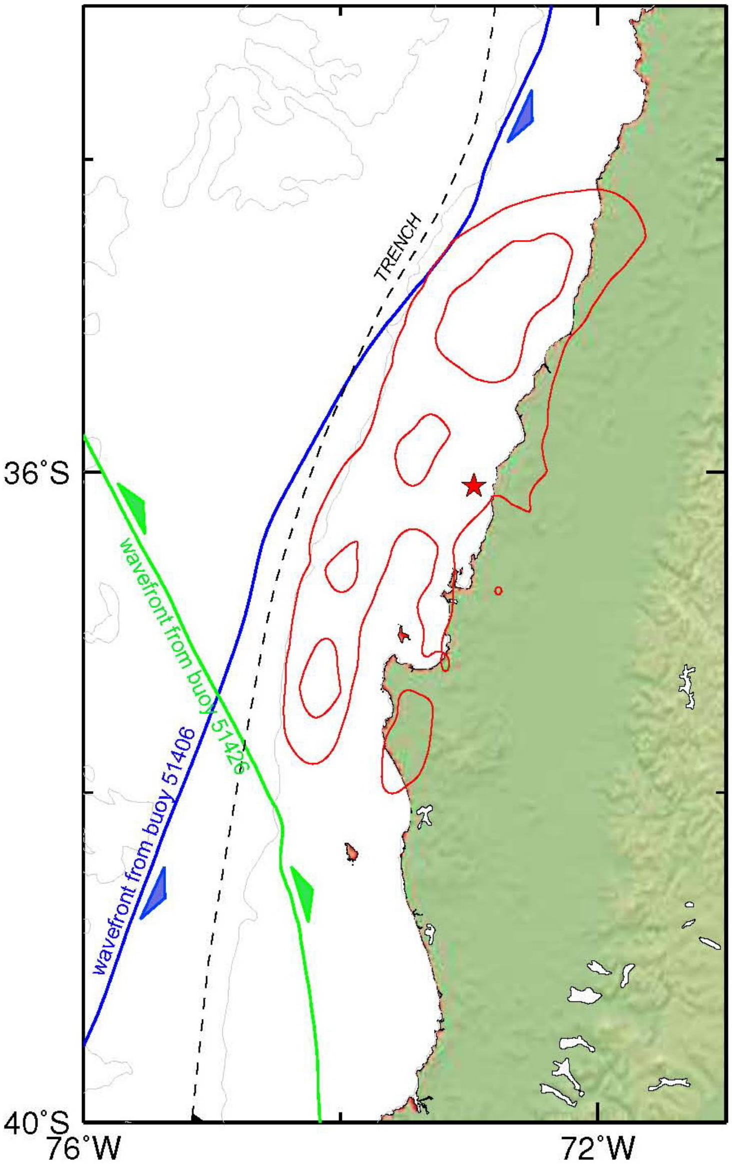

Figure S9

Tsunami wavefronts propagated from the deep-ocean buoys 51406 (blue wave front) and 51426 (greenwave front) (see Fig. 8 for the location map). The wavefront from buoy 51426 is representative of the group of buoys in the same distance range and azimuth —51425, 51426, 54401— of the southwest Pacific. Red contours correspond to 5-m slip contours of our preferred slip model. The red star is the mainshock epicenter. The tsunami wavefronts indicate that only station 51406 is a good discriminant of the updip extent of the source; for station 51426 and others nearby, the tsunami signal from the updip part of the source will be mixed with waves coming from the southern part of the fault.

5. Slip Potency Test for Shallow Slip

To test what is the likelihood of slip in the shallow part of the megathrust, we modify our objective function to

$$\Phi(\lambda_1,\lambda_2) = \|\mathbf{C}(\mathbf{Gm}-\mathbf{d})\|_2 + \lambda_1\|\mathbf{WDm}\|_2 + \lambda_2\|\mathbf{mA}\text{-}P_o\|_2 \tag{S1}$$

where P_o is the slip potency equivalent to that of the mainshock, and λ_2 is the strength of this extra term of regularization. We apply this regularization term only to patches above 80 m deep. The assumption here is that the creeping energy on the megathrust from 0-80 km at depth within the first 488 days of the postseismic period does not exceed the energy released by the mainshock.

Figure S10 shows the plot of model roughness (in terms of moment magnitude) versus model bias (in terms of mean RMS for time series) for different values of the slip potency constraint (λ_2). Here instead of choosing the "knee" of the L-curve, we determine the reliable range by choosing the λ_2 values within an identical level of RMS (i.e., between 0 and 100). **Figure S11** shows the postseismic slip models with selected values of λ_2. Right column shows the residual vectors of various time spans, reflecting the actual data length of each station (**Table S1**). For the largest λ_2 value within the reliable range (λ_2=100), there is some shallow slip near the trench, but the values are quite small. We therefore conclude if there were any shallow slip during the postseismic period, the amount needs to be small.

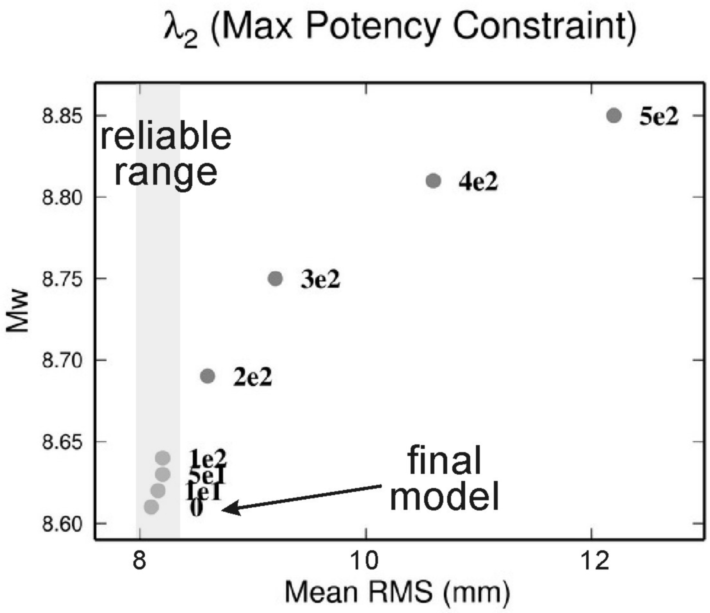

Figure S10

The L-curve test of λ_2 for slip potency test at the shallowest part of the megathrust. The grey band shows the region where the RMS values clusters and therefore is considered as a reliable range of λ_2.

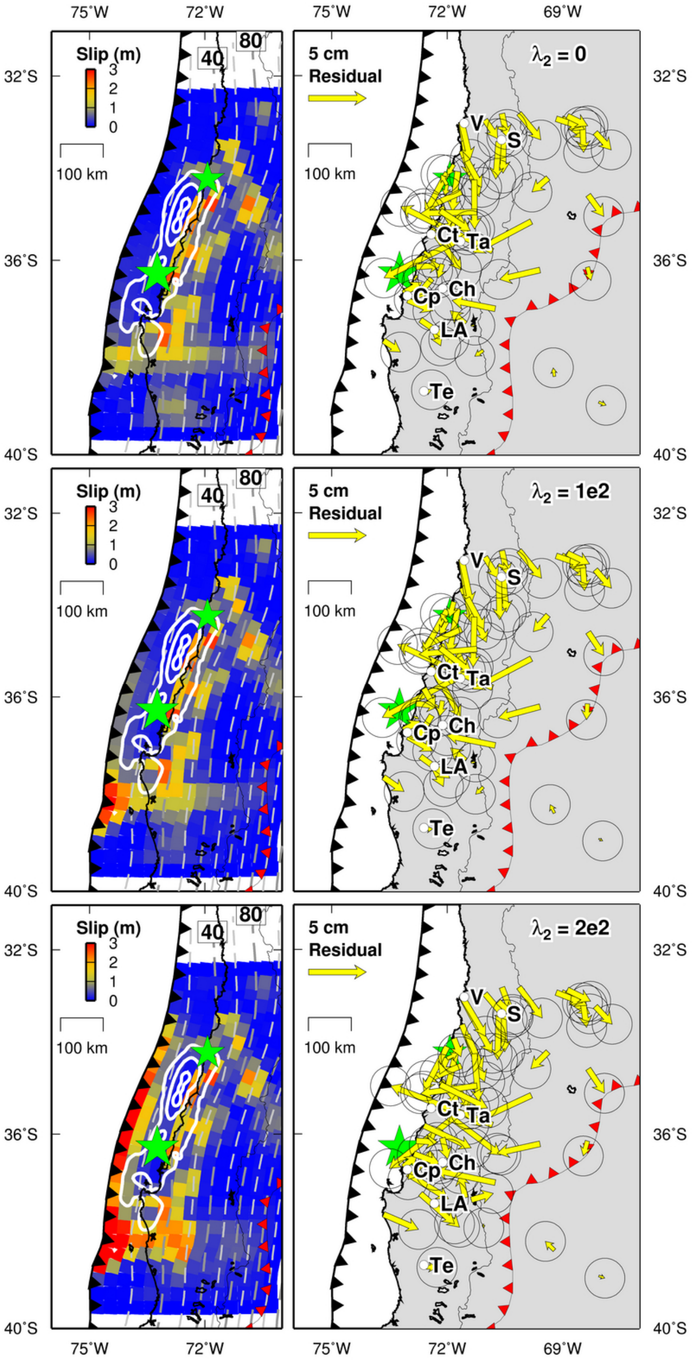

Figure S11

The slip models (left panel) and the corresponding residuals in the GPS horizontal components (right panel) for the λ_2 value of 0, 100 and 200. For the largest λ_2 value within the reliable range (λ_2=100), the shallow slip is still small compared to other part of the megathrust.

6. Comparison between Slip Models and Aftershock Focal Mechanisms

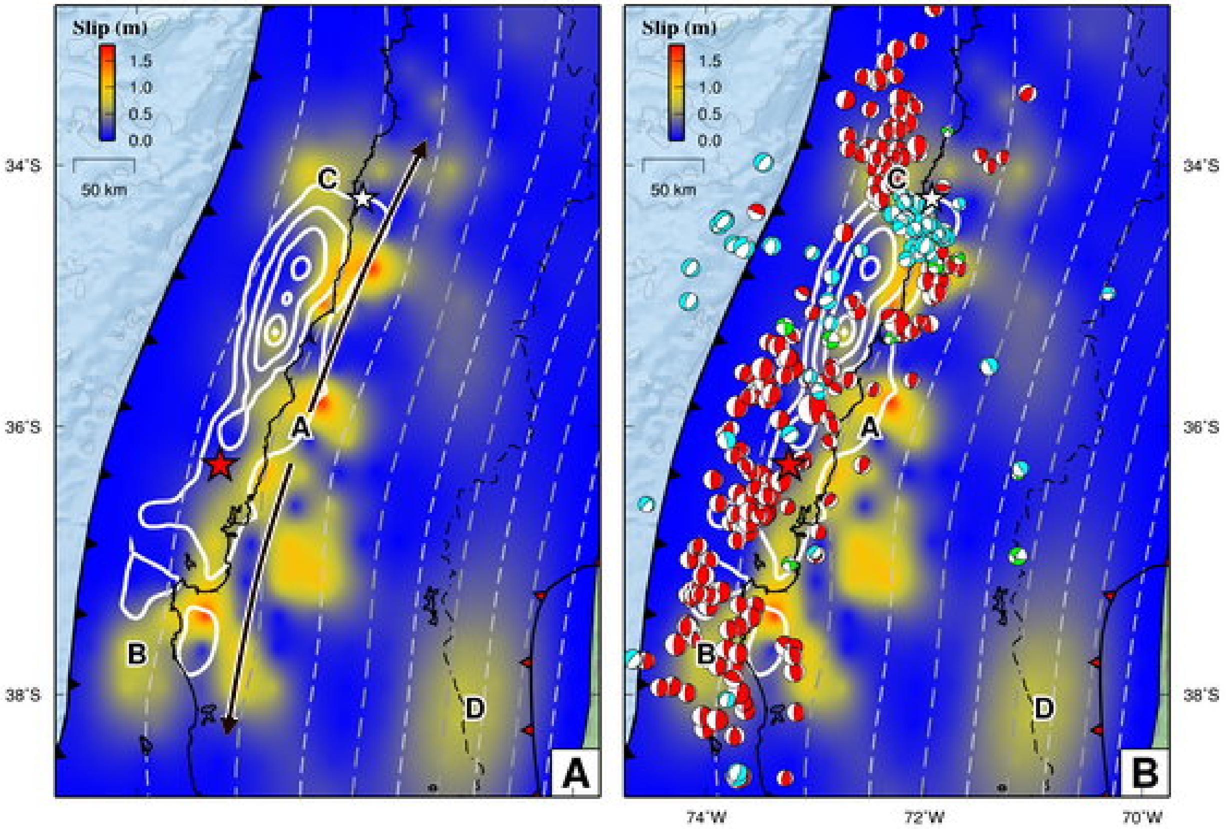

Figure S12

Comparison between the slip models derived from this study and the focal mechanisms for Maule aftershocks [Agurto et al., 2012]. (A) Color maps are the postseismic slip model, overlain with white contours of the coseismic slip model. (B) Focal mechanisms of M>4 aftershocks. Red: thrust event; cyan: normal event; green: strike-slip event. There are many M>4 events along the up-dip side of the coseismic slip patch between 35.5 and 38.5° S, suggesting seismically-related afterslip along the shallow section of the megathrust, whereas along the down-dip side of the coseismic patch it is mostly the geodetic data that allows us to resolve afterslip.

Reference

Agurto, H., A. Rietbrock, I. Ryder, and M. Miller (2012), Seismic-afterslip characterization of the 2010 MW 8.8 Maule, Chile, earthquake based on moment tensor inversion, *Geophys. Res. Lett.*, *39*, L20303, doi: doi:10.1029/2012GL053434.

Bassin, C., G. Laske, and G. Masters (2000), The current limits of resolution for surface wave tomography in North America, paper presented at Fall. Meet. Suppl., Abstract S12A-03, 2001.

Bevis, M., Y. Bock, P. Fang, R. Reilinger, T. Herring, J. Stowell, and R. Smalley (1997), Blending old and new approaches to regional GPS geodesy, *Eos, Transactions American Geophysical Union*, *78*(6), 61-66, doi: 10.1029/97e000040.

Brooks, B. A., M. Bevis, R. Smalley, Jr., E. Kendrick, R. Manceda, E. Lauría, R. Maturana, and M. Araujo (2003), Crustal motion in the Southern Andes (26°-36°S): Do the Andes behave like a microplate?, *Geochem. Geophys. Geosyst.*, *4*(10), 1085, doi: 10.1029/2003gc000505.

Brooks, B. A., et al. (2011), Orogenic-wedge deformation and potential for great earthquakes in the central Andean backarc, *Nat. Geosci.*, *4*(6), 380-383, doi: 10.1038/ngeo1143.

Campos, J., D. Hatzfeld, R. Madariaga, G. Lopez, E. Kausel, A. Zollo, G. Iannacone, R. Fromm, S. Barrientos, and H. Lyon-Caen (2002), A seismological study of the 1835 seismic gap in south-central Chile, *Phys. Earth Planet. In.*, *132*(1-3), 177-195, doi: 10.1016/S0031-9201(02)00051-1.

Contreras-Reyes, E., I. Grevemeyer, E. R. Flueh, and C. Reichert (2008), Upper lithospheric structure of the subduction zone offshore of southern Arauco peninsula, Chile, at ~38°S, *J. Geophys. Res.*, *113*(B7), B07303, doi: 10.1029/2007JB005569.

Contreras-Reyes, E., I. Grevemeyer, E. R. Flueh, M. Scherwath, and J. Bialas (2008), Effect of trench-outer rise bending-related faulting on seismic Poisson's ratio and mantle anisotropy: a case study offshore of Southern Central Chile, *Geophys. J. Int.*, *173*(1), 142-156, doi: 10.1111/j.1365-246X.2008.03716.x.

Delouis, B., J.-M. Nocquet, and M. Vallee (2010), Slip distribution of the February 27, 2010 Mw=8.8 Maule Earthquake, central Chile, from static and high-rate GPS, InSAR, and broadband teleseismic data, *Geophys. Res. Lett.*, *37*, L17305, doi: 10.1029/2010GL043899.

Haberland, C., A. Rietbrock, D. Lange, K. Bataille, and T. Dahm (2009), Structure of the seismogenic zone of the southcentral Chilean margin revealed by local earthquake traveltime tomography, *J. Geophys. Res.*, *114*, B01317, doi: 10.1029/2008JB005802.

Hayes, G. P., D. J. Wald, and K. Keranen (2009), Advancing techniques to constrain the geometry of the seismic rupture plane on subduction interfaces a priori: Higher-order functional fits, *Geochem. Geophys. Geosyst.*, *10*(9), Q09006, doi: 10.1029/2009GC002633.

Herring, T. A. (2000), Documentation for GLOBK: Global Kalman filter VLBI and GPS analysis program, edited, MIT.

Hu, Y., K. Wang, J. He, J. Klotz, and G. Khazaradze (2004), Three-dimensional viscoelastic finite element model for postseismic deformation of the great 1960 Chile earthquake, *J. Geophys. Res.*, *109*(B12), B12403, doi: 10.1029/2004JB003163.

Ji, C., D. J. Wald, and D. V. Helmberger (2002), Source description of the 1999 Hector Mine, California, earthquake, part I: Wavelet domain inversion theory and resolution analysis, *B. Seismol. Soc. Am.*, *92*(4), 1192-1207, doi: 10.1785/0120000916.

Kendrick, E., M. Bevis, R. Smalley, B. Brooks, R. B. Vargas, E. Lauriia, and L. P. S. Fortes (2003), The Nazca South America Euler vector and its rate of change, *J. S. Am. Earth Sci.*, *16*(2), 125-131, doi: 10.1016/S0895-9811(03)00028-2.

King, R. W., and Y. Bock (2000), *Documentation for the GAMIT GPS Analysis Software Version 10.0*, 206 pp., Massachusetts Institute of Technology.

Kositsky, A., and J. P. Avouac (2010), Inverting geodetic time-series with a principal component analysis-based inverison method (PCAIM), *J. Geophys. Res.*, *115*, B03401, doi: 10.1029/2009JB006535.

Lay, T., C. J. Ammon, H. Kanamori, K. D. Koper, O. Sufri, and A. R. Hutko (2010), Teleseismic inversion for rupture process of the 27 February 2010 Chile (M-w 8.8) earthquake, *Geophys. Res. Lett.*, *37*, L13301, doi: 10.1029/2010GL043379.

Li, Z., J.-P. Muller, and P. Cross (2003), Comparison of precipitable water vapor derived from radiosonde, GPS, and Moderate-Resolution Imaging Spectroradiometer measurements, *Journal of Geophysical Research: Atmospheres*, *108*(D20), 4651, doi: 10.1029/2003jd003372.

Lin, Y.-N. N., M. Simons, E. A. Hetland, P. Muse, and C. DiCaprio (2010a), A multiscale approach to estimating topographically correlated propagation delays in radar interferograms, *Geochem. Geophys. Geosyst.*, *11*(9), Q09002, doi: 10.1029/2010GC003228.

Lin, Y.-N. N., A. P. Kositsky, and J.-P. Avouac (2010b), PCAIM joint inversion of InSAR and ground-based geodetic time series: Application to monitoring magmatic inflation beneath the Long Valley Caldera, *Geophys. Res. Lett.*, *37*(23), L23301, doi: 10.1029/2010GL045769.

Lohman, R. B. (2004), The inversion of geodetic data for earthquake parameters, California Institute of Technology.

Lohman, R. B., and M. Simons (2005), Some thoughts on the use of InSAR data to constrain models of surface deformation: Noise structure and data downsampling, *Geochem. Geophys. Geosyst.*, *6*, Q01007, doi: 10.1029/2004GC000841.

Loveless, J. P., and B. J. Meade (2011), Spatial correlation of interseismic coupling and coseismic rupture extent of the 2011 MW = 9.0 Tohoku-oki earthquake, *Geophys. Res. Lett.*, *38*(17), L17306, doi: 10.1029/2011GL048561.

Minson, S., M. Simons, and J. L. Beck (2013), Bayesian inversion for finite fault earthquake source models I — Theory and algorithm, *Geophys. J. Int.*, doi: 10.1093/gji/ggt180.

Mockler, S. B. (1995), Water vapor in the climate system, AGU, Washington, D. C.

Moreno, M. S., J. Klotz, D. Melnick, H. Echtler, and K. Bataille (2008), Active faulting and heterogeneous deformation across a megathrust segment boundary from GPS data, south central Chile (36-39°S), *Geochem. Geophys. Geosyst.*, *9*, Q12024, doi: 10.1029/2008GC002198.

Moreno, M., et al. (2012), Toward understanding tectonic control on the Mw 8.8 2010 Maule Chile earthquake, *Earth Planet. Sci. Lett.*, *321-322*(0), 152-165, doi: 10.1016/j.epsl.2012.01.006.

Ortega-Culaciati, F. et al., (2013), Post-seismic deformation of the great 11 March 2011 Tohoku-Oki (Mw 9.0) earthquake, in preparation.

Pesicek, J. D., E. R. Engdahl, C. H. Thurber, H. R. DeShon, and D. Lange (2012), Mantle subducting slab structure in the region of the 2010 M8.8 Maule earthquake (30–40°S), Chile, *Geophys. J. Int.*, *191*(1), 317-324, doi: 10.1111/j.1365-246X.2012.05624.x.

Rietbrock, A., C. Haberland, K. Bataille, T. Dahm, and O. Oncken (2005), Studying the seismogenic coupling zone with a passive seismic array, *Eos Trans. AGU*, *86*, 293-300, doi: 10.1029/2005EO320001.

Rietbrock, A., I. Ryder, G. Hayes, C. Haberland, D. Comte, S. Roecker, and H. Lyon-Caen (2012), Aftershock seismicity of the 2010 Maule Mw=8.8, Chile, earthquake: Correlation between co-seismic slip models and aftershock distribution?, *Geophys. Res. Lett.*, *39*(8), L08310, doi: 10.1029/2012GL051308.

Ruegg, J. C., A. Rudloff, C. Vigny, R. Madariaga, J. B. de Chabalier, J. Campos, E. Kausel, S. Barrientos, and D. Dimitrov (2009), Interseismic strain accumulation measured by GPS in the seismic gap between Constitución and Concepción in Chile, *Phys. Earth Planet. Inter.*, *175*(1-2), 78-85, doi: 10.1016/j.pepi.2008.02.015.

Ryder, I., A. Rietbrock, K. Kelson, R. Bürgmann, M. Floyd, A. Socquet, C. Vigny, and D. Carrizo (2012), Large extensional aftershocks in the continental forearc triggered by the 2010 Maule earthquake, Chile, *Geophys. J. Int.*, *188*(3), 879-890, doi: 10.1111/j.1365-246X.2011.05321.x.

Vigny, C., et al. (2011), The 2010 Mw 8.8 Maule megathrust earthquake of central Chile, monitored by GPS, *Science*, *332*(6036), 1417-1421, doi: 10.1126/science.1204132.

Table S1: cGPS networks used in this study, data as of June 2011

Site	Position		Secular Rates* (mm/yr)			Uncertainties (mm/yr)			Postseismic** (cm)			Uncertainties (cm)			Time Span		
	Lon	Lat	Ve	Vn	Vz	Sve	Svn	Svz	Re	Rn	Rz	Sre	Srn	Srz	Start	End	# Epochs
ACPM	-70.537	-33.447							-10.124	-2.770	n/a	0.181	0.181	n/a	2010/01	2011/02	391
ALUM	-66.597	-27.323	5.159	-3.029	n/a	8.501	8.500	n/a							2009/01	2011/06	878
ANTC	-71.532	-37.339	14.790	0.717	4.522	0.414	0.413	1.488	-29.541	6.480	6.418	0.338	0.226	0.893	2004/01	2011/04	1873
ARCO	-73.226	-37.206							-16.286	-2.626	n/a	0.235	0.214	n/a	2010/06	2011/06	354
AREQ	-71.493	-16.466	4.331	-2.304	2.244	0.990	0.994	3.414							2007/01	2011/06	1597
AZUL	-59.881	-36.767	3.275	5.564	n/a	9.530	9.530	n/a	-1.729	-0.856	0.248	0.186	0.201	0.910	2009/01	2011/06	887
BAVE	-70.766	-34.168							-27.930	-0.775	n/a	0.182	0.179	n/a	2010/01	2011/01	243
BCAR	-58.301	-37.761							-1.232	-0.155	n/a	0.194	0.197	n/a	2009/06	2011/06	674
BRAZ	-47.878	-15.947	-0.356	0.750	-0.354	0.574	0.574	1.797							2007/01	2011/06	1530
BTON	-71.487	-30.263	18.440	8.025	3.316	0.826	0.768	2.601							2006/11	2011/04	1452
BUE1	-58.519	-34.574	2.321	3.083	n/a	2.253	2.244	n/a							2008/07	2010/08	757
CABR	-71.296	-34.286							-21.153	2.768	n/a	0.279	0.146	n/a	2010/03	2010/11	194
CATA	-65.774	-28.471	7.068	0.146	n/a	3.820	3.808	n/a							2009/01	2011/06	856
CAUQ	-72.341	-35.969							-27.122	-0.346	n/a	0.225	0.211	n/a	2010/03	2011/06	439
CBQC	-72.805	-36.147							-14.536	1.682	n/a	0.238	0.249	n/a	2010/05	2011/05	386
CFAG	-68.233	-31.602	6.782	2.877	0.696	2.504	2.487	3.386							2007/01	2010/12	1205
CMBA	-70.999	-31.188	21.216	6.604	6.550	0.982	0.973	3.102							2007/05	2011/02	1252
CNBA	-71.458	-31.398	25.474	7.550	10.803	1.586	1.560	5.745							2006/11	2010/11	1259
CONS	-72.412	-35.331	35.383	10.767	1.657	0.649	0.637	2.154	-22.984	1.791	2.864	0.311	0.200	0.736	2004/04	2011/04	2304
CONZ	-73.025	-36.844	32.839	10.810	0.882	0.342	0.339	1.227	-25.610	0.028	-0.093	0.271	0.217	0.849	2004/01	2011/04	2370
COPO	-70.338	-27.385	22.147	7.041	3.891	0.656	0.649	2.208							2004/01	2011/04	2000
CRRL	-68.354	-36.153							-10.596	1.652	n/a	0.197	0.199	n/a	2010/03	2011/06	447
CRZL	-71.410	-29.102	29.805	7.507	-3.214	4.296	2.814	8.972							2008/11	2010/11	683
CSJ1	-68.427	-31.981													2009/09	2011/06	579

CSLO	-69.302	-31.785													2009/06	2011/06	673
CUIB	-56.070	-15.555	1.928	-1.491	0.368	0.900	0.900	2.907							2007/01	2011/06	1594
CURI	-71.226	-34.977							-36.572	6.089	n/a	0.309	0.264	n/a	2010/03	2011/04	345
DGF1	-70.664	-33.457	20.819	6.200	5.445	0.380	0.375	1.569	-10.356	-1.496	3.003	0.333	0.200	1.120	2004/01	2011/04	2208
DUAO	-72.153	-34.873							-22.111	4.923	n/a	0.223	0.198	n/a	2010/03	2011/06	441
EBYP	-55.892	-27.369	0.628	0.594	-1.880	3.624	3.612	4.374							2009/01	2011/06	855
ELA2	-69.814	-35.180							-23.215	0.430	n/a	0.202	0.199	n/a	2010/04	2011/01	258
EMAT	-71.663	-31.147	29.234	8.926	-1.760	1.385	1.369	4.653							2007/05	2010/12	1025
ESCA	-71.061	-37.887							-19.626	3.659	n/a	0.312	0.316	n/a	2010/04	2011/01	296
ESQU	-71.323	-42.917	-3.677	5.198	n/a	5.876	5.968	n/a							2009/01	2011/06	834
GAS1	-69.589	-36.211							-19.210	3.413	n/a	0.201	0.202	n/a	2010/03	2011/01	332
HLNE	-71.745	-35.005							-27.330	2.193	n/a	0.211	0.210	n/a	2010/03	2011/06	420
IGM1	-58.439	-34.572	1.130	4.933	8.080	3.961	3.961	7.871	-0.737	-0.766	-0.285	0.177	0.198	0.932	2009/01	2011/06	887
ILOC	-72.179	-34.949							-18.627	3.125	n/a	0.267	0.230	n/a	2010/03	2011/04	344
IMBT	-48.656	-28.235	0.282	0.490	-0.219	0.981	0.980	3.492							2007/09	2011/05	1246
IQQE	-70.132	-20.274	24.562	4.206	5.853	1.611	1.612	5.307							2008/06	2011/06	1051
JUNT	-70.094	-29.977	17.249	5.472	2.604	1.444	1.439	5.085							2007/12	2010/11	994
LAJA	-71.376	-37.386							-28.274	6.392	n/a	0.282	0.252	n/a	2009/07	2010/11	311
LEMU	-72.004	-34.391							-30.844	20.310	n/a	0.304	0.236	n/a	2010/03	2011/04	343
LHCL	-65.595	-38.003	-0.288	-1.143	5.330	0.462	0.456	1.602	-3.415	1.235	0.317	0.257	0.192	0.739	2004/01	2011/02	1225
LMHS	-70.752	-37.024							-24.956	6.066	n/a	0.241	0.220	n/a	2010/04	2011/06	434
LNDS	-70.576	-32.840							-2.882	-1.256	n/a	0.173	0.170	n/a	2010/01	2011/01	221
LNQM	-71.362	-38.455	9.364	-0.987	n/a	5.093	5.076	n/a							2009/01	2010/08	488
LPGS	-57.932	-34.907	0.212	-0.202	2.767	0.908	0.901	3.432	-1.288	-0.833	-0.890	0.195	0.228	1.077	2007/01	2011/06	1597
LSCH	-71.246	-29.908	18.584	8.130	2.441	0.799	0.784	2.643							2006/11	2011/04	1483
LTUE	-71.726	-34.103							-26.098	3.096	n/a	0.146	0.179	n/a	2010/04	2011/01	123
LVIL	-71.514	-31.909	22.682	6.868	3.554	0.428	0.411	1.452							2004/01	2010/11	1772
MA01	-68.057	-38.951							-5.174	3.342	n/a	0.231	0.222	n/a	2009/08	2011/06	349

MAUL	-70.821	-35.810	17.783	6.076	-0.954	0.707	0.657	2.571	-41.355	7.953	4.820	0.417	0.265	1.127	2004/01	2011/03	1988
MGIN	-46.328	-22.319	1.045	0.386	0.656	1.146	1.146	3.786							2008/01	2011/06	1122
MGUB	-48.256	-18.919	-0.136	-0.339	-0.122	0.831	0.831	2.556							2008/01	2011/06	1216
MNMI	-69.596	-19.131	17.769	3.900	n/a	2.780	2.780	n/a							2007/04	2010/04	831
MSCG	-54.541	-20.441	0.631	-0.936	2.881	1.204	1.197	3.999							2008/01	2011/06	992
MTBA	-52.265	-15.890	-1.982	-1.964	-0.251	1.901	1.897	6.333							2008/08	2011/06	968
MZ01	-68.788	-33.135	8.356	2.140	-6.717	1.232	1.226	4.809	-3.663	-2.089	-0.017	0.213	0.227	1.206	2007/01	2010/11	1137
MZ02	-68.478	-33.092							-5.057	-3.718	n/a	0.263	0.297	n/a	2007/01	2011/03	882
MZ03	-68.796	-32.844	7.239	2.215	-0.386	1.103	1.103	3.963							2007/01	2010/04	1133
MZ04	-69.021	-32.949	8.409	2.626	0.524	1.208	1.206	4.428	-2.778	-1.662	-0.822	0.252	0.219	1.129	2007/01	2011/02	1247
MZ05	-69.169	-32.952	9.023	2.893	0.258	1.464	1.441	6.012	-2.957	-1.395	n/a	0.245	0.215	n/a	2007/03	2010/12	931
MZAC	-68.876	-32.895							-2.819	-1.167	n/a	0.184	0.180	n/a	2010/02	2011/06	459
MZAE	-68.150	-33.255	6.862	-1.009	4.241	1.375	1.374	5.547	-4.303	-1.561	-1.144	0.200	0.190	0.995	2007/05	2011/06	1329
MZAS	-68.335	-34.615	4.441	1.282	1.353	1.016	1.009	3.819	-9.007	-2.607	-1.754	0.232	0.219	1.049	2007/01	2010/10	1361
NAVI	-71.825	-33.953							-23.739	5.125	n/a	0.222	0.252	n/a	2010/03	2010/12	257
NIEB	-73.401	-39.869													2010/01	2010/12	336
NIHU	-72.397	-36.395							-27.266	0.360	n/a	0.239	0.226	n/a	2010/03	2011/06	385
OVLL	-71.204	-30.604	20.688	7.814	8.678	0.952	0.936	3.444							2004/04	2011/04	2234
PCHA	-69.432	-19.869	16.143	6.770	-0.729	1.781	1.803	5.970							2007/01	2008/12	701
PCLM	-72.004	-34.385							-25.422	16.540	n/a	0.221	0.196	n/a	2010/04	2011/06	371
PECL	-73.651	-37.687							-21.379	-6.081	n/a	0.256	0.206	n/a	2010/05	2011/06	264
PEDR	-70.689	-30.839	19.092	7.570	6.043	1.026	1.008	3.270							2007/02	2010/03	761
PELL	-72.606	-35.828							-29.293	2.293	n/a	0.429	0.176	n/a	2010/03	2011/03	328
PFRJ	PFRJ	-71.635	-30.675	22.788	8.104	7.716	0.889	2.607							2006/11	2010/11	1244
PLAJ	-72.695	-37.257							-22.165	-4.705	n/a	0.251	0.199	n/a	2010/03	2011/04	341
PMEJ	-70.448	-23.101	39.750	22.643	4.735	7.848	7.697	9.883							2007/03	2010/04	1067
PMQE	-71.630	-34.548							-26.382	6.724	n/a	0.166	0.175	n/a	2010/03	2011/01	112
POAL	-51.120	-30.074	1.050	1.268	n/a	1.572	1.572	n/a							2007/01	2011/06	1340

POLI	-46.730	-23.556	0.085	0.581	0.642	0.823	0.822	2.853							2007/04	2011/06	1439
PORT	-70.130	-32.835	18.305	5.829	8.229	0.335	0.330	1.158	-2.657	-2.186	1.547	0.344	0.204	0.882	2004/01	2011/04	2377
PPTE	-51.409	-22.120	-0.025	0.129	n/a	0.821	0.820	n/a							2007/01	2011/06	1538
PTPC	-71.997	-34.131							-30.380	5.339	n/a	0.149	0.171	n/a	2010/04	2011/01	127
PWRO	-69.211	-38.423							-7.151	4.389	n/a	0.241	0.216	n/a	2010/06	2011/06	369
QLAP	-72.126	-36.085							-26.969	0.291	n/a	0.284	0.182	n/a	2010/03	2011/04	343
RCSD	-71.613	-33.654	27.105	9.319	1.324	2.841	2.807	8.976	-18.744	3.786	-2.720	0.296	0.165	0.586	2008/10	2011/01	631
RGAO	-69.380	-34.246							-11.909	-0.807	n/a	0.233	0.210	n/a	2010/03	2011/06	448
ROBL	-71.015	-32.977	23.849	7.672	9.383	3.957	3.956	8.404	-2.978	0.451	-0.236	0.213	0.156	0.734	2008/10	2011/04	770
S031	-58.519	-34.574	-1.000	4.290	n/a	3.408	3.374	n/a							2007/01	2008/05	492
SANP	-71.481	-33.874							-19.797	2.656	n/a	0.171	0.169	n/a	2010/05	2010/12	204
SANT	-70.669	-33.150	21.172	6.279	4.817	0.335	0.329	1.098	-5.051	-0.839	1.777	0.316	0.191	0.730	2004/01	2011/04	2418
SCCH	-52.600	-27.138	1.013	2.426	4.225	1.527	1.527	5.019							2008/04	2011/06	1064
SCLA	-50.304	-27.793	0.665	1.139	3.685	1.445	1.445	5.121							2008/04	2011/06	1142
SILL	-70.739	-29.255	20.957	5.187	7.337	3.740	3.739	8.118							2008/06	2011/04	942
SJAV	-71.733	-35.595	30.481	5.951	5.619	0.679	0.655	2.370	-41.845	4.155	-0.519	0.316	0.209	0.963	2004/01	2011/01	2029
SL01	-66.314	-33.156							-2.921	-1.663	n/a	0.189	0.177	n/a			583
SLMC	-70.963	-31.777	21.825	6.269	5.642	0.415	0.410	1.494							2004/01	2011/01	1971
SMAR	-53.717	-29.719	0.939	-0.701	0.714	0.958	0.958	3.468							2007/01	2011/06	1579
SOLD	-73.138	-36.700							-25.968	1.335	n/a	0.213	0.221	n/a	2010/03	2011/06	388
SRLP	-64.280	-36.622	4.003	3.278	n/a	4.239	4.287	n/a	-2.942	-0.381	0.243	0.215	0.218	1.103	2009/01	2011/06	865
SUCE	-65.303	-19.006	7.078	4.009	3.355	1.253	1.260	4.083							2007/01	2009/11	758
SVIC	-54.488	-26.994	-0.455	-1.232	5.954	3.726	3.726	9.408							2009/01	2011/06	805
TERO	-64.257	-27.789	3.661	0.878	n/a	3.494	3.494	n/a							2009/01	2011/06	877
TMCO	-72.614	-38.765							-11.047	1.304	n/a	0.245	0.239	n/a	2010/05	2011/06	367
TOLO	-70.806	-30.170	17.930	7.626	9.302	0.868	0.856	2.766							2005/05	2011/04	1993
TRJA	-64.717	-21.549	5.828	0.550	n/a	2.293	2.279	n/a							2008/01	2009/11	375
TUCU	-65.230	-26.843	3.305	-0.738	-3.008	0.948	0.945	3.582							2007/01	2011/06	1345

UAPE	-70.141	-20.243	23.825	4.146	3.401	0.993	0.991	3.333							2007/01	2010/04	1177
UBAT	-45.119	-23.500	-3.231	0.325	n/a	1.904	1.905	n/a							2007/01	2010/11	843
UBER	-48.317	-18.890	-0.717	-0.866	1.331	0.672	0.672	2.181							2007/01	2011/06	1372
UCOR	-64.194	-31.435	5.036	2.376	n/a	3.791	3.791	n/a							2009/01	2011/06	744
UDEC	-72.345	-37.472							-31.652	-0.708	n/a	0.263	0.222	n/a	2010/01	2011/06	510
UFPR	-49.231	-25.448	0.438	0.171	-0.167	0.854	0.852	2.844							2007/09	2011/06	1349
UNRO	-60.628	-32.959	6.343	3.571	-4.912	4.613	4.613	6.106	-2.219	-0.691	1.494	0.160	0.195	0.907	2009/01	2011/06	863
UNSA	-65.408	-24.727	0.062	1.171	6.693	1.444	1.463	5.436							2007/01	2011/06	1552
UNSJ	-68.577	-31.541	13.492	2.426	n/a	3.836	3.836	n/a							2009/01	2011/06	862
UTAR	-70.297	-18.491	18.697	7.436	n/a	7.441	7.437	n/a							2007/01	2010/04	668
UYMO	-56.260	-34.888							-0.731	-0.248	n/a	0.175	0.175	n/a	2010/01	2011/06	504
UYRO	-53.555	-34.001							-0.770	-0.285	n/a	0.159	0.158	n/a	2010/01	2011/06	488
VALL	-70.764	-28.572	25.461	3.734	7.781	2.047	2.042	6.420							2008/06	2011/03	923
VALN	-71.635	-33.028	27.772	11.781	2.991	0.540	0.529	1.899	-2.714	2.353	0.687	0.319	0.188	0.833	2005/07	2011/04	1891
VALP	-71.626	-33.027							-2.758	3.249	n/a	0.193	0.215	n/a	2008/08	2011/04	87
VARG	-45.435	-21.543	-1.989	-1.114	n/a	2.314	2.315	n/a							2007/01	2009/09	924
VBCA	-62.269	-38.701	1.979	3.511	n/a	4.723	4.740	n/a	-3.132	-0.396	-1.387	0.222	0.238	1.174	2007/01	2011/06	836
VITA	-72.865	-36.424							-23.472	-0.830	n/a	0.290	0.171	n/a	2010/03	2011/04	342
VNEV	-70.249	-33.354	18.026	5.223	4.472	0.332	0.328	1.212							2004/01	2010/05	1800

*Secular rates are calculated only when the station's valid measurements (smaller or equal to the number of epochs) span through more than 1.5 years. Vz is discarded (n/a) when the values is larger than 13 mm/yr.

**Postseismic deformation values are calculated only for stations between 45°W and 75°W, 32°S and 40°S. Calculations are made only when there are more than 180 epochs between 02/27/2010 and 06/30/2011. Data values represent the deformation of the recorded time span of each station. Rz values are adopted when (1) the pre-earthquake time series is long enough to estimate the Vz and seasonal variations, or (2) the post-earthquake time series is long enough and has enough number of epochs that allow the estimates of Vz and seasonal variations, and the corrected time series has a smaller dynamic range than the pre-corrected time series. Otherwise Vrz values are discarded (shown as n/a).

Table S2: Newly augmented coseismic displacement from cGPS data as compared to Vigny et al. [2011]

Site	Position		Cosesimic (mm)			Uncertainties (mm)			Time Span			Augment. to Moreno et al. [2012]
	Lon	Lat	He	Hn	Hv	She	Shn	Shv	Start	End	# Epochs	
CMPN	-70.686	-29.028	2.0	4.0	7.4	2.4	1.2	5.4	2010/01	2011/02	338	x
CSJ1	-68.427	-31.981	-47.6	-27.4	1.0	1.2	0.6	2.6	2009/09	2011/06	579	x
CSLO	-69.302	-31.785	-37.1	-26.5	-2.6	1.3	0.6	2.7	2009/06	2011/06	673	
EBYP	-55.892	-27.369	-2.2	-4.5	-0.6	1.2	0.6	2.3	2009/01	2011/06	855	
IMBT	-48.656	-28.235	-2.9	1.2	7.9	1.2	0.6	2.5	2007/09	2011/05	1246	x
IQQE	-70.132	-20.274	-0.6	-2.0	-4.0	1.1	0.5	2.1	2008/06	2011/06	1051	
JBAL	-65.623	-27.584	-1.9	-4.0	-9.5	0.9	0.5	1.9	2009/06	2011/06	680	
MGIN	-46.328	-22.319	-2.3	-2.3	-3.1	0.6	0.3	1.1	2008/01	2011/06	1122	x
MGUB	-48.256	-18.919	-0.9	-2.0	2.3	0.4	0.2	0.8	2008/01	2011/06	1216	x
MSDO	-54.814	-22.217	-1.2	-4.9	1.5	2.2	1.1	4.3	2010/01	2011/06	319	x
NIEB	-73.401	-39.869	-2.2	-34.3	-15.4	2.9	1.4	7.5	2010/01	2010/12	336	x
OURI	-49.895	-22.949	0.9	-2.9	-3.2	1.2	0.6	2.3	2009/06	2011/05	490	x
POLI	-46.730	-23.556	-0.7	0.7	6.7	1.1	0.5	2.1	2007/04	2011/06	1439	x
PPTE	-51.409	-22.120	-3.3	-2.9	-5.2	0.7	0.4	1.4	2007/01	2011/06	1538	x
PRGU	-51.488	-25.384	-1.5	-3.6	-6.1	0.9	0.5	1.8	2009/04	2011/06	598	x
PRMA	-51.938	-23.41	-0.5	-3.5	-4.5	0.8	0.4	1.5	2009/04	2011/06	634	x
ROSA	-52.952	-22.523	-1.9	-2.1	-8.7	0.9	0.4	1.8	2009/06	2011/05	532	x
SCCH	-52.600	-27.138	-2.0	-1.3	-5.7	0.9	0.5	1.8	2008/04	2011/06	1064	x
SCLA	-50.304	-27.793	-3.0	-1.8	-3.5	0.8	0.4	1.5	2008/04	2011/06	1142	x
SJRP	-49.36	-20.786	-0.7	-3.0	-0.4	1.1	0.5	2.1	2010/01	2011/05	485	x
SMAR	-53.717	-29.719	-6.4	-1.7	5.9	0.8	0.4	1.6	2007/01	2011/06	1579	x
SVIC	-54.488	-26.994	-1.6	-2.8	-0.7	1.9	1.0	3.8	2009/01	2011/06	805	
UBER	-48.317	-18.890	0.3	-1.7	-1.3	0.7	0.4	1.3	2007/01	2011/06	1372	x
UNSA	-65.408	-24.727	-7.0	-2.5	5.2	1.5	0.8	3.0	2007/01	2011/06	1552	
UYNI	-66.826	-20.466	-0.8	-1.6	-7.1	0.9	0.4	1.6	2007/01	2011/06	724	x
UYTA	-55.938	-31.683	-8.6	-8.0	-7.9	1.3	0.7	3.0	2010/01	2011/06	438	x
VMON	-63.484	-21.259	7.1	-3.0	-8.4	4.7	2.3	9.7	2009/09	2010/09	254	x